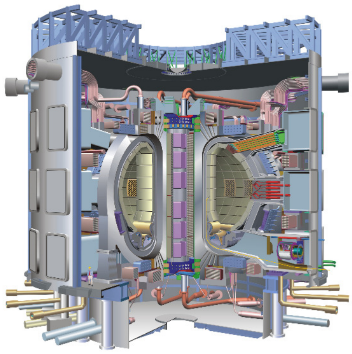

Education and Culture DG

Master of Science in Nuclear Fusion and Engineering Physics

Erasmus Mundus

Microwave heating of plasmas with the new 14 GHz system at the stellarator TJ-K

Master Thesis
presented by

Michael Løiten

Thesis Promoter
Thomas Hirth
Universität Stuttgart

Thesis Supervisor
Alf Köhn

July 7th, 2013

UNIVERSITEIT GENT

UNIVERSIDAD COMPLUTENSE MADRID

Universidad Carlos III de Madrid

Universität Stuttgart

UNIVERSITÉ DE LORRAINE

Microwave heating of plasmas with the new 14 GHz system at the stellarator TJ-K

Master Thesis
presented by

Michael Løiten

Thesis Promoter
Thomas Hirth
Universität Stuttgart

Thesis Supervisor
Alf Köhn

Erasmus Mundus Program on Nuclear Fusion Science and Engineering Physics

July 7th, 2013

Abstract

The aim of this thesis has been to investigate the plasmas generated by the newly installed 14 GHz microwave heating system at TJ-K in the equilibrium state. The new heating system has been installed in order to operate TJ-K at a wider range of controllable parameters.

Several diagnostics have been used to investigate the plasma: An interferometer was used to obtain the line averaged density. A radially movable device with three Langmuir probes was used to obtain the radial profiles of the electron density and the electron temperature. An optical diode was used to obtain the radiation mainly in the visible range, whereas a bolometer with eight channels was used in order to obtain the poloidal radiation profiles. In addition, the neutral gas pressure, the magnetic field (based on the current running through the coils), and the injected and reflected microwave power was measured.

Magnetic and pressure scans in the new regime have been performed, meaning that the scanned parameter has been varied on a shot to shot basis, whereas the other parameters have been kept constant. In addition to increase the parameter space, the magnetic field has been varied in order to vary the power deposition in the plasmas. The pressure has been varied in order to approach regimes where neoclassical effects become important. When lowering the collisionality, collisional regimes where neoclassical effects dominates can be reached.

Lower collisional regimes were found for low pressures in hydrogen. However, operation at these collisional regimes is not readily available as it was found that the plasmas become increasingly unstable when closing in on these regimes.

With this heating system one can operate at higher magnetic fields, and thus increase the confinement of the plasma. It has been found that plasmas in this regime have higher densities than the previously installed heating systems. This makes the new heating system a good candidate in studying over-dense plasmas.

Contents

Chapter 1

Introduction

Due to an increasing energy demand in the world, it is urgent to develop technologies to harvest energy from non-fossil fuel sources. As other technologies try to harvest the energy directly or indirectly from the sun, *fusion* is the only technology which tries to reproduce the processes taking place on the sun in order to produce electrical energy.

Fusion energy has major advantages compared to other technologies. Firstly, it is theoretically possible to fuel a fusion machine with the elements found in normal seawater. Also, it does not depend on weather conditions in the same way as for example solar cells or wind turbines do.

However, mimicking the processes found on the sun turns out to be a difficult task. Major theoretically and engineering challenges have hindered the way towards a break even machine (that is a machine where the harvested energy is larger than the energy input). Yet certain challenges have to be solved in order to distribute energy harvested from a fusion machine onto the electrical grid. The difficulties depend on what way one wish to harvest energy from the fuel.

The first way to harvest energy is to hit a small pellet of the fuel with powerful lasers. This is referred to as *inertial confinement*. This method will not be considered in this thesis. The second way of harvesting the energy is by heating the fuel until it reaches its plasma state. That is, the fuel consists of charged particles. By further heating, the plasma is able to release its energy through fusion. Since the fuel will be heated to temperatures higher than those found on the sun, one cannot contain the fuel in a normal container.

On the contrary, as the plasma consists of charged particles, it is influenced by magnetic fields due to the Lorentz-force. Therefore it is possible to contain the plasma with magnetic fields. This is referred to as *magnetic confinement*. Difficulties related to turbulent transport in the edge region of the plasma is one of the main hinder for fusion through magnetic confinement.

Some low temperature machines, such as TJ-K, have the possibility of scaling the dimensionless parameters to the conditions found in the edge region of these high temperature fusion machines. In order to increase the parameter space where the experiments can be performed at in TJ-K, a 14 GHz microwave heating system has been installed. This enables TJ-K to be operated at magnetic fields up to about 500 mT. With higher magnetic field, higher confinement of the plasma is possible.

The goal of this thesis has been to characterize the plasmas created by this new heating system. One of the tasks have been to find out if we reach lower collisional regimes (or to find out how close we can approach them) in order to be able to investigate neoclassical transport effects.

This thesis is organized as follows: After this brief introduction, chapter 2 is presenting the theory used. The theory of waves in cold plasmas, collisional transport and calculation of radiation losses are briefly discussed. Chapter 3 presents the experiment TJ-K together with the newly built 14 GHz heating system. A summary of the diagnostics used is given in chapter 4. The results of the plasma characterization performed in this thesis are given in 5. First the results from the magnetic field scan is presented, followed by the results obtained from the base pressure scan. A summary and outlook are finally given in chapter 6.

Where nothing else is specified, the notation used in this thesis is summarized in table 1.1.

Quantity	Symbol	Units
Temperature	T	[eV]
Elementary charge	q	[C]
Approximately equal to	$\simeq$	-
Rounded to	$\approx$	-
Orders of magnitude larger than	$\gg$	-
Orders of magnitude less than	$\ll$	-

TABLE 1.1: *The notation used in this thesis.*

Chapter 2

Theory

2.1 Waves in cold plasmas

We will in this section give the derivation of the dispersion relation with the *cold* plasma model. The derivation is based on [1], where the collisional effects have been neglected. For derivation with collisional effects, see [2].

In the cold plasma model used here, the plasma consists of ions and electrons treated like separated frictionless fluids, homogeneous in space. The fluids are taken to be neutral with zero temperature and immersed in an uniform magnetic field. The only movement by the electrons and ions is assumed to be due to the electromagnetic wave itself. The reader might observe that this is a huge oversimplification, but the results obtained from this theory is in surprisingly good agreement with what is obtained from kinetic plasma theory (using the Vlasov equation) [3].

The idea is to find an expression for the dielectric tensor, and derive the dispersion relation from this. We start by letting the unsubscripted values represent the relevant wave quantities. The relevant Maxwell's equations are

$$\nabla \times \boldsymbol{E} = -\frac{\partial \boldsymbol{B}}{\partial t} \tag{2.1}$$

$$\nabla \times \boldsymbol{B} = \mu_0 \boldsymbol{j} + \varepsilon_0 \mu_0 \frac{\partial \boldsymbol{E}}{\partial t}. \tag{2.2}$$

In this case $\frac{\partial}{\partial t}$ and $\nabla\times$ commutes, which means that the order of the operations are without importance. Therefore, we can use $\nabla\times$ on equation (2.1), $\frac{\partial}{\partial t}$ on equation (2.2), substitute the two and obtain

$$\nabla \times (\nabla \times \boldsymbol{E}) + \frac{\partial}{\partial t}\left(\mu_0 \boldsymbol{j} + \varepsilon_0 \mu_0 \frac{\partial \boldsymbol{E}}{\partial t}\right) = 0. \tag{2.3}$$

We now assume that the wave fields are small, so that the current is a linear functional of the electric field. If we also assume that the plasma is homogeneous in space and time, we can write

$$\boldsymbol{E}(\boldsymbol{x},t) = \int \boldsymbol{E}(\boldsymbol{k},\omega)\exp(i[\boldsymbol{k}\cdot\boldsymbol{x}-\omega t])\frac{\mathrm{d}^3\boldsymbol{k}}{(2\pi)^3}\frac{\mathrm{d}\omega}{2\pi}. \tag{2.4}$$

That means that each Fourier mode in equation (2.4) is a solution of (2.3). The assumption that the wave fields are small gives us

$$\boldsymbol{j}(\boldsymbol{k},\omega) = \boldsymbol{\sigma}(\boldsymbol{k},\omega)\cdot\boldsymbol{E}(\boldsymbol{k},\omega), \tag{2.5}$$

where $\boldsymbol{\sigma}$ is the conductivity tensor in the plasma. We have to use the tensor quantity since we are assuming an anisotropic plasma.

Equation (2.3) for one Fourier mode can now be written like

$$\boldsymbol{k}\times(\boldsymbol{k}\times\boldsymbol{E}) + i\omega(\mu_0\boldsymbol{\sigma}\cdot\boldsymbol{E} - \varepsilon_0\mu_0 i\omega\boldsymbol{E}) = 0. \tag{2.6}$$

Using that $\varepsilon_0\mu_0c^2 = 1$, the expression yields

$$\left(\boldsymbol{kk} - k^2\mathbf{1} + \frac{\omega^2}{c^2}\boldsymbol{\varepsilon}\right)\cdot\boldsymbol{E} = 0, \tag{2.7}$$

where and $\mathbf{1}$ is the dyadic tensor, and $\boldsymbol{\varepsilon}$ is the dielectric tensor given by

$$\boldsymbol{\varepsilon} = \left(\mathbf{1} + \frac{i}{\omega\varepsilon_0}\boldsymbol{\sigma}\right). \tag{2.8}$$

In order for $\boldsymbol{E}$ to have a nonzero solution, we require from equation (2.7) that

$$\det\left(\boldsymbol{kk} - k^2\mathbf{1} + \frac{\omega^2}{c^2}\boldsymbol{\varepsilon}\right) = 0. \tag{2.9}$$

Since the ions are so much heavier than the electrons, the ion contribution will be negligible. If we in addition neglect dissipative terms, the equation of motion yields

$$m_e\frac{\partial\boldsymbol{v}}{\partial t} = -q(\boldsymbol{E} + \boldsymbol{v}\nabla\times\boldsymbol{B}_0). \tag{2.10}$$

We now specify our coordinate system, so that the background magnetic field B_0 is aligned in the z-direction (see figure 2.1)

$$v_x = \frac{-iq}{\omega m_e}\frac{1}{1-\omega_{ce}^2/\omega^2}\left(E_x - i\frac{\omega_{ce}}{\omega}E_y\right) \tag{2.11}$$

$$v_y = \frac{-iq}{\omega m_e}\frac{1}{1-\omega_{ce}^2/\omega^2}\left(i\frac{\omega_{ce}}{\omega}E_x + E_y\right) \tag{2.12}$$

$$v_z = \frac{-iq}{\omega m_e}E_z, \tag{2.13}$$

where

$$\omega_{ce} = \frac{qB_0}{m_e}. \tag{2.14}$$

Since we are neglecting the thermal distribution of the electrons, and by that assuming that all electrons are moving in the same way, the current arising from the electric field may be written like

$$\boldsymbol{j} = -qn_e\boldsymbol{v} = \boldsymbol{\sigma} \cdot \boldsymbol{E}. \tag{2.15}$$

Equation (2.15) implies that

$$\boldsymbol{\sigma} = \frac{in_eq^2}{m_e\omega}\frac{1}{1-\omega_{ce}/\omega^2}\begin{bmatrix} 1 & -\omega_{ce}/\omega & 0 \\ \omega_{ce}/\omega & 1 & 0 \\ 0 & 0 & 1-\frac{\omega_{pe}^2}{\omega^2} \end{bmatrix}. \tag{2.16}$$

Substituting this into equation (2.8) yields

$$\boldsymbol{\varepsilon} = \begin{bmatrix} 1-\frac{\omega_{pe}^2}{\omega^2-\omega_{ce}^2} & \frac{i\omega_{pe}^2\omega_{ce}}{\omega(\omega^2-\omega_{ce}^2)} & 0 \\ \frac{-i\omega_{pe}^2\omega_{ce}}{\omega(\omega^2-\omega_{ce}^2)} & 1-\frac{\omega_{pe}^2}{\omega^2-\omega_{ce}^2} & 0 \\ 0 & 0 & 1-\frac{\omega_{pe}^2}{\omega^2} \end{bmatrix}, \tag{2.17}$$

where

$$\omega_{pe} = \sqrt{\frac{n_eq^2}{\varepsilon_0 m_e}} \tag{2.18}$$

is the electron plasma frequency.

Let us now use

$$X = \omega_{pe}^2/\omega^2 \qquad Y = \omega_{ce}/\omega \qquad N = kc/\omega, \tag{2.19}$$

together with the geometry depicted in figure 2.1. By writing out equation (2.9) and using equation (2.17), we get

$$\begin{vmatrix} -N^2+1-\frac{X}{1-Y^2} & \frac{iXY}{1-Y^2} & 0 \\ -\frac{iXY}{1-Y^2} & -N^2\cos^2\theta+1-\frac{X}{1-Y^2} & N^2\cos\theta\sin\theta \\ 0 & N^2\cos\theta\sin\theta & -N^2\sin^2\theta+1-X \end{vmatrix} = 0. \tag{2.20}$$

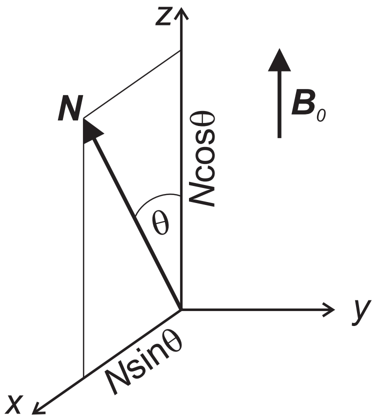

FIGURE 2.1: *Cartesian coordinate system specifying the propagating wave in the magnetized plasma. From [4].*

By solving for N^2, we end up with the so called Appleton-Hartree equation

$$N^2 = 1 - \frac{X(1-X)}{1 - X - \frac{1}{2}Y^2\sin^2\theta \pm \left[\left(\frac{1}{2}Y^2\sin^2\theta\right)^2 + (1-X)^2Y^2\cos^2\theta\right]^{1/2}}. \tag{2.21}$$

The ± sign in equation (2.21) tells us about the properties of the wave. The plus sign refers to a *ordinary mode* (O-mode) if $\boldsymbol{k} \perp \boldsymbol{B}_0$, and to a left-hand circularly polarized mode if $\boldsymbol{k} \parallel \boldsymbol{B}_0$. The minus sign refers to a *extraordinary mode* (X-mode) if $\boldsymbol{k} \perp \boldsymbol{B}_0$, and to a right-hand circularly polarized mode if $\boldsymbol{k} \parallel \boldsymbol{B}_0$.

2.1.1 Limitations in the cold wave dispersion relation

We have arrived to equation (2.21) by using the assumptions that the wave is propagating through a homogeneous[1] , isotropic[2] medium, with low enough intensities[3].In the derivation we assumed that $v_{th,e} \ll c$, so that the particles could be taken as stationary only perturbed by the propagating wave. The motion of ions was neglected since $m_e \ll m_i$.

Strictly speaking equation (2.21) is only valid for a *homogeneous* and *isotropic* medium, which we know that our plasma is certainly not. However we can use the Wentzel, Kramers, Brillouin (WKB) approximation. In this approximation, one talks about a *locally* homogeneous medium, where N can be well defined. This is a good approximation as long as the variation in one wavelength is small, that is if $|\nabla k/k^2| \ll 1$.

---

[1] So that the Fourier components individual satisfies Maxwell's equations, which allows us to write $\mathbf{j}(\mathbf{k},\omega) = \sigma(\mathbf{k},\omega)\mathbf{E}(\mathbf{k},\omega)$ due to the linearity of each Fourier mode.

[2] So that $\mathbf{D} = \boldsymbol{\varepsilon} \cdot \mathbf{E}$.

[3] So that the current depends linearly on the fields.

In contrast to a homogeneous media, only the *sum* of the Fourier components is a solution to Maxwell's equations in an inhomogeneous medium. In the WKB approximation, the electrical field and magnetic field $\simeq \exp i(\int \boldsymbol{k} \cdot \mathrm{d}\boldsymbol{l} - \omega t)$, where $\mathbf{k} \overset{def}{=} 2\pi/\lambda = \omega/v_{\text{phase}} = N\omega/c$. If this condition is not meet, one needs to use a full wave treatment of plasma, where the geometrical boundary conditions have been specified.

2.1.2 Cut-off and resonances

If $k \to 0$ in (2.21), that is if $N \to 0$, we will have a cutoff. The wave will generally be reflected. On the other hand, if $k \to \infty$ (or equally $N \to \infty$), we will have a resonance, and an absorption of the wave in the plasma. With this information, we get the following cut-offs

$$\omega_{pe} = \sqrt{\frac{n_e q^2}{m_e \varepsilon_0}} \tag{2.22}$$

$$\omega_R = \frac{1}{2}\left(\omega_{ce} + \sqrt{\omega_{ce}^2 + 4\omega_{pe}^2}\right) \tag{2.23}$$

$$\omega_L = \frac{1}{2}\left(-\omega_{ce} + \sqrt{\omega_{ce}^2 + 4\omega_{pe}^2}\right), \tag{2.24}$$

and the following resonances for perpendicular propagation

$$\omega_{ce} = \frac{qB}{m_e} \tag{2.25}$$

$$\omega_{UHR} = (\omega_{ce}^2 + \omega_{pe}^2)^{1/2}. \tag{2.26}$$

2.2 Collisional transport

It is important to know what kind of collisional processes which are taking place in the plasma as it will effect the transport. First one need to know the collision frequency, or equally the collision time. For charged particles *Coulomb collisions* have to be considered. One collision is then defined as a 90° change in a the trajectory of a particle from a certain reference.

Once the collision time is known, one can say something about what *collisional regime* the plasma is in (see section 2.2.1). A good derivation of how to calculate the collisional frequency can be found in [5], with the following result

$$\nu_{ei} \approx \frac{q^4 n_e \ln(\Lambda)}{4\pi\varepsilon_0^2 m_e^{1/2} (3T_e)^{3/2}}, \tag{2.27}$$

where

$$\Lambda = \frac{12\pi\varepsilon_0^{1.5}T_e^{3/2}}{n_e^{1/2}q^3}, \tag{2.28}$$

and ε_0 is the vacuum permittivity, q is the elementary charge, m_e is the electron mass, n_e is the electron density and T_e is the electron temperature. An equal expression is also found in [6], although the equation has another form. In the end we observe that

$$\nu_{ei} \propto \ln\left(\frac{T_e^{3/2}}{n_e^{1/2}}\right)\frac{n_e}{T_e^{3/2}} \overset{\propto}{\sim} \frac{n_e}{T_e^{3/2}}. \tag{2.29}$$

The following assumptions have been made to obtain equation (2.27):

- The contribution from the ion velocity is neglected since one assumes $v_e \gg v_{T_i}$. This is usually what is observed, except in extreme cases.
- The reduced mass $m_r \simeq m_e$ since $m_e \ll m_i$
- Quasi neutrality is assumed so that $n_i \simeq n_e$
- The thermal velocity of the ions are set to the most probable velocity, so that $v_{T_i} = \sqrt{2T_i/m_i}$

The following assumptions have been made to obtain equation (2.28):

- The coulomb logarithm is found when integrating the impact parameter[4]b over all possibilities. To avoid the use of heavy mathematics, the upper limit in the integral has been set to λ_D instead of infinity. This is a good approximation since the contribution outside the Debye-sphere is negligible.
- The typical thermal velocity has been set to the root mean square of total velocity (in three dimensions) in a Maxwellian distribution. That is $\frac{1}{2}m_r v^2 \simeq \frac{3}{2}T_e$.

Collisions with other species can be deduced in the same way as (2.27). One only has to take care that the appropriate species subscripts and the correct limit for the reduced mass is taken. Making the same assumptions as over and by assuming that the particles are moving with the thermal velocity, we get

$$\nu_{ee} \approx \frac{q^4 n_e \log(\Lambda)}{2\pi\varepsilon_0^2 m_e^{1/2} 2.3(3T_e)^{3/2}} \tag{2.30}$$

$$\nu_{ii} \approx \frac{q^4 n_e \log(\Lambda)}{2\pi\varepsilon_0^2 m_i^{1/2} 2.3(3T_i)^{3/2}} \tag{2.31}$$

$$\nu_{ie} \approx \frac{q^4 n_e \log(\Lambda) m_e^{1/2}}{4\pi\varepsilon_0^2 m_i 1.3(3T_e)^{3/2}}. \tag{2.32}$$

---

[4] The impact parameter b is defined as the perpendicular distance between the path of a projectile (for example an electron) and the center of the field (in this case the electrical field) created by an object (for example an ion) that the projectile is approaching.

In addition, the electron collisions with the neutral gas is given in as

$$\nu_{e0} = \sqrt{\frac{2T_e}{m_e}} n_0 \sigma_{e0}, \tag{2.33}$$

where n_0 is the neutral density, and σ_{e0} is the collisional cross section between electrons and neutral particles.

2.2.1 The diffusion coefficient

Apart from turbulent transport causing *anomalous transport*, which will not be considered here, the *radial* transport in a fusion machine is mainly due to collisional effects. As the fusion device is built in such a way so that there should be no advection of the plasma core towards the vessel, diffusion will be the major contributor to the radial transport[5].

The diffusion coefficient can be deduced from random walk principles. Friedberg gives in [5] a very detailed introduction in how to derive the diffusion coefficient. Nevertheless [6] is more precise as it is taking into account the velocity distribution. In the reference, it is also shown that the same result can be derived from the transport equations themselves.

Although it should be stressed that sophisticated kinetic theory is required to accurately calculate the numerical multipliers for the transport coefficient, the results from [6] is adequate for the purposes in this thesis. The diffusion coefficient D can be written like

$$D = \frac{\delta^2}{2\tau_c}, \tag{2.34}$$

where δ^2 is the *magnitude of the average step size* between collisions (from here on just referred to as the *step size*) and τ_c is the average time between collisions. The challenge of equation (2.34) is to determine the correct step size and the correct time step.

Generally, the step size is found by determining the *time averaged change in the center of mass*, and then to integrate over all collisions and all scattering angles. One assumes equal probabilities of scattering for all angles[6]. In order to determine the time averaged change in the center of mass, one has to take into account how the particle is moving in the magnetized plasma. If one neglects all magnetic topology, the classical collisionality is obtained. When magnetic fields and the geometry of the vessel is taken into account, one finds indeed that the drifts $v_D^{\nabla B + R_C}$ are playing a major role in determining the step size[7].

---

[5] Again, we are neglecting turbulence here. However, it is possible to define a diffusion coefficient for the transport caused by the turbulence [6]

[6] The *heat conduction* coefficient can be found in the same way as the diffusion coefficient, but requires calculations of the time averaged change in the center of *energy* instead. The results are given in [5].

[7] We are here considering the single particle picture. The same results are obtained if one uses the fluid picture.

Let us start our discussion with high collisions, and then gradually work our way towards non-collisionality. The different regimes are summed up in table 2.1.

If the collisions are high enough, one only has to take into account the drifts as a consequence of the geometry and magnetic fields. This regime is referred to as *high collisional Pfirsch-Schlüter* regime. When the collision frequency is lowered, one finds that the step size is related to how the guiding center is changing after the particle has completed one poloidal revolution following[8]a field line (and by that defining a drift orbit due to the drifts). We are then speaking about the *low collisional Pfirsch-Schlüter* regime.

The time takenfor a particle with a pitch angle[9]of zero degrees to complete a poloidal revolution, τ_{tr}, is given in [6], and reads

$$\tau_{tr} = \frac{2\pi R_0}{\iota v_{\|}}, \tag{2.35}$$

where ι is the rotational transform, and $v_{\|}$ is approximated to be the thermal velocity, as this is common practice in the literature.

If the poloidal transit time is larger than the collision time τ_{ei}, the particle statistically has time to complete a poloidal turn before a collision occurs. If on the contrary, the pitch angle (the angle between the trajectory and the magnetic field at one instant), is high, the particle can be reflected by the magnetic mirror When this happens, *banana* particles trapped in the toroidal ripple become apparent.

The width of the banana particle trajectories increases for lower collisionalities, whereas the frequency decreases. As a result, the diffusion coefficient is constant in this regime, and hence the regime is called the *plateau regime*. In this regime the effective collision time (the average time it takes to make a collision so that it can be de-trapped) is approximately equal to the bounce time (the time it takes to complete a banana orbit).

Further reduction of the collision frequency leads to the case where the effective collision time is less than the bounce time. In the tokamak this leads to the *banana regime*, where the effective collision, and hence the step time decreases with the collisionality. On the contrary, in a stellarator case, particles can be *helically* trapped. Since a helically trapped particle will spend most of its time in one poloidal position (as the mirroring process takes time), the particles are lost due to the $v_D^{\nabla B+R_C}$ drift[10]. The more particles trapped in the helical ripple, the more particles will be lost in this regime. As collisions in this regime will help to de-trap particles, higher collisions will reduce the diffusion of the particles. Hence, this regime is called the *1/ν regime*.

Further reduction of the collisionality leads to a build up of a radial E field as electrons are lost more rapidly. This leads to a $v_D^{E_r\times B}$ drift, which contributes to change the poloidal position of the particles, and hence reduces the losses due to $v_D^{\nabla B+R_C}$.

---

[8] This is not to be confused with the gyration of the particle *around* the field line.

[9] The angle between the velocity vector and the magnetic field vector.

[10] When the particle is not helically trapped, the rotational transform is averaging out the $v_D^{\nabla B+R_C}$ drift.

In the end it should be stressed that ions and electrons might be located at different regimes at the same time. This has indeed been found in [7].

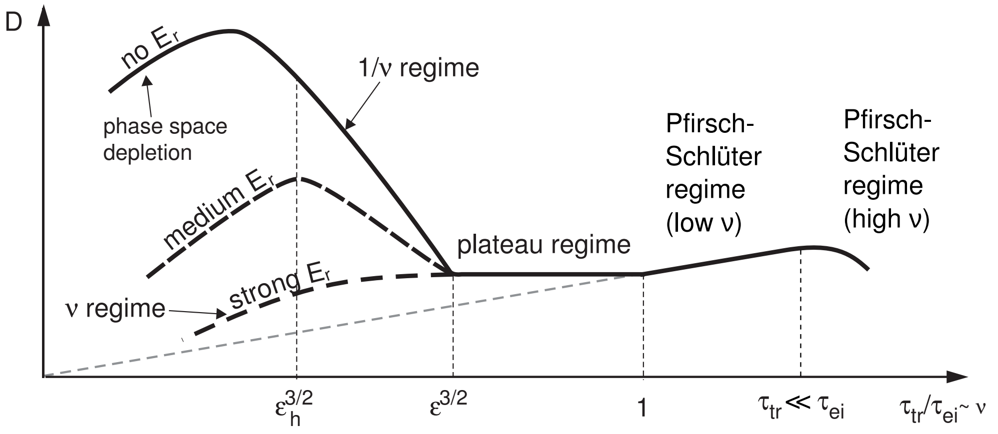

FIGURE 2.2: *The different collisional regimes found in a stellarator [8].*

2.2.2 Alternative estimation of the diffusion coefficient

Another way to estimate the diffusion coefficient is to measure the particle confinement time, and calculate the diffusion coefficient from that. The particle confinement time τ_N can be measured by the interferometer. As shown in figure 2.3, the idea is to measure when the density has dropped to $1/e$ of its original value.

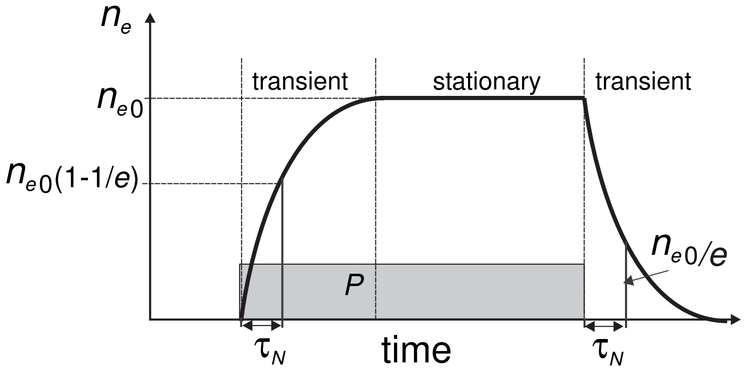

FIGURE 2.3: *Qualitative evolution of the plasma particle content when a heating pulse is applied [6].*

From a theoretical point of view, the particle confinement time can be defined as

$$\tau_N = \frac{N}{S_n}, \tag{2.36}$$

where N is the total number of particles, and S_n is the source term for particles. In a steady state, the sum of the source and the sink will be equal to zero. The sink will then be the the transport of particles to the outside the separatrix[11]. The transport is given by Fick's law[12], which reads

$$\Gamma = -D\nabla n. \tag{2.37}$$

Calling the area of the separatrix A_s, we got

$$A_s\Gamma = S_n = -D\nabla n\big|_a \simeq A_s D\frac{\overline{n}}{a} = 2\frac{DN}{a^2}, \tag{2.38}$$

where we have used that in a toroidal geometry $V/A_s = a/2$ together with $V\overline{n} = N$. By substituting equation (2.38) into the left hand side of equation (2.37) and rearranging, we obtain

$$D \simeq \frac{a^2}{2\tau_N}. \tag{2.39}$$

Similarly, we can estimate χ by measuring τ_E. It should be noted though, that the result is expected to be less accurate. The reason for this is that only one of the two source terms in the heat transport equation is taken into account in Fick's law for temperature transport.

2.3 Calculating the total radiated power

The plasma radiation is important to take into account when finding the energy balance of the plasma. It can be estimated by using the power radiated onto the bolometers. We want to find a multiplying factor which can relate the radiation measured by the bolometers , $P_{\text{chnl sum}}$, to the total radiated power from the plasma P_{total}.

As it will be shown in section 4.3.1, the bolometers have a certain line of sight. The radiation from the plasma within the line of sight is radiating in all directions, and only a small part, $A_{\text{cylinder}}/A_{\text{bolo}}$ will hit the bolometers. We are assuming that the bolometers can resolve the whole poloidal cross section, and that the channels are not overlapping. As apparent from figure 4.6b, the channels are overlapping, but this can be considered as negligible.

If we assume that the radiation hitting the bolometers in front of the central axis of the plasma is the same as the radiation hitting the bolometers from behind the central axis, and if we also neglect the curving of the plasma, we can then approximate the cone of the line of sight in toroidal direction with a outer cylinder. This is shown in figure 2.4. By using simple trigonometry, we can then calculate the toroidal length L of this outer

---

[11] In this sense the separatrix is the region where the last closed magnetic flux surface form, separating the toroidally confined region from the region where field lines connect to material surfaces.

[12] This law can be derived rigorously from the transport equation for motion itself, assuming that only a density gradient is present.

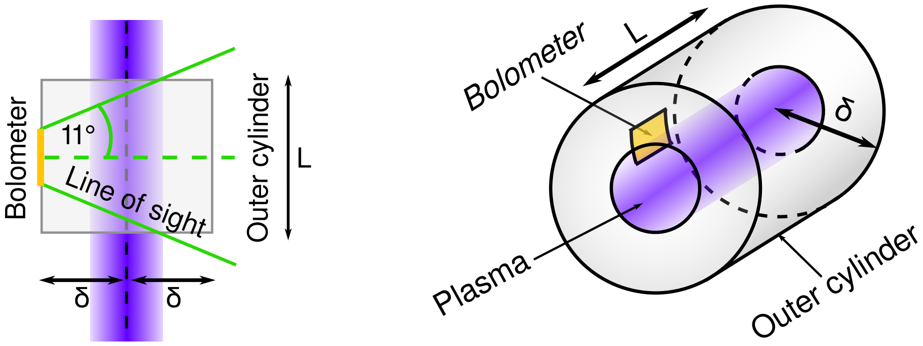

(a) Line of sight for the bolometers seen from above.

(b) The outer cylinder surrounding the bolometer.

FIGURE 2.4: *The geometry of the bolometer and plasma (not drawn to scale).*

cylinder. When L is known, we can calculate the area by $A_{\text{cylinder}} = 2\pi a L$.

This area must be related to the area of the surface of the plasma cylinder due to how the radiation depends on the distance from the source. Let us assume that the radiation is being radiated from the plasma surface $A_{\text{plasma}} = 2\pi\delta L$. The radiation from the plasma surface is then $A_{\text{cylinder}}/A_{\text{plasma}}$ times the radiation found on the outer cylinder.

To find the total radiated power, we need to relate how much the radiation found on the plasma surface is compared to the total radiation. If we assume that the radiation is equally distributed in our torus, we only need to find how long the plasma segment is compared to the total toroidal length $L_{\text{torus}} = 2\pi R_0$. In the end, we have

$$P_{\text{total}} = P_{\text{chnl sum}} \frac{A_{\text{cylinder}}}{A_{\text{bolo}}} \frac{A_{\text{cylinder}}}{A_{\text{plasma}}} \frac{L_{\text{torus}}}{L}. \tag{2.40}$$

Regime	Particle fraction	δ	τ	Condition	Comment
Classical	All	$2v_{th}/\omega_{ce}$	τ_{ei}	-	Neglecting magnetic field effects.
High ν Pfirsch-Schlüter	All	$v_D^{\nabla B+R_C}\tau_{ei}$	τ_{tr}	$\tau_{tr} \ll \tau_{ei}$	Collisions too high for poloidal transits.
Low ν Pfirsch-Schlüter	All	δ_P	τ_{tr}	$\tau_{tr} < \tau_{ei}$	Some particles complete poloidal transits.
Plateau	$\epsilon^{1/2}$	δ_{Ba}	τ_{Ba}	$\tau_{tr} > \tau_{ei}$	As trapped particles can complete more of their banana orbits for lower collisionalities, the step size increases.
Banana (tokamak)	$\epsilon^{1/2}$	δ_{Ba}	$\tau_{\text{eff}} \simeq \epsilon\tau_{ei}$	$\tau_{\text{eff}} > \tau_{Ba}$	Collisions under 90° can de-trap banana trapped particles.
$1/\nu$ (stellarator)	$\epsilon_h^{1/2}$	$v_D^{\nabla B+R_C}\tau_{\text{eff}}$	$\tau_{\text{eff, h}} \simeq \epsilon_h\tau_{ei}$	$\tau_{\text{eff}} > \tau_{Ba}$	Helically trapped particles stays longer at poloidal positions, and are lost due to $v_D^{\nabla B+R_C}$.
ν (stellarator)	$\epsilon_h^{1/2}$	$v_D^{\nabla B+R_C}/2\omega_{E\times B}$	τ_{ei}	$\tau_{\text{eff, h}} > \tau_{Ba}$	High losses builds up an E_r field. Particles are helically detrapped by $v_D^{E\times B}$. Diffusion is again due to collisions.

TABLE 2.1: *Collisional regimes.*

Chapter 3

Experimental setup

TJ-K (abbreviated from "Torsatron de la Junta de Energía Nuclear - Kiel"[1]) is a torsatron typed stellarator, and depicted on figure 3.1. It was built in Spain, and taken into operation at Spain's National Fusion Laboratory[2] in 1994. In 1999 it was moved to Christian-Albrechts-Universität in Kiel and given the current name TJ-K. In 2006 it was again moved, this time to "IGVP - Institut für Grenzflächenverfahrenstechnik und Plasmatechnologie"[3]at Universität Stuttgart.

Whereas it was previously a short pulsed machine capable of producing plasmas with T_e up to $\simeq 100\,\mathrm{eV}$, it is now a long pulsed machine capable of producing energies up to $\simeq 25\,\mathrm{eV}$. Because of the low temperatures it makes it an excellent machine for probe measurements, which is useful in investigation of turbulence.

With its major radius $R_0 = 0.6\,\mathrm{m}$ and its averaged minor radius $\langle a \rangle = 0.1\,\mathrm{m}$ it is a relatively compact stellarator, and cheap to operate compared to other machines. This makes it a good candidate for testing out new diagnostics. It has one passively cooled helical coil ($l = 1$) winded symmetrically six times ($m = 6$) around the toroidal vessel. The heat in this coil is the limit for the operational time. For lower magnetic fields, shot times up to about 60 minutes are possible, whereas for high magnetic fields (B_0 up to $\simeq 0.5\,\mathrm{T}$) the shot time can last for around 30 seconds. Two vertical field coils are placed slightly above and below the vacuum vessel. This enables shaping of the plasma by setting the current ratio between the vertical and helical field coils R_{vh}.

Three heating systems have been operational in this thesis, namely the 2.45 GHz system, the 8 GHz system and 14 GHz system. Only the plasmas generated by the 14 GHz system have been investigated in this thesis.

TJ-K is a fusion relevant experiment due to the possibility of scaling the dimensionless parameters to the conditions at the edge of high-temperature fusion plasmas [9, 10, 11].

---

[1] Originally "TJ-I U" or "Tokamak de la Junta de Energía Nuclear - I Upgrade".

[2] At that time "JEN - Junta de Energía Nuclear", now "CIEMAT - Centro para Investigaciones Energéticas, Medioambientales y Tecnológicas".

[3] At that time "IPF - Institut für Plasmaforschung".

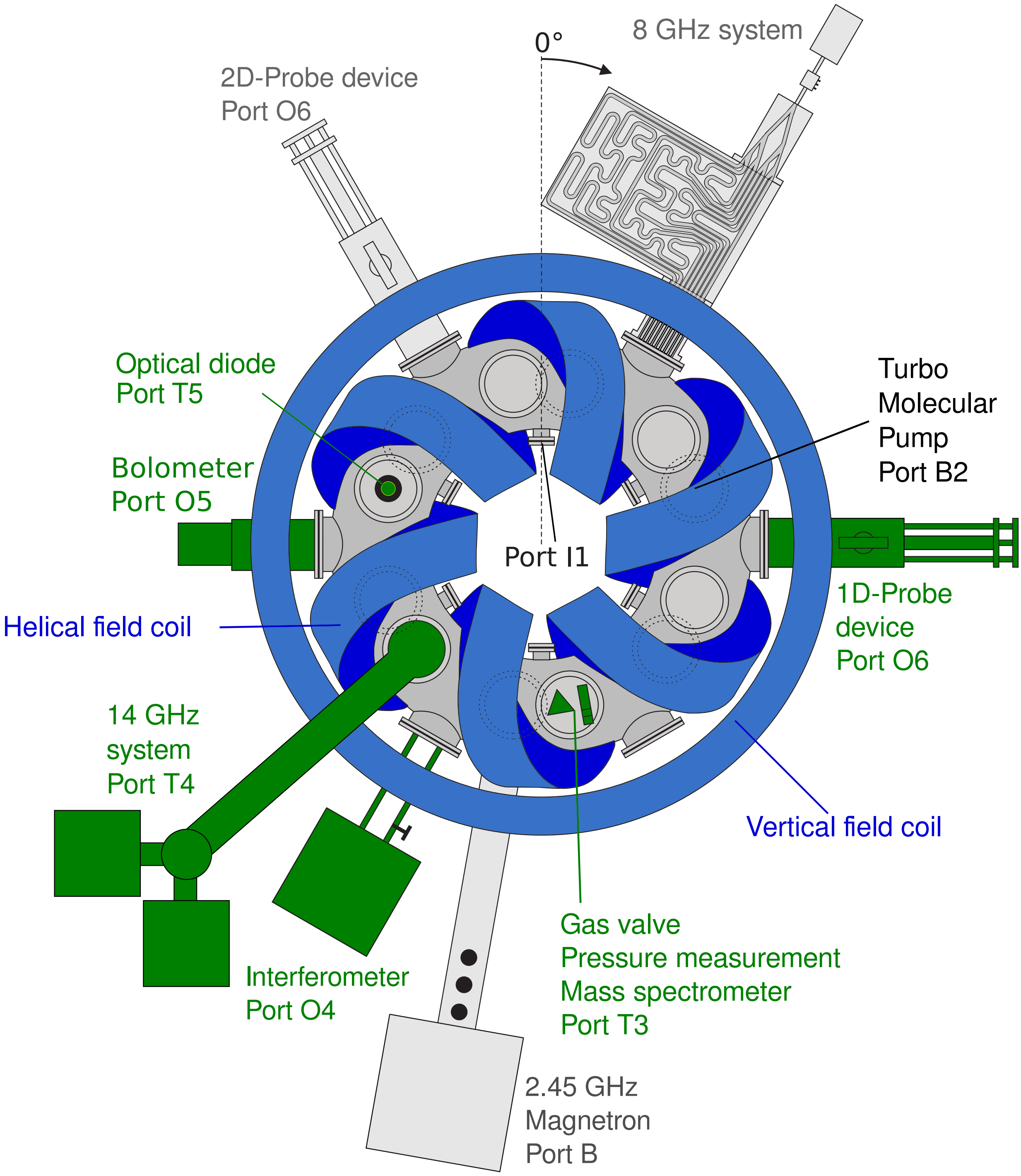

FIGURE 3.1: *The experiment TJ-K.*

3.1 The 14 GHz system

The 14 GHz system is depicted in figure 3.2. Whereas previously works mainly have focused on building and setting up the system as in [12, 13], the aim of this thesis has been to characterize the plasmas made with this system. As for this thesis, the 14 GHz system consist of two klystrons, whereas a third klystron is planned to be installed.

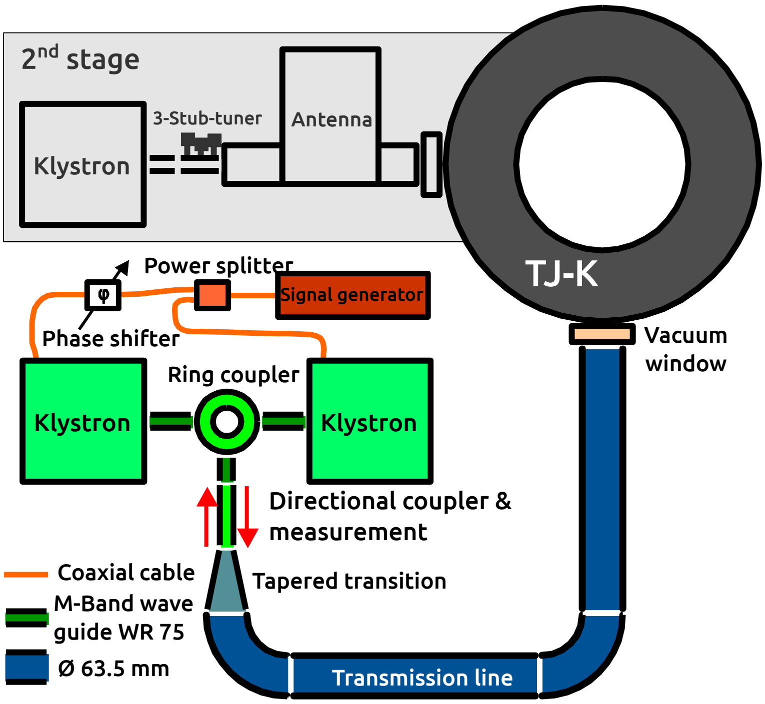

FIGURE 3.2: *The 14 GHz system. The grayed out part is planned to be installed as a second stage. From [12].*

Since the klystrons are only useful for amplifying signals, a signal generator has to be used. The signal generator in this thesis was set to produce sinusoidal signals with a frequency of 13.75 GHz. For simplicity this number is rounded to 14 GHz. The klystrons are amplifying this signal to 1.5 kW each, yielding a total of 3 kW output power. A phase shifter had been installed to ensure that the two klystrons are sending out the power in the same phase. This is a necessity for combining the power of the two klystrons using the rat-race coupler (also known as a ring coupler).

The ring coupler is shown in figure 3.3a. The input from the klystrons is connected to the ports 1 and 3. Port 2 leads to TJ-K. All out-of-phase signals will be reflected and absorbed by the dummy load after port 4. This is shown on figure 3.3b. The injected and reflected power are measured in the directional coupler.

The wave guides so far have been relatively short had a rectangular shape. This ensures propagation of the TE_{11}-mode (see [13] for more details). As the transmission line from the klystrons to the vacuum vessel is several meters long, it is important that

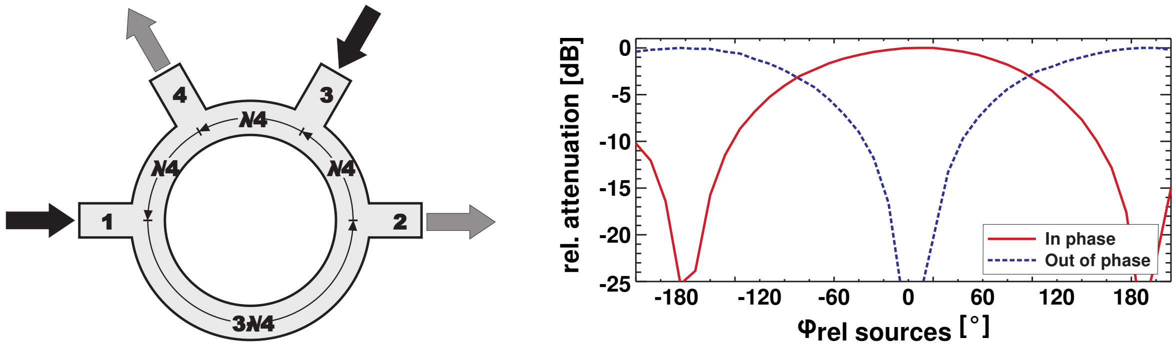

(a) The rat-race coupler (b) The signal from the coupler

FIGURE 3.3: *The rat race coupler is installed to combine the power [12].*

the loss in the waveguides are minimized. Over-sized circular waveguides have been found adequate for these purposed as shown in figure 3.4.

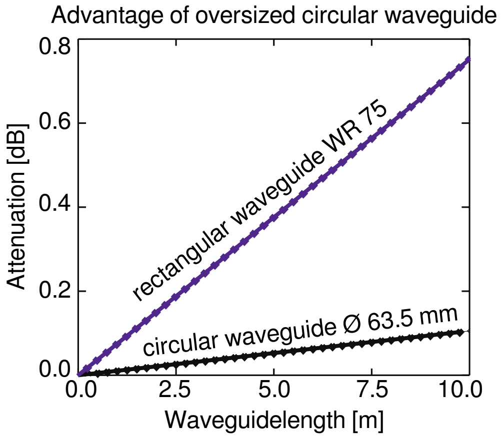

FIGURE 3.4: *Reference [13] compares the over-sized with rectangular waveguides.*

The transition from the rectangular to the circular wave guides is realized with a numerically optimized taper. It is optimized so that higher order modes will be excited as little as possible. If the propagating wave is without higher order modes, it will propagate without too much backscattering, and the power will be deposited in a narrow region in the plasma.

Two bends are included in the transmission line. Also these have been numerically optimized to prevent excitation of higher order modes. The final wave is injected as an O-mode into the vessel through port T4.

Chapter 4

Diagnostics

4.1 Microwave interferometry

The interferometer is a non-invasive diagnostic used to measure the phase shift between superimposed electromagnetic waves. In plasma diagnostics, it is a common diagnostic used to measure the *line-averaged* electron density (or simply the line-averaged density) $\overline{n}_e$. It exploits the principle that a electromagnetic wave experiences a phase shift when propagating to a plasma. The phase shift is dependent on the density of the plasma. For technical details about the interferometer used in TJ-K, see [14].

4.1.1 The basic idea

The basic idea behind an interferometer is to compare the phase of a wave sent into the plasma with a wave sent to a reference arm. This is depicted in figure 4.1. This can be done in several different ways. In TJ-K however, a *heterodyne Mach-Zehnder* interferometer is used. Since the method is non-invasive[1], the perturbation of the plasma is kept to a minimum.

Derivation of the line averaged density

A relation between the line-averaged density and phase shift can be obtained from the refractive index $N \overset{def}{=} \frac{c}{v_{\text{phase}}} = \frac{\lambda_0}{\lambda}$, where λ_0 is the wavelength in vacuum and λ is the wavelength in the medium of propagation (in this case the plasma). Details of the derivation is given in section 2.1.

However, it is not trivial that the plasma can be described with a refractive index, since the refractive index is only well defined for a homogeneous medium. Several assumptions have to be made to find $\phi(N)$, and from there to arrive at $\overline{n}_e(\phi)$. The assumptions are given in section 2.1.1. If $Y \to 0$[2], in 2.21 as it does in our case, we end

---

[1] In other words, no components are introduced in the vessel.

[2] Even when $Y \neq 0$, there exists an O-wave polarization with the same refractive index.

up with

$$N^2 = 1 - X = 1 - \left(\frac{\omega_{pe}}{\omega}\right)^2 = 1 - \frac{n_e}{n_c}, \tag{4.1}$$

where $n_c \overset{def}{=} \omega^2 m_e \varepsilon_0 / e^2$ is the cutoff density[3].

Assume now that we are injecting an electromagnetic wave into the plasma, and that we have reached a steady state. We make a reference point at the tip of the antenna. For simplicity we assume that the electric field of the wave has a maximum there (but in general, it can be any reference point on the wave). A length L from the tip of antenna, the wave is ϕ radians away from the next maximum (or the arbitrary reference point we chosen on wave). We have

$$\phi = \int_{\mathcal{L}} \boldsymbol{k} \cdot \mathrm{d}\boldsymbol{l} = \int_0^L \frac{\omega}{c} N \,\mathrm{d}l, \tag{4.2}$$

where we have used that the direction **k** and **l** coincide in an isotropic medium.

We would like to compare the phase in 4.2 with the phase of a wave that is not propagating through the plasma, acting as a reference. This is found by taking

$$\begin{aligned}\Delta\phi &= \int_{\mathcal{L}} \boldsymbol{k}_{\text{plasma}} - \boldsymbol{k}_{\text{ref}} \cdot \mathrm{d}\boldsymbol{l} = \int_0^L \frac{\omega}{c}(N_{\text{plasma}} - N_{\text{ref}})\,\mathrm{d}l = \frac{\omega}{c}\int_0^L (N_{\text{plasma}} - 1)\,\mathrm{d}l \\ &= \frac{\omega}{c}\int_0^L \left(\sqrt{1 - \frac{n_e}{n_c}} - 1\right)\mathrm{d}l \overset{n_e \ll n_c}{\simeq} \frac{\omega}{c}\int_0^L \left(1 - \frac{1}{2}\frac{n_e}{n_c} - 1\right)\mathrm{d}l = \frac{-\omega}{2cn_c}\int_0^L n_e\,\mathrm{d}l \\ &= \frac{-\omega}{2cn_c}\overline{n}_e L. \end{aligned} \tag{4.3}$$

In TJ-K the emitting and receiving antenna is located on the low-field side. The injected wave is reflected by a mirror inside the vacuum vessel. This yields $L = 2 \cdot 17\,\text{cm}$.

4.1.2 Measuring the line-averaged density

At TJ-K $|\Delta\phi| \equiv \varphi$ is measured, and from this quantity we can calculate $\overline{n}_e$. Note that the observable φ between two sinusoidal signals can be maximally 180° if nothing is done with the circuitry treating the imposed signal.

The interferometer circuitry at TJ-K was modified in the summer 2009, so that phase-shifts up to multiples of 2π can be detected. Therefore, if the phase shift is over 2π, a *fringe-jump* will occur. Since the interferometer is turned on before the plasma is started, the actual density can then be found by counting fringe-jumps in the time trace. With the circuitry currently installed, the line-averaged density from equation (4.3) is given by

$$\overline{n}_e \approx 3.9 \cdot 10^{17}\,\text{m}^{-3}\left(n_F + \frac{\Delta U}{V}\right), \tag{4.4}$$

---

[3] If $n_e = n_c \;\Rightarrow\; \omega_{pe} = \omega$. Since the dispersion relation for the injected O-wave is $\omega^2 = \omega_{pe}^2 + k^2c^2 \;\Rightarrow\; k = 0$, and there is a cutoff.

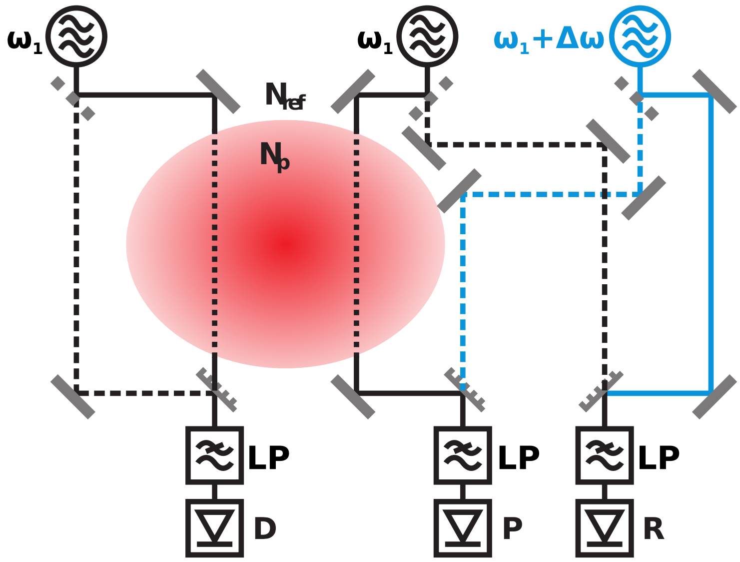

FIGURE 4.1: *Sketch of two types of Mach-Zehnder interferometers with low pass filters (LP) and detectors (D, P, R). The homodyne type is shown to the left, and the heterodyne is shown to the right [12].*

where ΔU is the measured output voltage, and n_F is number of fringe jumps.

The homodyne Mach-Zehnder interferometer

To explain how it is possible to measure φ, we start by explaining how the *homodyne* Mach-Zehnder interferometer works. The principle is depicted to the left in figure 4.1.

A wave is launched into the plasma with a frequency ω_1. In this example, we will use $\omega_1/2\pi \approx 64\,\mathrm{GHz}$, as is the case in TJ-K.[4]This gives $n_c \approx 5.1 \cdot 10^{19}\,\mathrm{m}^{-3}$, so for the measurements done at TJ-K $n_c \gg n_e$, and we can be sure that the launched wave will propagate.

Since ω_1 is so high, a direct comparison of φ between the plasma arm and the reference arm would be impossible as data acquisition at these speeds are not available to this day. Therefore, the waves must be modulated in order to obtain the phase shift. This can be done by letting the signal from the superimposed wave (consisting of the wave from the plasma arm and the wave from the reference arm) pass through a low pass filter.

In the homodyne Mach-Zehnder interferometer, the detector D is detecting the intensity I of signal from the superimposed wave. Calling the detected signal s, we

---

[4] However, be aware that TJ-K is *not* utilizing a homodyne interferometer.

then have that[5]

$$\begin{aligned} I_D &\propto (s_\mathrm{p} + s_\mathrm{ref})^2 = (s_{\mathrm{p},0}\cos\{\omega_1 t + \varphi\} + s_{\mathrm{ref},0}\cos\{\omega_1 t\})^2 \\ &\propto \frac{s_{\mathrm{p},0}^2}{2}(1+\cos\{2[\omega_1 t + \varphi]\}) + \frac{s_{\mathrm{ref},0}^2}{2}(1+\cos\{2[\omega_1 t]\}) + s_{\mathrm{p},0}s_{\mathrm{ref},0}(\cos\{\varphi\} + \cos\{2\omega_1 t + \varphi\}). \end{aligned} \tag{4.5}$$

The low pass filter will filter out the high frequencies, so we are left with

$$I_D \propto \frac{s_{\mathrm{p},0}^2}{2} + \frac{s_{\mathrm{ref},0}^2}{2} + s_{\mathrm{p},0}s_{\mathrm{ref},0}\cos(\varphi). \tag{4.6}$$

The heterodyne Mach-Zehnder interferometer

The problem with the homodyne interferometer is that it is not capable of detecting whether or not a change in the intensity is due to a phase shift, or due to the change in the intensity of the signals. The intensity of the signals will usually be altered due to various absorptions and refractions.

The *heterodyne* Mach-Zehnder interferometer (shown to the right in figure 4.1) is overcoming this problem. In this setup, two different sources are used. One with $\omega_1 = 64\,\mathrm{GHz}$, and the other one with $\omega_2 = \omega_1 + \Delta\omega$. $\Delta\omega$ is small compared to ω_1. At TJ-K, $\Delta\omega/2\pi \approx 60\,\mathrm{MHz}$. By using the same calculation as in section 4.1.2, we end up with

$$I_R \propto \frac{s_1^2}{2} + \frac{s_2^2}{2} + s_1 s_2\cos(\Delta\omega t) \tag{4.7}$$

$$I_P \propto \frac{s_1^2}{2} + \frac{s_2^2}{2} + s_1 s_2\cos(\Delta\omega t + \varphi), \tag{4.8}$$

after the low pass filters.

We see from equation (4.7) and (4.8) that the cosines are varying with time. We can therefore find the phase shift by measuring the time t_1 when I_R has a maximum, and compare it with the time t_2 when I_D has a maximum. The phase shift is then

$$\varphi = \frac{|t_1 - t_2|}{\Delta\omega}. \tag{4.9}$$

The interferometer installed at TJ-K is slightly different than presented here. However, the principle of the operation remains the same.

Instead of sending the reference signal through an arm which is equal of length to the plasma arm, the reference signal is sent through a shorter arm. For details, see [14].

---

[5] $I \overset{def}{=} \langle S\rangle$, where $\langle S\rangle = \langle \boldsymbol{E}\times\boldsymbol{B}\cdot\hat{k}/\mu_0\rangle$ is the time averaged pointing vector in the direction of propagation. For monochrome plane waves $B^2 = E^2/c^2$, so $I = c\varepsilon_0 E_0^2/2$.

4.2 The Langmuir probe

The Langmuir probes [15] are often used to diagnose low temperature plasmas. It consist of a thin, isolated wire, and is usually made of wolfram. Typical d of the wire is $200\,\mu$m. The probe tip outside of the ceramic isolation is for the probes at TJ-K $\approx 2\,$mm.

It has the advantages that it offers a simple method to measure the electron density n_e, the electron temperature T_e and the plasma potential ϕ_p. In reference [16], it is explained how the Langmuir probes can be used to obtain the fluctuating quantities, and how they can be used to study turbulence. The disadvantage is however that the the probe can only be used in a environment where the probe itself can survive.

Hot plasmas can transfer sufficient heat in a short time to melt the probe. However, in some cases, probes can be used to measure cold parts of these plasmas, such as the scrape-off layer. In general, measurements with the Langmuir probes are limited to plasmas with $T_e \lesssim 100\,$eV [17].

Measuring with Langmuir probes is an invasive method. Hence the probe will locally perturb the plasma when introduced. Once we know how the probe locally perturbs the plasma, we can deduce information about the plasma (such as n_e, T_e and ϕ_p). To investigate the local perturbation, it is fruitful to look at the particle flux traveling towards the probe.

4.2.1 The basic idea

To explain the basics, let us for simplicity start with a homogeneous, isotropic, unmagnetized, collisionless plasma with cold ions. A derivation from gas kinetics gives us the current from the flux towards one side of a flat probe [18]. We have

$$I = \sum_{p=\{i,e\}} q_p A \Gamma_p = A\frac{1}{4}(qn_i\overline{v}_i + (-q)n_e\overline{v}_e), \tag{4.10}$$

where A denotes the flux surface. Let us now assume that we are introducing a Langmuir probe without any bias into the plasma. Such a probe is referred to as a *floating* probe. Since the mean speed of the electrons usually is higher than the mean speed of the ions (due to their relative mass), electrons will be collected on the probe at first. These electrons will form a *sheath*. After some time, the net current *arriving* at the probe equals to zero due to ambipolarity. The probe will however still be negatively charged due to the first electrons hitting the probe, and will therefore have a potential relative to ground. This potential is called the *floating potential* ϕ_{fl}.

Electrically it can be looked upon as this: The plasma is in contact with the large area of the vessel, which acts as a ground. This area is many times greater than the area of the probe. This implies that the resistance in the Debye-layer be much greater than resistance between the plasma and the vessel, and hence a potential difference will occur.

If we bias the probe negatively, it will start to repel electrons and attract ions. The bias will in other words lead to an ion current (positive electrical current) *towards* the probe. At a certain negative voltage, the ion current towards the probe will saturate. Increasing the negative voltage further would therefore not affect the current. The current where this happens is called the *ion saturation current* I_{sat}. This current can be obtained by simply biasing the probe enough to make sure that the ion saturation current has been reached.

Of course, it is also possible to positively bias the probe. This will repel the ions and attract the electrons. A saturation limit can be reached if the probe geometry can be approximated as planar. The limit for this to happen, is when the probe is biased with the potential of the plasma itself i.e. at the plasma potential ϕ_p. Other geometries will not necessarily lead to a electron saturation current (see section 4.2.2). The biasing explained leads to the characteristic shown in figure 4.2. With our simple assumptions and from basic sheath analysis, the following results can be obtained [8]

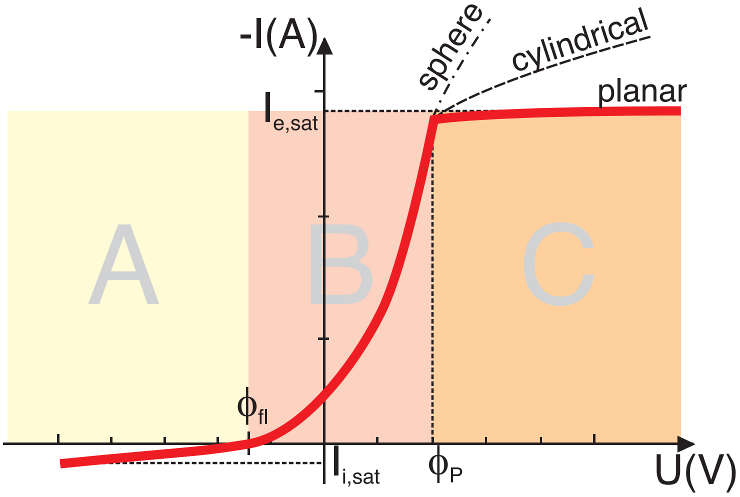

FIGURE 4.2: *Characteristic of a biased probe, where the x-axis represent the potential of the probe, and the y-axis the negative current drawn by the probe. Notice that the unbiased probe has the floating potential* ϕ_{fl} *[4].*

$$\text{(A)} \qquad I = I_{i,sat} = 0.61 q n_e S \sqrt{\frac{T_e}{m_i}} \tag{4.11}$$

$$\text{(B)} \qquad I = I_{i,sat} + I_{e,sat} = I_{i,sat} + I_{e,sat} \exp\left(-\frac{q(\phi_P - U)}{T_e}\right) \tag{4.12}$$

$$\text{(C)} \qquad I = I_{e,sat} = -q n_e S \sqrt{\frac{T_e}{2\pi m_e}}, \tag{4.13}$$

Where S is the effective probe surface.

4.2.2 Complicating factors

The results obtained above are obtained from the the assumptions given in section 4.2.1 . We will in this section briefly discuss some of the things that needs to be taken care of when using the results.

The probe can be considered as planar if the *Debye shielding length* $\lambda_D = \sqrt{\varepsilon_0 T_e / e^2 n_e} \ll d$, where d is the typical probe dimension. In this limit S is close to the real surface of the probe. If $\lambda_D \simeq d$, *orbital motion limits* must be taken into account (see [15]). S is no longer close to the real surface, and geometrical factors tend to increase the current when the bias is increased in this limit. The geometrical factors can be found in reference [19].

If collisions dominates the plasma, the current will be reduced. This is due to the fact that the particles are arriving at the probe due to diffusion rather than to free flight. However, the effects from the collisions may be neglected if the $\rho_L \gg d$, where ρ_L is the Larmor radius.

When a magnetic field is present, the current will also be reduced. Again, the magnetic field may be neglected if $\rho_L \gg d$. For details, see chapter 3.3 in [1].

4.2.3 Operational regimes

In the end the raw output from the Langmuir probe depends on how the probe is biased. There are three different operational regimes, as depicted on figure 4.3. For all three cases in TJ-K, cylindrical tungsten probes with lengths of $\simeq 1\,\mathrm{mm}$ and diameters $\simeq 200\,\mu\mathrm{m}$ are used. The voltages U_2 and U_3 are simultaneously acquired with $R_3 = 1\,\mathrm{k}\Omega$. For a more detailed description of the instruments used at TJ-K, see [20].

At TJ-K, no complicating factors are taken into account when extracting the quantities.

Floating probe operation

The setup of for the floating probe operation is given in figure 4.3a, and it is used to measure ϕ_{fl}. The resistors R_A and R_B makes a $1 : 20$ voltage divider with a total resistance of $1\,\mathrm{M}\Omega$. The ϕ_{fl} might be of interest, as ϕ_p can be hard to measure. Since $I = 0$ at $U = \phi_{fl}$, we can from (4.12) write

$$\phi_p = \phi_{fl} - \frac{T_e}{e} \ln \left(0.061 \sqrt{2\pi \frac{m_e}{M_i}} \right) \tag{4.14}$$

Single bias operation

The single bias operation setup is presented in (4.3b). It is used to measure the ion saturation current. A bias of approximately $-90V$ is applied to ensure that the current

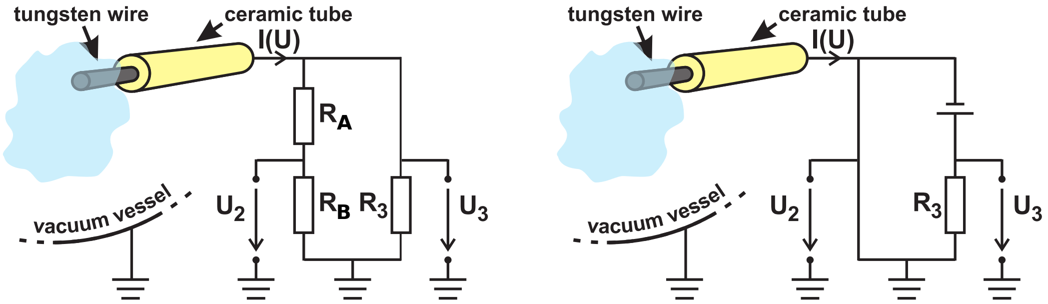

(a) Floating potential (b) Single bias

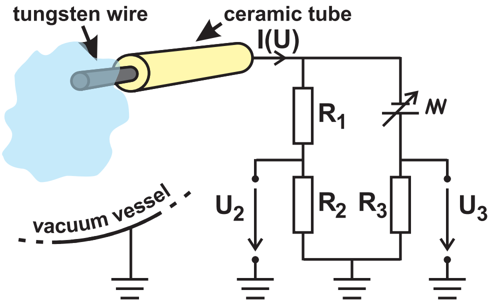

(c) Swept probe

FIGURE 4.3: *The the electric setup for the different Langmuir probe operations [20]. The numeration (a), (b) and (c) is not to be confused with the characteristic regions depicted in figure 4.2, nor equation (4.11) - (4.13)*

has reached the saturation current. The saturation current can be used to find the density profiles. We see from (4.11) that

$$I_{i,sat}(r) \propto n_e(r)S(r)\sqrt{T_e(r)}, \tag{4.15}$$

where r denotes the radial coordinate.

The effective surface $S(r)$ is a measure of how large the particles experiences the target (the probe). It is quite hard to estimate $S(r)$ since this requires detailed knowledge of the trajectories of the particles as presented in [15]. Instead of having a detailed knowledge of $S(r)$, we can estimate $n_e(r)$ by finding how $n_e(r)$ varies with $S(r)$, and in the end make an estimate of n_e by normalizing with the line averaged density $\overline{n}_e$ (see section 4.1).

To find out how $n_e(r)$ varies with $S(r)$, we can use the fact that $S(r)$ is also dependent on ρ_L. Since ρ_L is increasing with increased B_0, the current collected goes down. In the end, a good assumption is that $S(r) \propto 1/B_0(r)$, so that

$$n_e(r) \propto I_{i,sat}(r)B_0(r)\frac{1}{\sqrt{T_e(r)}}. \tag{4.16}$$

We can now find $n_e(r)$ by finding $n'_e(r) = I_{i,sat}(r)B_0(r)\frac{1}{\sqrt{T_e(r)}}$. All we have to do is to find the normalization constant C. We obtain

$$C\overline{n'}_e = \overline{n}_e. \tag{4.17}$$

It is possible to account for the correction of T_e, since both the ion saturation current, and the electron temperature are measured simultaneously during a sweeping mode operation of the probe (see section 4.2.3). During this operation, the probe has to stay fixed at the measuring position while the biasing voltage is being swept between $\pm 100V$. As this takes a certain amount of time, the probe can only measure a few points in the profile of a shot before the temperature of the magnetic coils are too high to continue the shot.

Sweeping operation

In the sweeping operation, the probe is biased with $\pm 100V$ at a frequency of 10 Hz. The electrical setup is presented in figure 4.3c, and the resistors $R_1 = 482\,\mathrm{k\Omega}$ and $R_2 = 24\,\mathrm{k\Omega}$. From this operation, one can obtain the electron temperature T_e. A typical characterization is presented in figure 4.4.

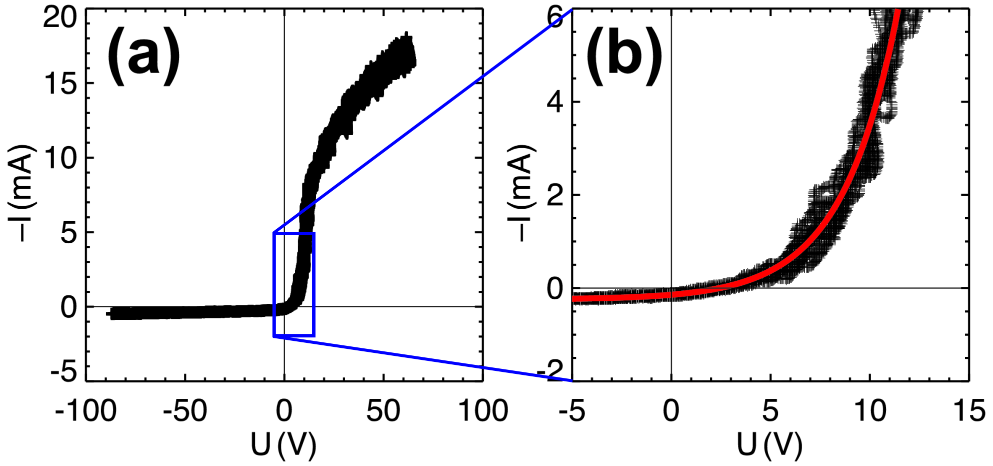

FIGURE 4.4: *The fitting of the swept data for shot #6421 at position $R - R_0 = 6\,cm$ [4]. The black crosses are the measured data, and the red line is the fitted line from equation (4.18).*

By inserting equation (4.14) in (4.12), we get the fitting formula

$$I = 0.61en_eS\sqrt{\frac{T_e}{M_i}}\left[1 - \exp\left(-\frac{e(\phi_{fl} - U)}{T_e}\right)\right], \tag{4.18}$$

which can be solved for T_e.

I is obtained from a Levenberg-Marquardt algorithm, also known as the damped least-squares algorithm [21]. Since the algorithm essentially is finding the curve with the least squared error with respect to the measured data points, it is sensitive to large scatters in the characteristics. This is qualitatively shown in figure 4.5. In this example, the scatter gives a fitted characteristic curve below the actual curve. The fitted curve will therefore have a shallower gradient, and due to equation (4.18) the temperature is overestimated. This happens especially when the density is low, since the characteristics here are relatively flat. As a consequence, the scatter for the electron saturation current is comparable with the ion saturation current.

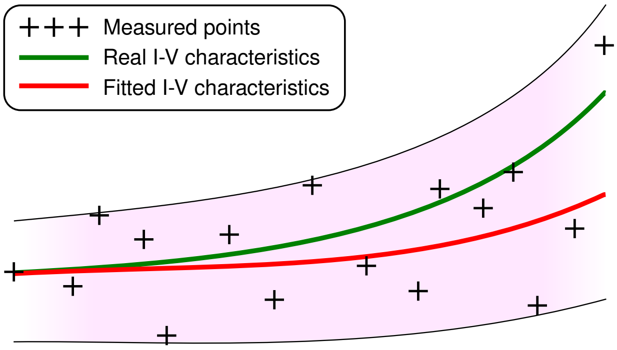

FIGURE 4.5: *Qualitative example where the fitted curve is lower than the real curve due to the scatter in the measured points. The measured points lie within the thin black lines.*

In general, it can be quite hard to estimate the errors for such a fitting routine unless one has other instruments to measure the temperature. One could of course repeated the same measurement several times to give an estimate for the error. However, this can be quite time demanding as it can be challenging to keep the parameters exactly the same for consecutive shots at TJ-K. For this reason the error when measuring T_e has been set to 20%, since one do not expect errors larger than this.

4.2.4 The three pin probe

In the scope of this thesis, a three pin probe have been used at the 1-D probe device as depicted in figure 3.1.

One of the probes is used in the single bias operation, and is measuring the ion saturation current. From this, one can estimate n_e once T_e and B_0 is known, as described above. Another probe is used in the floating probe operation, and is measuring the floating potential. The data from this probe is not used in this thesis, but the data is stored for use in the future. The third probe is used in the sweeping operation. By using the fitting routine, the temperature for each position can be obtained.

4.3 The bolometer

A bolometer is a device which is capable of measuring electromagnetic radiation. This is in particularly of importance for fusion devices, as the bolometers can indicate how much energy which is lost from the plasma due to radiative processes. Even if the core of the fusion plasmas are hot enough not to radiate large amounts of energy, the outer parts of the plasma is cool enough to radiate large amounts of energy [1].

A plasma can radiate either through purely radiative processes, or through collision induced processes. In either way, one can categorize the radiation into three groups: Line radiation, recombination and bremsstrahlung (for details see [22]). In TJ-K, the plasmas generated are relatively cool ($T_e < 30\,\mathrm{eV}$). Hence, the line radiation is much larger than for recombination and bremsstrahlung [23].

There are mainly two types of bolometers used in fusion research. Namely the semiconductor bolometer and the metal foil bolometer. The semiconductor has the advantage of high temporal resolution in the microsecond range, and can be used in investigation of edge localized modes (ELM). However, at present day, these bolometers do not have wide spectral adsorption range. In addition, the semiconductors are subjected to radiation induced degeneration [24]. The metal film bolometers can have a wide spectral range if the foil material is chosen properly. In addition, the foil need to be of a certain thickness to cover the desired spectral range. This reduces the temporal resolution due to thermal conduction through the material, so for the bolometers installed at TJ-K the temporal resolution is around 2 ms [22].

In TJ-K, a bolometer with gold foils is used. It measures the incoming radiation through measuring the change in resistivity of a known resistor.

4.3.1 The device

The bolometer consists of two bolometer heads, where each head contains four measuring channels with one corresponding reference channel to each measuring channel (see figure 4.6a).

The bolometer housing consist of two cylindrical segments as depicted on figure 4.7, and is installed on port O-5. The bolometer heads are located in the plasma facing segment, which is at the same pressure as the rest of the vacuum vessel. The head is placed approximately 350 mm from the plasma center. A mesh is placed in front of this segment, and shield the bolometers from microwave radiation. The mesh is around 75% transparent for visible light. The bolometer heads are connected to the electronics in the second cylindrical segment through vacuum feedthroughs.

An adjustable aperture of $8 \times 14\,\mathrm{mm}^2$ is placed just before the two bolometer heads. This make the bolometer work according to the principle of a *camera obscura*, and is hence called a bolometer camera. The entire poloidal angle of aperture is about $\pm 28^\circ$, the toroidal $\pm 11^\circ$. The poloidal angle of the individual channels through the aperture is approximately 11°.

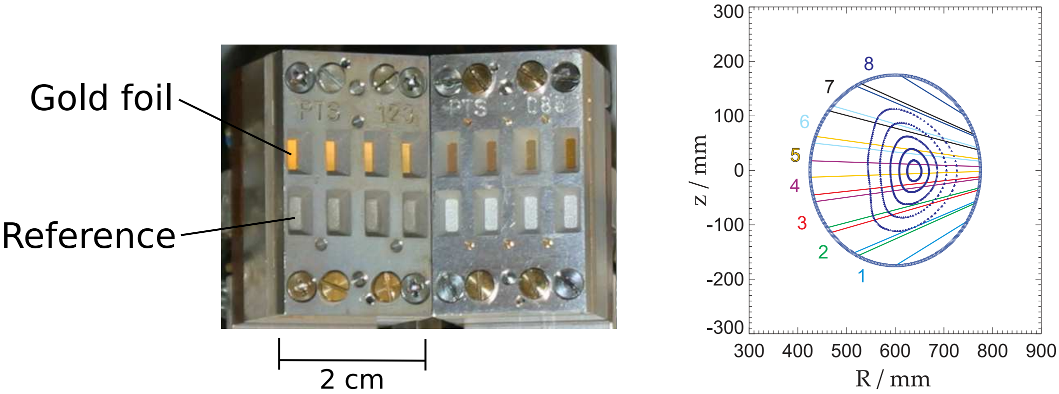

(a) A picture of the two bolometer heads, tilted towards each other [23].

(b) The bolometric line of sight. From [22].

FIGURE 4.6: *The bolometer heads with its respective line of sight.*

In contrast to the first segment, the second segment has a atmospheric pressure. In this second segment, the lock-in amplifier is located. The lock-in amplifier is modulating the signal with a carrying wave with known frequency ω. The signal is multiplied with a square wave with the same phase and frequency. In the end a low pass filter is picking out only the DC component of the signal. In that way noise with different frequencies than the carrying wave is filtered out. The lock-in amplifier is used since the signal to noise ratio directly from the bolometer heads are relatively low [22].

The bolometer is designed to withstand temperatures up to 150°C, and magnetic fields up to 4.5 T. Furthermore, they are largely insensitive to radiation damage by neutrons and gamma radiation [25].

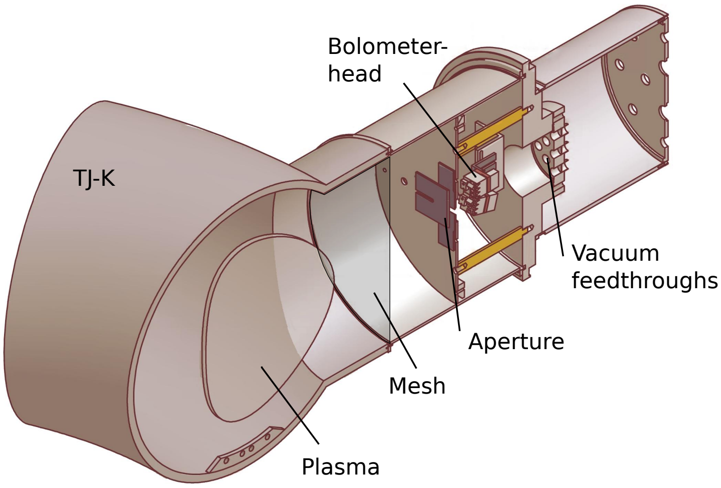

FIGURE 4.7: *The bolometer as installed in TJ-K [23].*

The bolometer head

As described in section 4.3.1, the bolometer consist of two bolometer heads. One such head has the dimensions $2 \times 3.3 \times 1.5\,\mathrm{cm}^3$, and is shown in detail in figure 4.8. The foremost part of the head consist of cooling plate made out of aluminum. Windows for the measuring channels are carved out, whereas the reference channels are cover with 0.6 mm of aluminum [23]. This cover shields the underlying gold foils against radiation in the spectra ranging from visible light to soft X-rays. In addition it provides a cover against neutral particles.

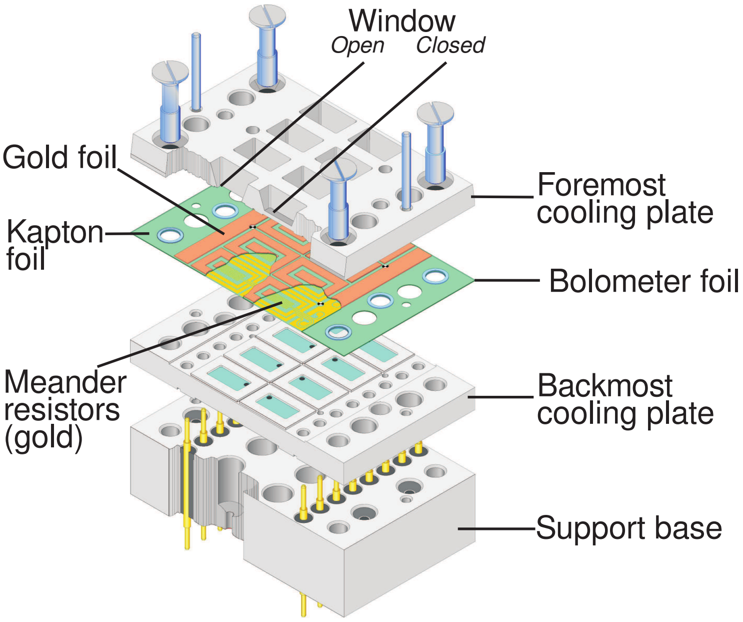

FIGURE 4.8: *Detailed view of one of the bolometer heads [24].*

The bolometer foil is located below the foremost cooling plate. It consists of absorbing gold foils atop of a Kapton foil atop of meander resistors made of gold. The $7.5\,\mu$m Kapton foil serves as a conductor for heat and isolator for the electricity. There are eight absorbing gold foils on the bolometer foil. One for each measuring channel, and one for each reference channel. Each gold foil is $4\,\mu$m thick, and has an absorbing area of $1.3 \times 3.8\,\mathrm{mm}^2$. The adsorption spectra is shown in figure 4.9.

Finally 16 meander resistors of gold are deposited on the back of the Kapton film, directly below the absorbing gold foil. There are two resistors per measuring channel (referred to as R_{M1} and R_{M2} for one channel), and two resistors per reference channel (referred to as R_{R1} and R_{R2} for one channel). Each resistor pair is interleaved in a meander like form. The resistors have a resistance of approximately $1.6\,\mathrm{k}\Omega$ each, and are connected so that one measuring channel together with one reference channel are forming a Wheatstone bridge (see figure 4.10).

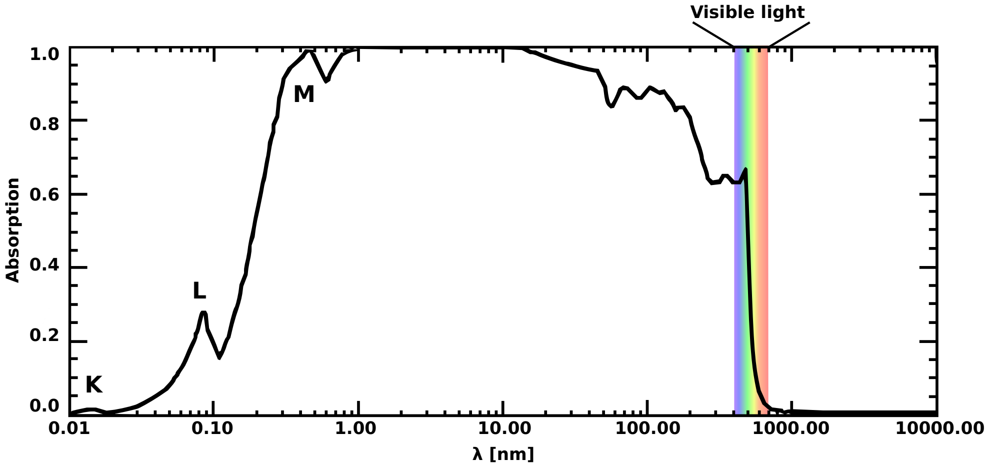

FIGURE 4.9: *The absorption* 4 *µm thick gold foil [26].*

The eight measuring channels covers the the whole range of the poloidal cross section (see figure 4.6b). Since the different lines of sights covers different amounts of magnetic surfaces, one can use Abel inversion to deduce the *radial* radiation profiles if one assumes poloidal symmetry. If a poloidal symmetry cannot be assumed, one can still find radial profiles through tomography with two or more bolometers with overlapping lines of sight.

4.3.2 Measuring the radiated power

Figure 4.10 shows the schematic circuit for one of the measuring channels with the corresponding reference channel. By knowing how the the radiated power is absorbed in the gold foil, it is possible to relate ΔU_{LI} to the absorbed radiated power P_{abs}.

Let us assume that all the four resistors are identical. If we apply the voltage U_{AC}, the resulting voltage $U_B = 0$ if all the resistors have the same temperature. If the bolometer is irradiated, then the temperature of the measuring resistors will rise. Thus the resistance of these resistors will also change, and $U_B \neq 0$.

We can relate the absorbed irradiated power P_{abs} on the gold foil and U_B. Let us call the heat in the bolometer foil for Q_B. We note that the change of heat in the bolometer foil per time depends on the absorbed irradiated power P_{abs} and the power lost to the surroundings P_{loss}. We have

$$\frac{\mathrm{d}}{\mathrm{d}t} Q_B = P_{\text{abs}}(t) - P_{\text{loss}}(t). \tag{4.19}$$

The loss can be found form Stefan-Boltzmann's law if we neglect heat losses due to convection. This is a good approximation due to the low pressures in TJ-K ($p \sim 10^{-3}$ Pa) [26]. Stefan-Boltzmann's law applies for black bodies, and states

$$\frac{P}{A} = \sigma T^4, \tag{4.20}$$

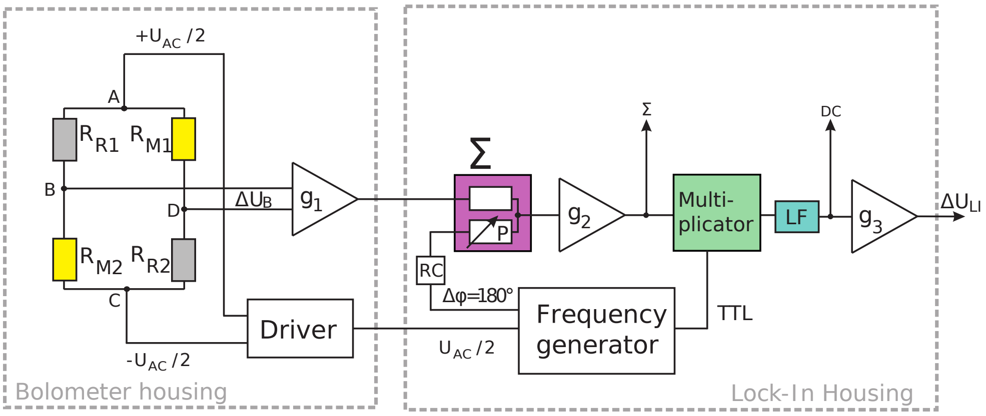

FIGURE 4.10: *A schematic circuit for one of the Wheatstone bridges (containing one pair of the measuring resistors R_{M1} and R_{M2}, and the corresponding pair of reference resistors R_{R1} and R_{R1}) together with its lock-in amplification.*
The Wheatstone bridge is excited with a sinusoidal signal coming from the driver and frequency generator. The bridge voltage ΔU_B is amplified by the instrumentation amplifier g_1, and adjusted to zero by the summer circuit Σ prior to the the measurement. This is followed by another amplifier g_2, and by the multiplier modules. Finally, the signal is time averaged and filtered through the low-pass filter before amplified one last time through g_3. The output voltage ΔU_{LI} is the voltage acquired during the experiments [22].

where A is the surface area of the body, and $\sigma = 5.67\ldots \cdot 10^{-8} \frac{\mathrm{W}}{\mathrm{m}^2\,\mathrm{K}^4}$ is the Stefan-Boltzmann constant. For non-black bodies, the radiation can be found by multiplying with the emissivity ε, which is a fraction of how much power the body radiates compared to a perfect black body.

Let us call T_B for the temperature of the bolometer foil, and T_S for the temperature of the surroundings. The temperature of the surroundings is for all practical purposes the temperature of the cooling plates. That means that the power lost due to radiation from the bolometer foil (due to increase in temperature) can be written as

$$P_{\text{loss}} = 2A\sigma\varepsilon_{\text{Au}}(T_B^4 - T_S^4) \;\Rightarrow\; P_{\text{loss}}(t) = k(T_B(t) - T_S(t)) = k(\Delta T(t)), \tag{4.21}$$

where the factor 2 comes from the fact that the foil has two sides with area A.

Further on, assuming that the bolometer foil has a constant pressure during the heating, we have from first principles that $(\partial_T Q)_p = C_p$, so

$$\frac{\mathrm{d}}{\mathrm{d}t} Q_B = C_p \frac{\mathrm{d}}{\mathrm{d}t} T_B, \tag{4.22}$$

where C_p is the heat capacity of the whole bolometer foil. If we assume that the cooling plates are operating in a steady state, we can write

$$\frac{\mathrm{d}}{\mathrm{d}t}\Delta T = \frac{\mathrm{d}}{\mathrm{d}t}(\Delta T_B - \Delta T_S) = \frac{\mathrm{d}}{\mathrm{d}t}T_B - 0 \tag{4.23}$$

$$\frac{\mathrm{d}}{\mathrm{d}t}\Delta Q = \frac{\mathrm{d}}{\mathrm{d}t}(\Delta Q_B - \Delta Q_S) = C_p\frac{\mathrm{d}}{\mathrm{d}t}T_B - 0. \tag{4.24}$$

If we use $\tau \equiv \frac{C_p}{k}$, substitution of equation (4.19), (4.21) and (4.23) into equation (4.24) yields

$$P_{\text{abs}}(t) = C_p\left(\frac{\mathrm{d}}{\mathrm{d}t}\Delta T(t) + \frac{\Delta T}{\tau}(t)\right) \tag{4.25}$$

Let us now say that R_0 is the resistance before the irradiation, and that $\Delta R = R(t) - R_0$. Then, any of the resistors in the Wheatstone-bridge can be described by [25]

$$R(t) = R_0(1 + \alpha\Delta T(t)) \;\Rightarrow\; \Delta T = \frac{\Delta R - 1}{R_0\alpha} \overset{\Delta R \gg 1}{\simeq} \frac{\Delta R}{R_0\alpha}. \tag{4.26}$$

α is the temperature coefficient, and for the gold meanders $\alpha = 3.9 \cdot 10^{-3}K^{-1}$.

If we in addition define $\kappa \equiv C/\alpha\tau$, we get

$$P_{\text{abs}}(t) = \frac{\kappa}{R(T_0)}\left(\tau\frac{\mathrm{d}\Delta R(t)}{\mathrm{d}t} + \Delta R(t)\right). \tag{4.27}$$

We would now relate equation (4.27) this to our circuit. By looking at figure 4.8, we see that

$$U_{AB} = U_{AC}\frac{R_{R1,0}}{R_{R1,0} + R_{M2,0} + \Delta R_{M2}} \tag{4.28}$$

$$U_{AD} = U_{AC}\frac{R_{M1,0} + R_{M1,0}}{R_{R2,0} + R_{M1,0} + \Delta R_{M1}} \tag{4.29}$$

With the assumption that all the resistors in the bridge are equal, and by that also assuming that the change of resistance in R_{M1} and R_{M2} is the same, we get (following [27])

$$\Delta U_B = U_{AD} - U_{AB} = U_{AC}\left(\frac{R_0 + \Delta R}{2R_0 + \Delta R} - \frac{R_0}{2R_0 + \Delta R}\right) \tag{4.30}$$

$$= U_{AC}\frac{\Delta R}{2R_0 + \Delta R} \approx U_{AC}\frac{\Delta R}{2R_0}. \tag{4.31}$$

Solving this relationship with respect to ΔR gives

$$\Delta R = 2R_0\frac{\Delta U_B}{U_{AC}}. \tag{4.32}$$

If we substitute equation (4.32) into equation (4.27), we obtain

$$P_{\text{abs}}(t) = \frac{2\kappa}{U_{AC}} \left(\tau \frac{\mathrm{d}\Delta U_B(t)}{\mathrm{d}t} + \Delta U_B(t) \right). \tag{4.33}$$

According to [28], a more precise description is

$$P_{\text{abs}}(t) = \frac{2\kappa}{U_{AC}} (R_{OH} + 2R_C) \sqrt{g_C} \left[\tau \frac{\mathrm{d}\Delta U_B(t)}{\mathrm{d}t} + \Delta U_B(t) \left(1 - \frac{U^2_{AC}\beta}{4\kappa} \right) \right] \tag{4.34}$$

$$g_c = 1 + (\omega C_C R_{\text{eq}}) \tag{4.35}$$

$$\beta = \frac{1 - (\omega C_C R_O H)^2 + (\omega C_C R_C)^2}{1 + [\omega C_C (R_O H + R_C)]^2}, \tag{4.36}$$

which incorporates the effects from the cable connecting the output from the Wheatstone-bridge to the preamplifier. R_{OH} denotes the resistance of the bridge without any irradiation and R_{eq} is the bridge's equivalent resistance. R_C and C_C is the resistance and the capacitance of the cable between the bridge output and the preamplifier, and ω is the excitation frequency. At TJ-K, the cable used is 30 cm long with $R_C \approx 0.1$ and $C \approx 50\,\text{pF}$ [23] . With $\omega \approx 2\pi \cdot 133\,\text{Hz}$, $\beta = 1$ and $g_C = 1$ serves as good approximations. In addition the last term in (4.35) is negligible. Thus equation (4.33) is a good approximation.

In the end U_{LI} is measured. Reference [22] gives the following equation for relating the irradiated power to U_{LI}

$$P_{\text{abs}}(t) = \frac{\pi}{g} \frac{2\kappa}{U_{AC}} \left(\tau \frac{\mathrm{d}\Delta U_{LI}(t)}{\mathrm{d}t} + \Delta U_{LI}(t) \right). \tag{4.37}$$

In equation (4.37) $g = 2g_1g_2g_3$, with $g1 = 30$, $g2 = 100$ and $g3 = 5$. κ and τ is determined by calibration of each single channel. These constants are given in table (4.1)

Bolometer	Channel 1	Channel 2	Channel 3	Channel 4	Channel 5	Channel 6	Channel 7	Channel 8
κ [W]	0.428	0.435	0.426	0.455	0.537	0.534	0.509	0.534
τ [ms]	119.32	112.95	118.64	114.32	79.09	78.18	78.18	78.54

TABLE 4.1: *Calibration constants for the different bolometer channels [22].*

4.4 The optical diode

An optical diode is used for detecting radiation with wavelengths in the visible spectrum. A silicon Positive Intrinsic Negative (PIN) photo diode of the type SIEMENS, BPX 61 [29] is installed at the upper port T 5. Together with the bolometer, it can be used to detect if the radiation emitted by the plasma is shifting to higher frequencies.

The PIN photo diode is characterized by very short switching times. The diode used at TJ-K has a switching time of $\simeq 20\,\mathrm{ns}$. By an appropriate circuit of the amplifier a rising time of 2 ms can be achieved. This gives enough resolution to investigate the energy confinement time τ_E, as described in [22]. The radiation-sensitive area of the diode has a diameter of $\varnothing = 5.8\,\mathrm{mm}$. The diode is sensitive in the spectrum ranging from 400 nm to 1100 nm, and thus covers the entire visible range of the radiation. Figure (4.11) shows the relative spectral sensitivity of the diode as a function of the wavelength.

A voltage change of $\Delta U_{\mathrm{Diode}} = 1\,\mathrm{V}$ corresponds to $16.13\,\mu\mathrm{W}$.

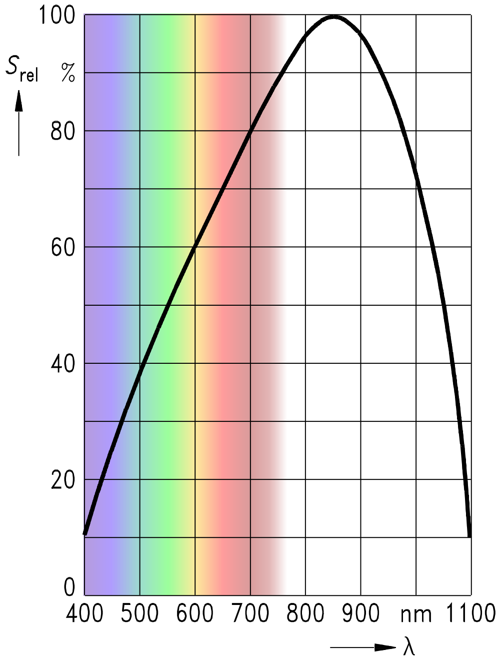

FIGURE 4.11: *Relative sensitivity as a function of the wavelength λ [29].*

Chapter 5

Results

In this section the results obtained in this thesis will be presented. First, a presentation of the results from the magnetic field scan will be given, followed by the results of the pressure scan. In a scan the scan parameter is varied on a shot to shot basis while all the other quantities are kept constant. If nothing else is given, the parameters for a given shot is given in table 5.1. Shots with a too high deviation in the values presented in table 5.1 have been discarded.

Gas	B_0 [mT]	Pressure [mPa]	Current ratio	Injected power [kW]
H	411	4.3	0.5775	1.5
He	413	18.9	0.5775	1.5
Ne	412	22.1	0.5775	1.5
Ar	417	21.5	0.5775	1.5

TABLE 5.1: *Table of the standard parameters of the shots performed in this thesis. The current ratio is the ratio between the helical and vertical field coils.*

In the results presented, the plasma is assumed to be in a steady state, since the time signal from the interferometer has been flat during the data acquisition. This is shown in figure 5.1. If the interferometer signal varied during the acquisition time in a shot, the shot was discarded, and is not presented here.

Although hydrogen shots have been performed, they are not represented in all the plots. The reason for this is that the probe measurements in hydrogen have globally disturbed the plasma so that the interferometer signal is no longer flat. Also the shots done with hydrogen are less reproducible than the other gases investigated. Meaning that even if all the external parameters have been held constant, the results from hydrogen shots sometimes differs considerably from each other as compared with other gases.

It should also be stressed that, unless stated otherwise, the error bars in the following plots represents the *standard error of the mean* $SE_{\overline{x}}$. To calculate $SE_{\overline{x}}$ the *corrected sample*

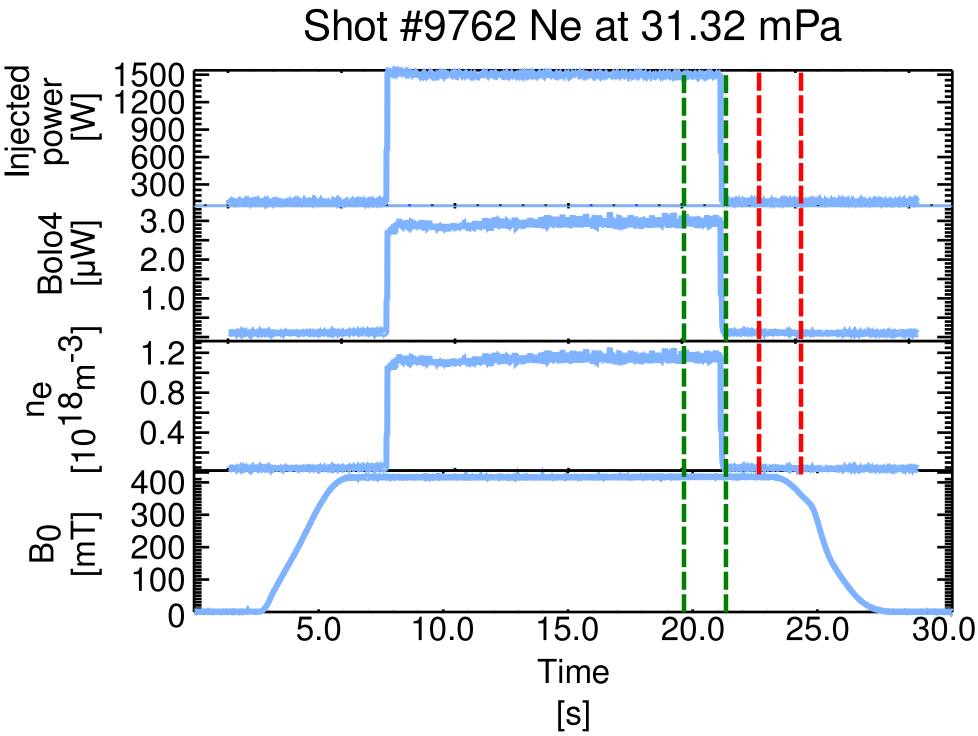

FIGURE 5.1: *The time trace for a typical shot performed in this thesis. The green dashed line indicates the range where a mean value has been acquired. The red dashed line indicates the range of the offset subtracted from the mean.*

standard deviation have been used together with the assumption that the data is Gaussian distributed [30].

5.1 Variation of magnetic field

The 14 GHz system allows TJ-K to be operated at higher magnetic fields. A higher magnetic field corresponds to a higher magnetic pressure. As a consequence, higher kinetic pressure can be stored in the equilibrium. This means that more energy can be stored in the plasma since

$$W \approx 3V\overline{n}(\overline{T_e} + \overline{T_i}), \tag{5.1}$$

where W denotes the kinetic energy [6]. This is indeed what is observed in figure 5.2.

Some notes should be done about the errors in figure 5.2 though. We see from equation (5.1) that it is a function of T_i. The ion temperatures, however, have not been measured in this thesis.

On the other hand, this has been done earlier for the 2.45 GHz, and the 8 GHz systems. Reference [31] explains how the temperature is estimated by measuring the the diamagnetic drift and by using LIF measurements (in the case of argon). It has

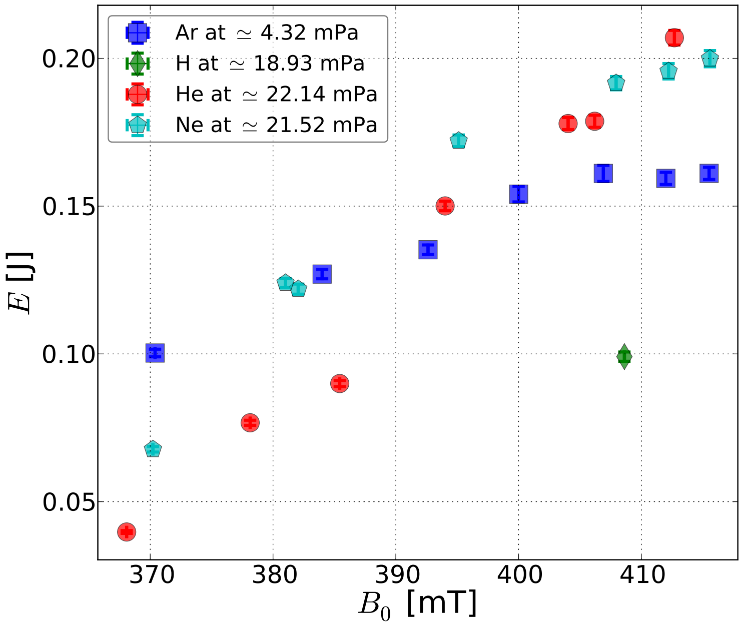

FIGURE 5.2: *The confined energy as a function of* B_0. *See the text regarding assumptions and the errors in this plot.*

been found that the ion temperature increases for decreasing pressure (in the range of interest), and that higher magnetic field yields higher T_i.

Based on those results, and by taking into account that the plasma parameters in the 14 GHz regime are somewhat different, T_i in equation (5.1) has been set to 1 eV (without any deviation) for all plasma parameters. This is an oversimplification, but it serves as an indicator for how the confined energy scales with B. In the end the ion temperature should be measured in further works to estimate the confined energy more correctly.

5.1.1 Positioning of the electron cyclotron resonance layer

In this work heating at the fundamental electron cyclotron resonance (ECR) has been aimed. In theory it would also be possible to heat the plasma at the *upper hybrid resonance*, or with electron Bernstein waves as described in [4].

Attempts on igniting the gas to plasma at the second ECR harmonic have also been done, but without any results. Also attempts of starting the plasma at the fundamental ECR frequency, and then reducing the magnetic field so that heating at the second ECR harmonic is possible have been done, but with the only result that the plasma is extinguished back to the neutral gas phase. However, it is thought that it would be possible to ignite and heat the plasma with higher injected power. A higher injected power will be available after installing the third 14 GHz klystron (see section 3.1). Another possibility would be to install a lens to increase the power density in the injected microwave.

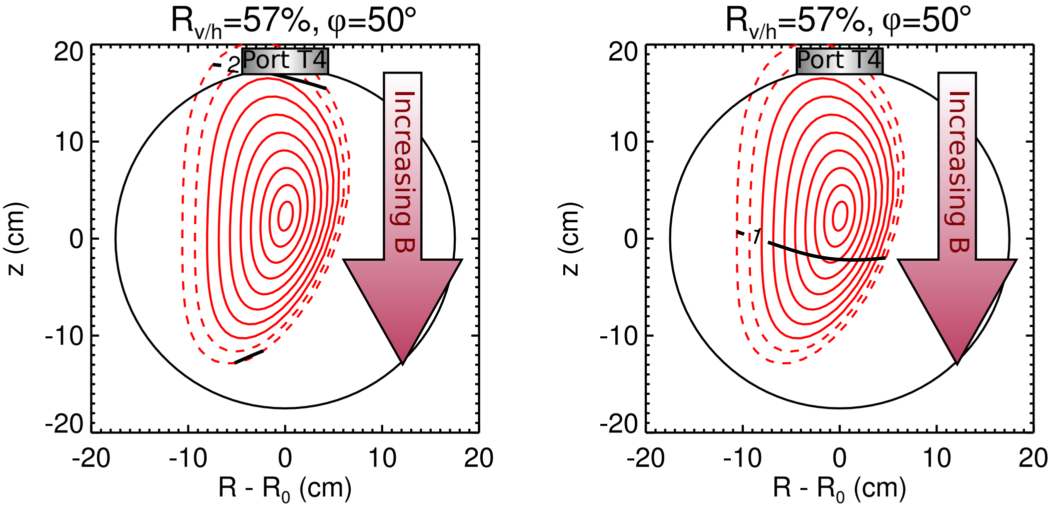

(a) $B_0 \approx 370\,\mathrm{mT}$ (b) $B_0 \approx 440\,\mathrm{mT}$

FIGURE 5.3: *Magnetic flux surfaces together with the position of the fundamental ECR-layer (annotated with the number* 1*) at* $B_0 \approx 370\,mT$ *and at* $B_0 \approx 440\,mT$*. The second harmonic of the ECR can be seen at* $B_0 \approx 370$*, and is annotated with the number* 2*. Notice that* B *is increasing for decreasing* z *at* $\varphi = 50$*. This is not the case* $\forall \varphi$ *due to the complex magnetic field topology of the stellarator. The dashed lines in the figure are the loci of the magnet field lines beyond the separatrix.*

The fundamental electron resonance is given in equation (2.25). By rearranging equation (2.25), and substituting the resonance frequency with 13.75 GHz, one finds that the cyclotron resonance will occur in the plasma where the magnetic field is $\approx 491\,\mathrm{mT}$. When varying the magnetic field, one will therefore effectively vary the position of the resonance layer. This is apparent from figure 5.3[1] ,which shows where the fundamental ECR-layer (from now on the word "fundamental" will be omitted when it is obvious) is situated in the plasma for two different magnetic fields. One can see that the ECR-layer moves towards increasing z for increasing B_0.

The plasma pressure, and hence the confinement will be affected when moving the ECR-layer. This can be described as follows: As the ECR-layer is moving towards the center, the absorption area will increase. The coupling between the wave and the plasma will therefore be stronger. Close to the center the change in absorption area when moving the ECR-layer will decrease, and so will the change in the coupling. In addition, the closer to the center the layer comes, the more flux surfaces it will intersect. Due to collisions (explained in 2.2), the particles in these outermost flux surfaces will have a poorer confinement compared with those in the center. In addition, there will be a reduction in the mean free path as the density is increasing towards the center (as

---

[1] The magnetic flux surfaces in figure 5.3 are obtained from a Poincaré plot of field lines equally spaced in the radius at one point in the torus. Since the flux surfaces are not equally spaced in the field strength B, one can not from this plot alone deduce the strength of the magnetic field.

will be shown in section 5.1.4). Because of this, it is plausible that the particles do not have enough energy for ionization processes[2], and that the energy will be transferred to transitional states in the atoms in the plasma instead. However, as the slope of the ionization is changing only slightly at high magnetic fields (as seen in figure 5.20), the effect is not considered to have a large effect.

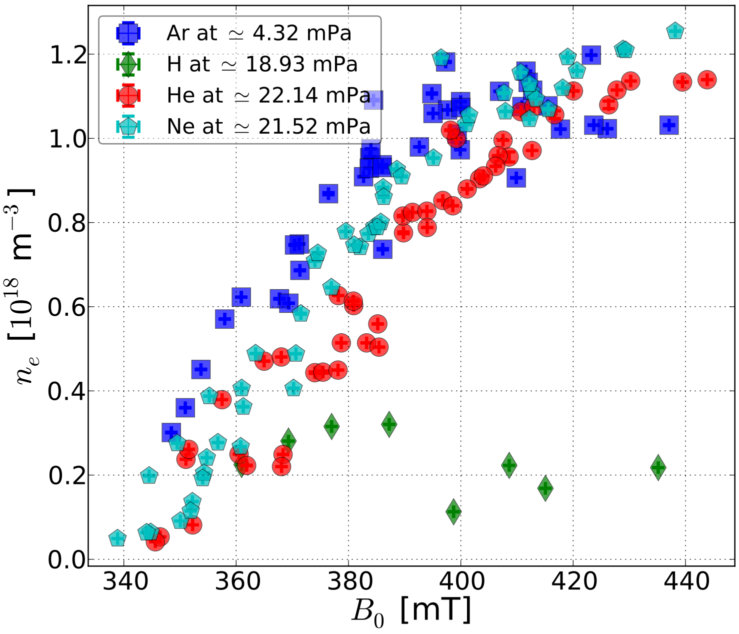

FIGURE 5.4: *Line average density plotted against* B_0*. Note that the different gases have different base pressures. The reason for this is mainly due to practical reasons. It is found that with much lower densities, it can be problematic to ignite the plasma.*

Based on this, if we plot the line averaged density as a function of the magnetic field, we would expect saturations at low and high magnetic fields. This is indeed what we see in figure 5.4. Notice that hydrogen is behaving somewhat unexpended. There might be several reasons for this. Firstly it is the lightest of all gases, which affects the dynamics of the particles, secondly, it is observed that hydrogen has the highest electron transport, and might also have a high ion transport (this needs of course to be investigated). At last, this gas is the only non-noble gas investigated, and the dissociation of the molecules might affect the plasma (see table 5.2 for atomic details).

5.1.2 Interaction with cut-offs and other resonances

Even though we are only considering plasmas heated with the ECR, other cut-offs and resonances comes into play. The other resonances and cut-offs of importance here are given in section 2.1.2.

---

[2] Note that the cross section for ionization varies for different gases, as stated in [32].

Gas	Atomic number	Dissociation	First ionization	Second ionization
H_2	-	4.518 eV	-	-
H	1	-	13.59844 eV	-
He	2	-	24.58741 eV	54.41778 eV
Ne	10	-	21.5646 eV	40.96328 eV
Ar	18	-	15.75962 eV	27.62967 eV

TABLE 5.2: *Energy levels for the gases investigated in this thesis [33, 34].*

The first of importance is the density cut-off, where the plasma becomes so thick that the wave can no longer propagate, and is being reflected. This happens if the injected wave is close to the plasma electron frequency given in equation (2.22). By rearranging equation (2.22), and substituting the cut-off frequency with 13.75 GHz, we find that $n_{e,\text{cutoff}} \simeq 2.35 \cdot 10^{18}\,\text{m}^{-3}$. It can also be noted that in over-dense plasmas, the density cut-off is shielding the plasmas from the injected wave. Bernstein waves created by the O-X-B conversion can then be used, as explained in [4, 12].

The third frequency of importance is the *upper hybrid resonance* (UHR). As apparent from equation (2.26), ω_{URH} is a function of B and n_e. Depending on the plasma parameters, this layer is shielded by the right and left cut-offs (equations (2.23) and (2.24) respectively). Although this resonance is only available for X-mode waves, it can be reached by our injected O-mode wave due to X-mode excitations. The X-modes can be excited either by reflections in the vessel, or by reflections at the cyclotron resonance if the injected wave is hitting the layer at certain angles [35, 36].

The interaction between the different frequencies and the input frequency for high and low fields is found in figure 5.5. A cut-off or resonance is found whenever its curve is intersecting with the input frequency.

5.1.3 Profiles acquired through Langmuir probe measurements

By using the three pin probe as described in section 4.2.4, the density profiles and the temperature profiles was obtained. An explanation on how the data was acquired, and how the plots should be read are given before the results are presented.

Acquiring data with the probes

One profile is acquired per shot at a constant scanning parameter (the scanning parameter is either the magnetic field or the base pressure). Due to limitations in the shot time, only data in four positions has been acquired for each profile. Data acquisition are performed in the positions $R - R_0 = 4$, 8, 12 and 16 cm. The density and temperature for each point have been estimated as explained in section 4.2.1. The values obtained have been used to calculate the collisionality and the transport. By

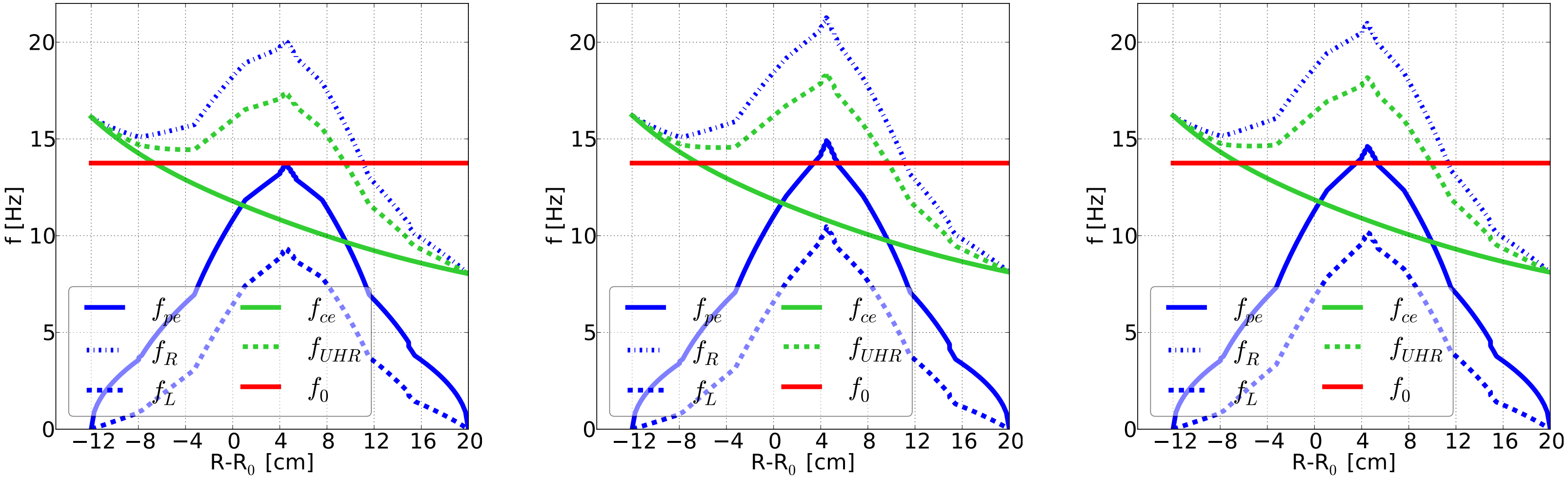

(a) Frequencies for He at $B_0 \approx 413\,\mathrm{mT}$ (b) Frequencies for Ne at $B_0 \approx 416\,\mathrm{mT}$ (c) Frequencies for Ar at $B_0 \approx 415\,\mathrm{mT}$

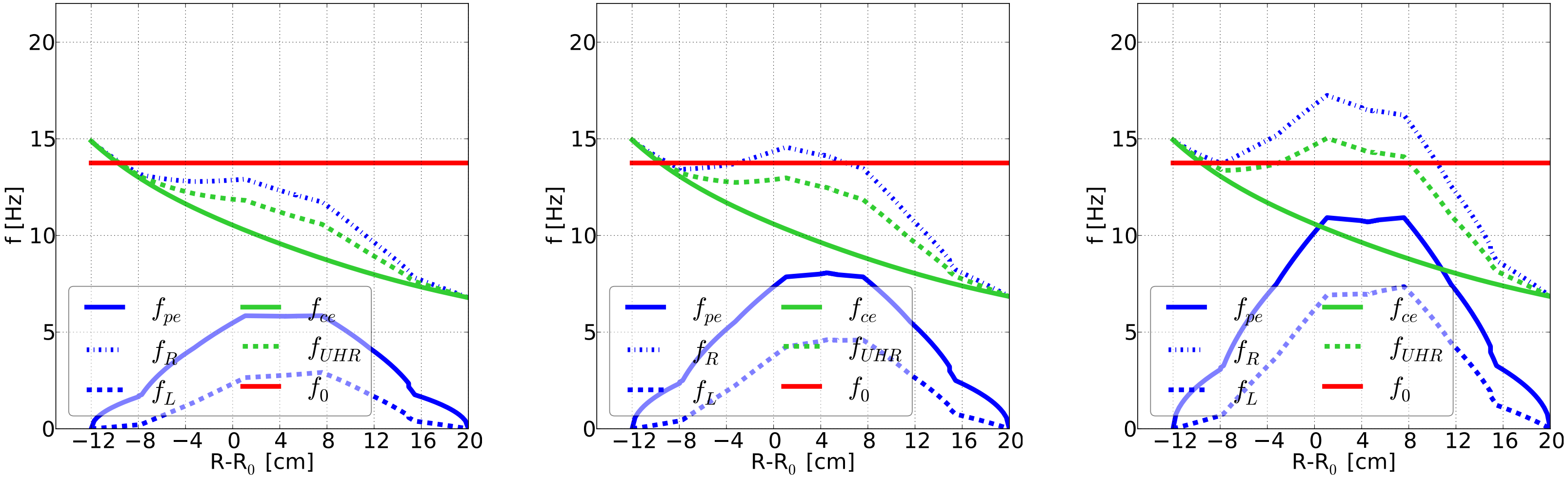

(d) Frequencies for He at $B0 \approx 368\,\mathrm{mT}$ (e) Frequencies for Ne at $B0 \approx 370\,\mathrm{mT}$ (f) Frequencies for Ar at $B0 \approx 370\,\mathrm{mT}$

FIGURE 5.5: *Cut-offs (blue), resonances (green) and the input frequency (red).*

using the proper line averaging, the confined energy and the diffusion coefficient have been calculated.

The probe was first injected in the plasma, and on its way back the probe was recording the data in these discrete positions. At a subsequent shot in the scan, the scanning parameter has been varied. All other parameters have been kept constant.

Explanation of the plots

In the following sections, figures with three subplots (one contour plot and two line plots) are going to be presented. The contour plot is considered to be the main plot. However, as it can be difficult to deduce numbers from colors, and since errors cannot be displayed in a contour plot, the two line plots are added.

In the contour plot , the position is found on the $x-$axis, the scanning parameter (magnetic field or pressure) is found on the $y-$axis, and the density (or the relevant quantity) is found on the $z-$axis. A linear interpolation has been made between the four positions in the profile for one shot. Further on, a linear interpolation has been made between the different shots. Black dashed lines have been included in the plot to indicate at what scanning parameter a non interpolated shot has been performed. Thus, the interpolated values should be handled with care. Even though the resolution of this plot is low, it serves the purpose of visualizing the general trends as the scanning parameter is varied.

The bottom most line plot is a plot of three profiles corresponding to actual non-interpolated shots at the lowest scanning value, the intermediate scanning value, and the highest scanning value. The left most line plot shows how the profile quantity at the four different positions (where the data has been acquired) varies with the scanning parameter.

5.1.4 The density profiles

In figure 5.6, 5.7 and 5.8 we can see how the densities increase with increasing magnetic field. Even if the power is not deposited in the center, we can see that the profiles are peaked. This might appear somewhat counter-intuitive, but the peaked equilibrium shape is a consequence of the transient phase the plasma goes through before it reaches its equilibrium.

A detailed explanation of why the shapes are peaked is given in [37]. Basically the explanation is given by the transport equations (when neglecting convective terms) for density and temperature

$$\frac{\partial n}{\partial t} = -\nabla \cdot \Gamma_n + n_0 n \langle \sigma v \rangle_{\text{ionization}} - n^2 \langle \sigma v \rangle_{\text{recombination}} \tag{5.2}$$

$$\frac{3}{2}\frac{\partial T}{\partial t} = -\frac{3}{2n}\nabla \cdot (T\Gamma_n) + \frac{1}{n}\nabla \cdot Q + \frac{P}{n} - n_0 \left(\langle \sigma v \rangle E \right)_{\text{ionization}} - n_0 \langle E \rangle \langle \sigma v \rangle_{\text{neu coll}}, \tag{5.3}$$

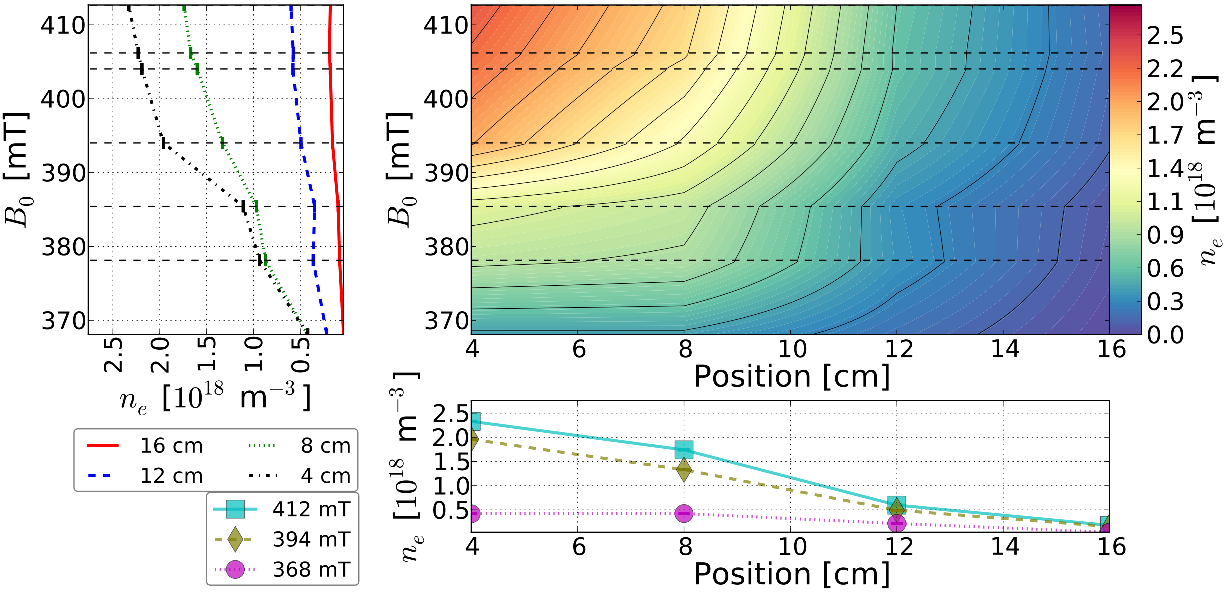

FIGURE 5.6: *Density profiles for helium at and various magnetic fields.*

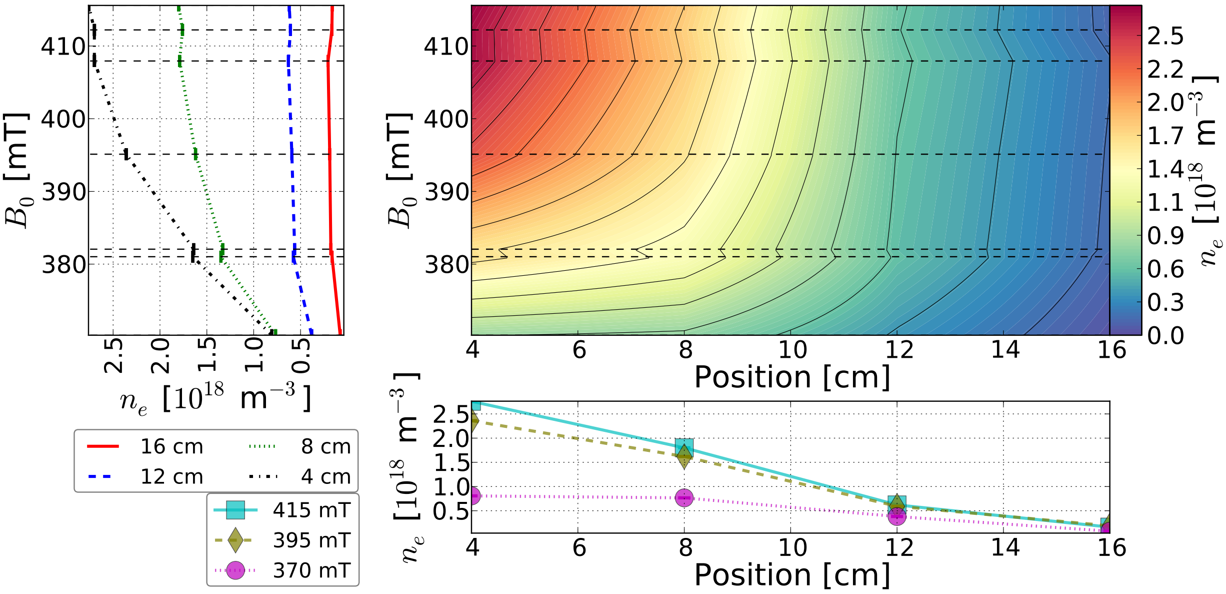

FIGURE 5.7: *Density profiles for neon at and various magnetic fields.*

where n_0 denotes the neutral particle density, σ denotes the cross-section of the respective reaction (*neu coll* is an abbreviation for collisions with neutral particles), E denotes the energy, Q denotes the heat and P denotes the injected power. The angular brackets are used for the averaging over velocity weighted with the distribution function. Notice that the subscript e has been neglected everywhere since we here are talking about the electron transport. Similar equations exists for the ion density and

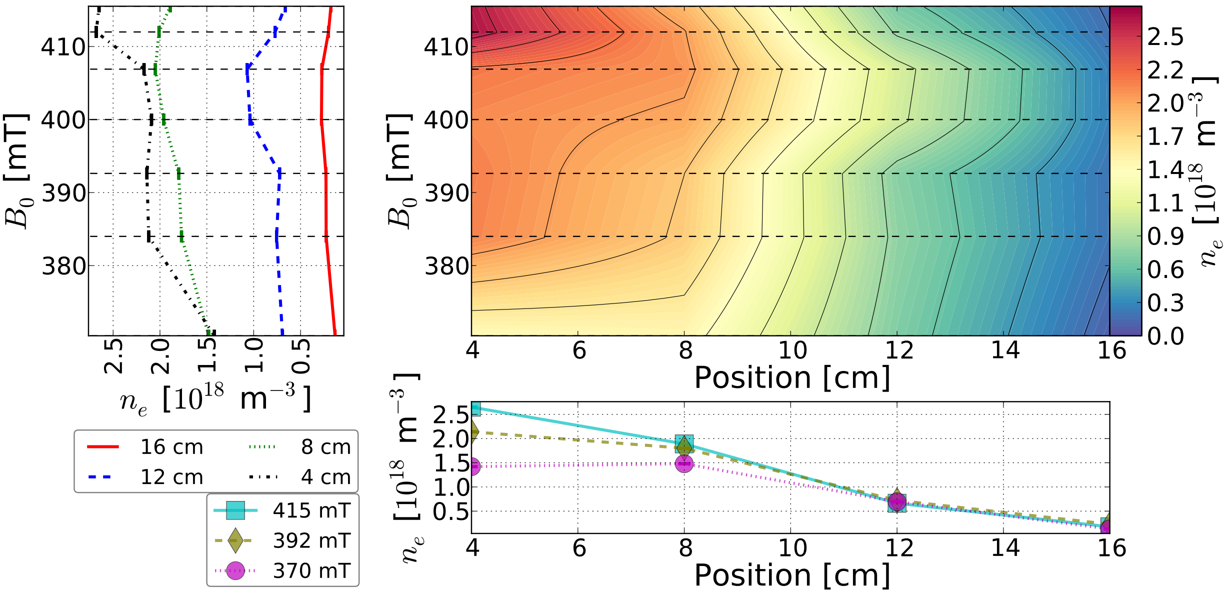

FIGURE 5.8: *Density profiles for argon at various magnetic fields.*

temperature transport as well.

When the injected wave hits the plasma and is absorbed, there is a change in temperature. As a consequence the diffusion $\frac{3}{2n}\nabla \cdot (T\Gamma_n)$ in the temperature transport equation (5.3) increases. The increased diffusion leads to a broadening of the temperature profile. Next, the increased temperature increases the ionization term $n_0 n \langle \sigma v \rangle_{\text{ion}}$ in the density transport equation (5.2), which in turn increases the density in the deposition layer. However, it is found in [37] that the ionization is larger than the diffusion term $\nabla \cdot \Gamma_n$ in (5.3). Hence, the density will build up around the deposition site.

As the temperature profile continues to broaden, there will be more ionization in the density transport equation (5.2), which increases the diffusion term $\nabla \cdot \Gamma_n$. In the end there will be a balance between the diffusion and ionization in the density transport equation (5.2) in the *edge* of the plasma. On the contrary, this will not happen in the center of the plasma, since the ionization term here still exceeds the diffusion of the density. As a consequence there will be a build up of density until an equilibrium (where $\frac{\partial n}{\partial t}$ and $\frac{\partial T}{\partial t}$ is zero) is reached. Hence will we observe the peaked profiles.

It should be mention that it was found in [37], that the collisions with the neutrals and the recombination had negligible effects on the shape of the profiles. So had the ionization and particle flux in the temperature equation.

We can observe that the density profiles for all gases seems to steepen as B_0 is increased. In other words, the shape of the profiles goes from flat to peaked as B_0 is increased, with the steepest density gradient for neon. The increase is less pronounced in argon.

5.1.5 The temperature profiles

The shape of the temperature profiles might be easier to understand as the profile peak for the observed shots tends to follow the deposition of the power better than compared to the density profiles. The reason for this can be explained by fact that the diffusion in the temperature transport in equation (5.3) is much larger than the equivalent in equation (5.2).

Due to the rotational transform and the complex magnetic topology in a stellarator, the flux surfaces will look different at the position where the profiles are acquired (port O6 in figure 3.1) compared to the position where the wave is injected (port T4 in figure 3.1). The flux surfaces at port T4 are given in figure 5.3, whereas the flux surfaces at port O6 are given in figure 5.9.

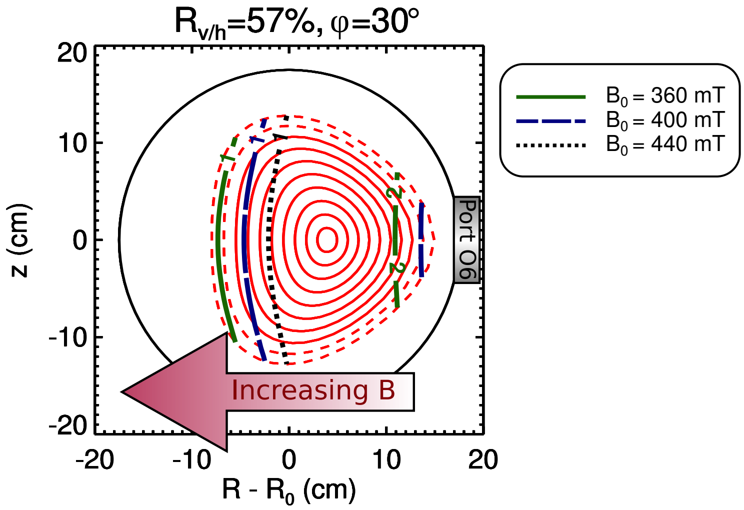

FIGURE 5.9: *The ECR layer over-plotted on the flux surfaces at port O6 for three magnetic fields.*

We will use $z = 0\,\text{cm}$ as our ordinate, as this is the height the probe is injected at. We see in figure 5.9 that the central flux surface is positioned around $R - R_0 = 4\,\text{cm}$. Notice that even at $B_0 = 440\,\text{mT}$, the ECR layer only reaches $R - R_0 = -2\,\text{cm}$, which corresponds to the flux surface located at $R - R_0 = 9\,\text{cm}$. The vessel is located at around $R - R_0 = 17.5\,\text{cm}$.

The figures 5.10, 5.11 and 5.12 are plotted in the same manner as explained in section 5.1.3 We observe that the profiles goes from hollow to flat for all three gases. It is most pronounced in helium, and least pronounced in argon. The change from hollow to flatter profiles could maybe have been explained by moving of the ECR layer, but one can see from figure 5.9 that even for high fields, the ECR layer does not reach deep into the plasma. Yet another suggestion for the flatting of the profiles could have been that heating at the UHR had occurred. However, one can in figure 5.5 observe that the UHR is located far from the center of the plasma, and is therefore not a good candidate of explaining the flattening of the profiles. Therefore, the hollow profiles might be

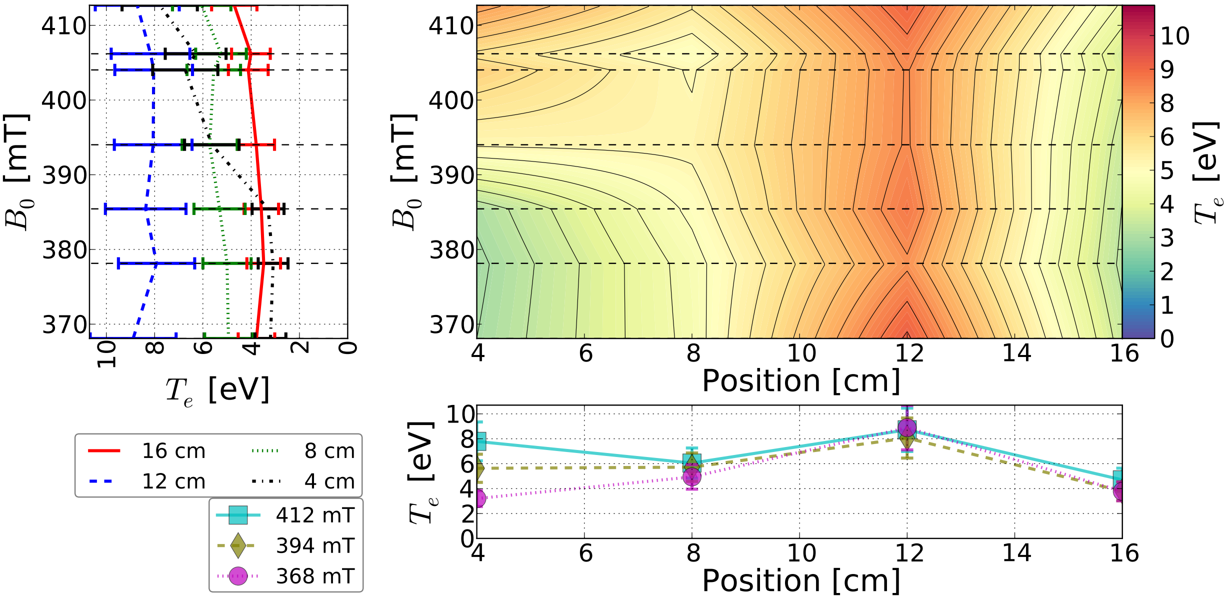

FIGURE 5.10: *Temperature profiles for helium at various magnetic fields.*

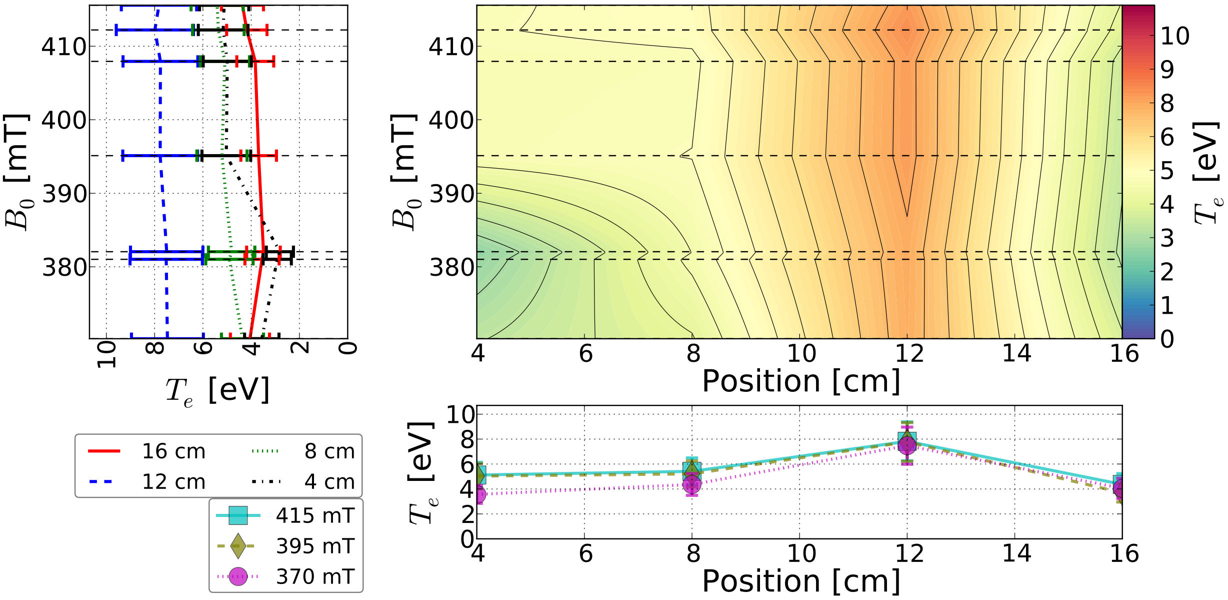

FIGURE 5.11: *Temperature profiles for neon at various magnetic fields.*

explained by the ratio between the diffusion term and ionization term in equation 5.3. Numerical studies, like the one performed in [37] can confirm or disprove this. The gas dependence might be explained by the different ionization energies as shown in table 5.2, since the ionization energies changes the rate coefficient for ionization ($\langle \sigma v \rangle_{\text{ionization}}$) as found in the transport equations (5.2) and (5.3).

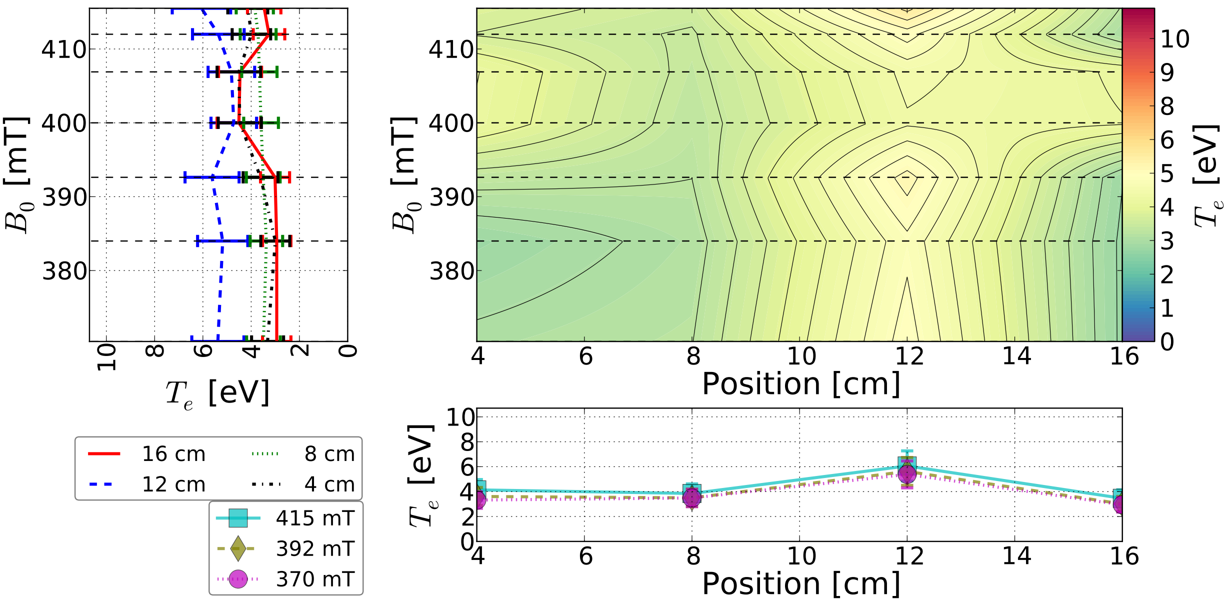

FIGURE 5.12: *Temperature profiles for argon at various magnetic fields.*

5.1.6 Collisionality

Now that the densities and temperatures are known, one can deduce the collisionality. More specifically are we intrested in the electron-ion collision ν_{ei} as given in equation 2.27. Figure 5.13a shows the collisionality for neon at the 14 GHz system. By comparison, figure 5.13b shows the collisionalities for neon in the 8 GHz heating system. In general, we can see that the collisionality is at least one order of magnitude larger in the 14 GHz system compared with the 8 GHz system. This is the case for all the three gases, and is a consequence of the temperature and density obtained in the 8 GHz case (see figure 5.13c), as compared with the 14 GHz case. The collisionality scales with density and temperature as shown in equation (2.29).

At this point it should be noted that the density and temperature for hydrogen were properly measured once during the magnetic field scan. With temperatures ranging from $5 - 25$ eV, and densities below $0.5 \cdot 10^{18}\,\mathrm{m}^{-3}$, substantially lower collisionalities were found.

However, what kind of collisionality regime we are in is not determined by the collisionality alone, as discussed in section 2.2.1. To find the collisional regime, the collisionality must be normalized with the poloidal transit time τ_{tr}. The collisional regime is then determined by the ratio $\frac{\tau_{tr}}{\tau_{ei}}$. The poloidal transit time has been found to be around 12 μs for hydrogen, and close to 20 μs for the other gases. The figures 5.14, 5.15 and 5.16 shows the normalized collisionality profiles. The large error bars in the plots comes as a consequence of the 20% accuracy from the temperature measurements.

It can be observed for that for helium, neon and argon $\frac{\tau_{tr}}{\tau_{ei}} \gg 1$. The hydrogen shot performed showed a normalized collisionality of 8, 0.9, 0.42, and 0.34 at the positions

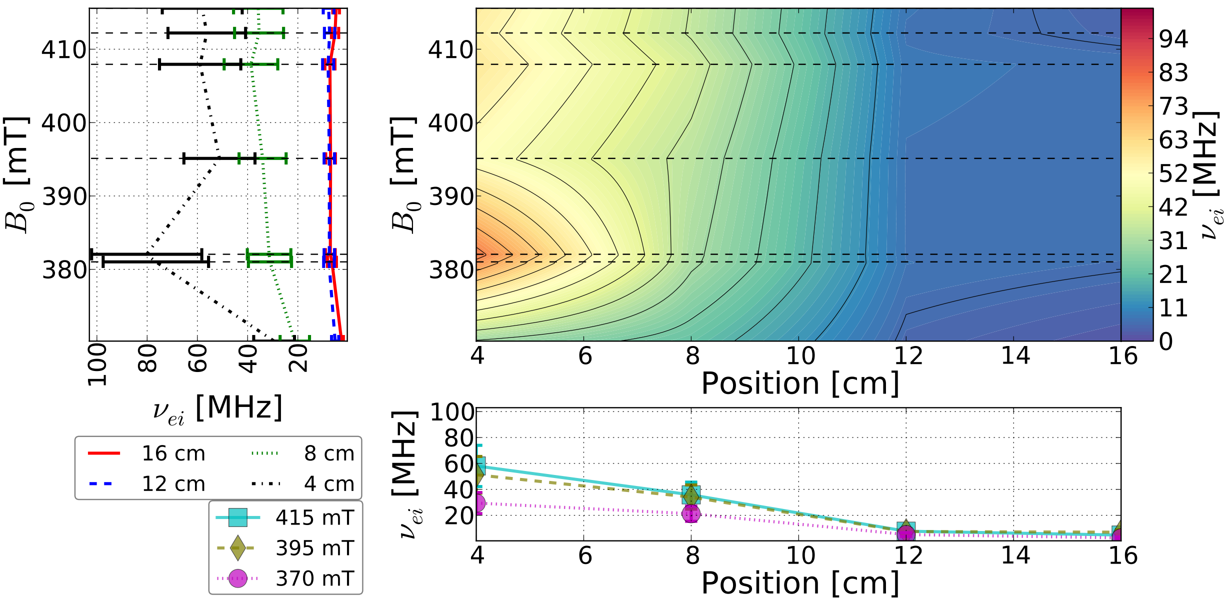

(a) Collisionality profiles for Argon at various magnetic fields.

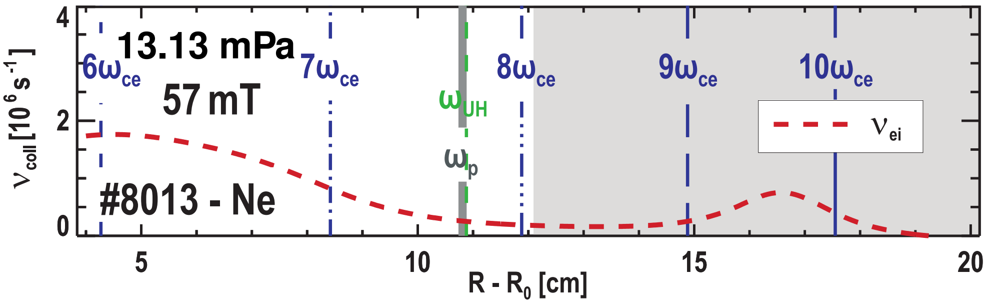

(b) Collisionality in the 8 GHz system [12].

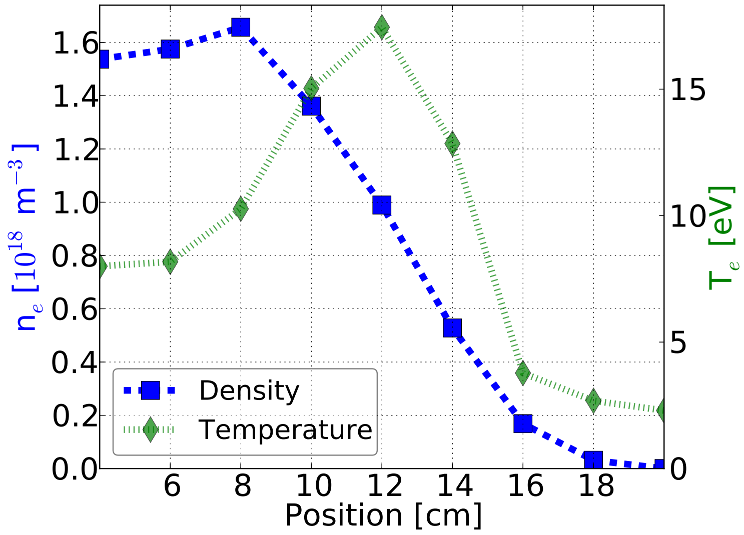

(c) Density and temperature profiles for 8 GHz shot #8013.

FIGURE 5.13: *Comparison of collisionalities in the 8 GHz and 14 GHz system.*

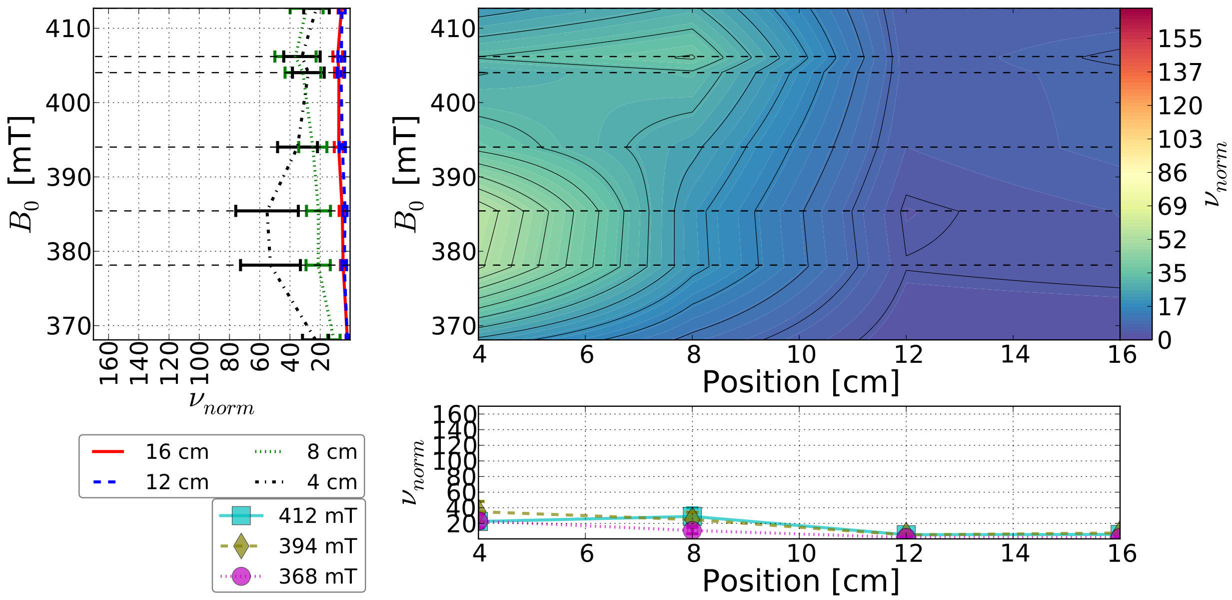

FIGURE 5.14: *Normalized collisionality profiles for helium at various magnetic fields.*

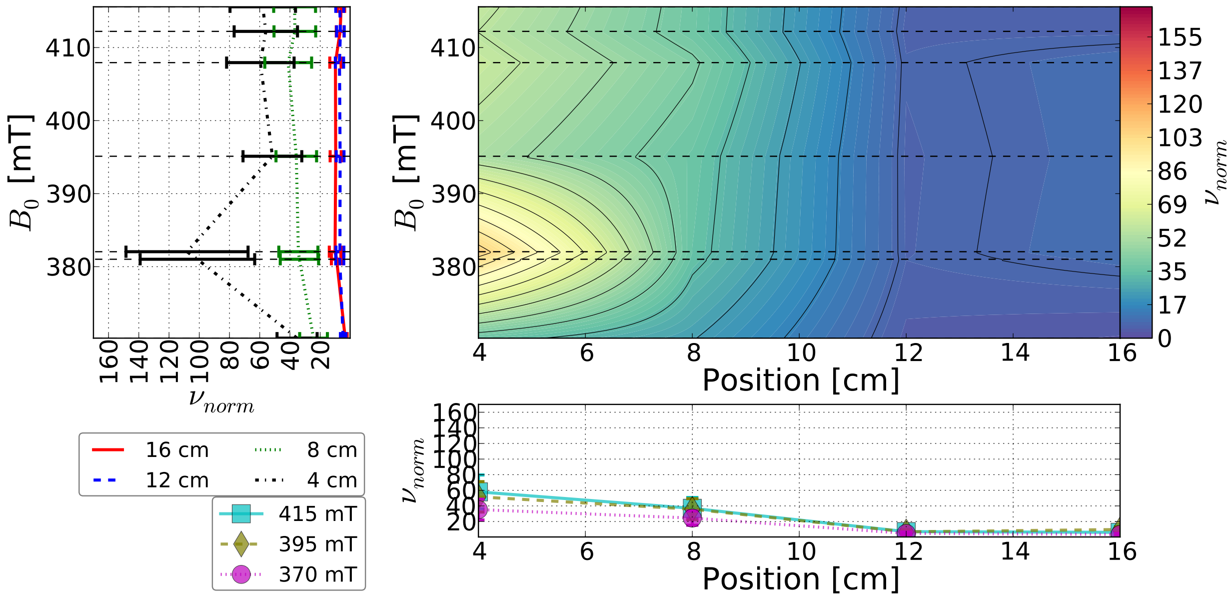

FIGURE 5.15: *Normalized collisionality profiles for neon at various magnetic fields.*

$R - R_0 = 4$ cm, 8 cm, 12 cm and 16 cm. In other words neoclassical effects should be apparent.

With exception from hydrogen, the line averaged, normalized collisionalities $\frac{\tau_{tr}}{\tau_{ei}} \gg 1$, which means that we are in the *high collisional Pfirsch-Schlüter* regime, as apparent from figure 2.2. In the high collisional Pfirsch-Schlüter regime, the diffusion coefficient

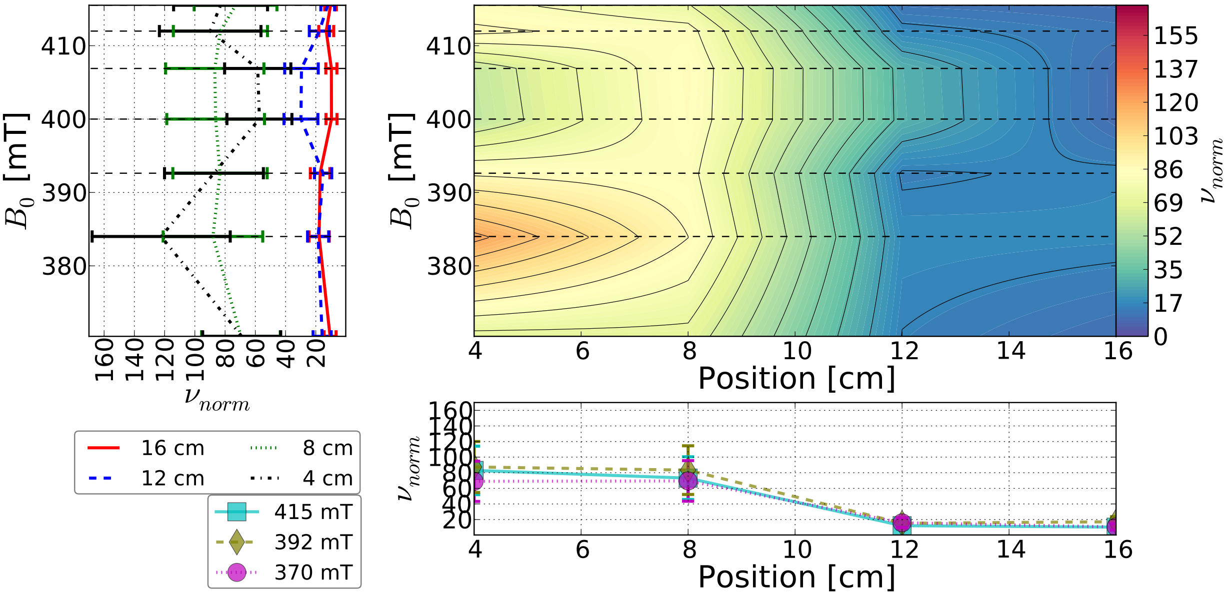

FIGURE 5.16: *Normalized collisionality profiles for argon at various magnetic fields.*

is given by

$$D_{ps} = \frac{m_e v^2 \tau_{ei}}{2qB_\phi R} \tag{5.4}$$

where v is taken to be the thermal velocity of the electrons $v = \sqrt{\frac{2T_e}{m_e}}$ [6].

5.1.7 The diffusion coefficient

As noted in section 5.1.6, it was found from the probe measurement that the electrons in the magnetic field scan performed belongs to the *high collisional Pfirsch-Schlüter* regime, and therefore equation (5.4) can be used to estimate the diffusivity. The line averaged diffusion coefficients obtained from the probe measurement are shown in figure 5.18. We observe in the figure that the diffusion coefficient is relatively constant over most of the B_0 values. Only for very low B_0 we observe an increase. It should be noted that the hydrogen measurement done at 410 mT yields a D_{ps} of about two orders of magnitude larger than in the other gases. *Particle* transport based on this result is presented in A.1.

It should be stressed that the real diffusivity is expected to be much larger since equation (5.4) does not incorporate the effects of turbulent transport. For that reason, estimates of the diffusion coefficient based on the particle confinement time (as described in section 2.2.2) were done towards the end of this thesis. The measurements were done for argon at various magnetic fields. For each shot, the input power was modulated with square waves at a frequency of 77.7 Hz[3] over a time of 0.5 s. The pulses

---

[3] It should be noted that for some of the higher magnetic fields, the measured density was only close

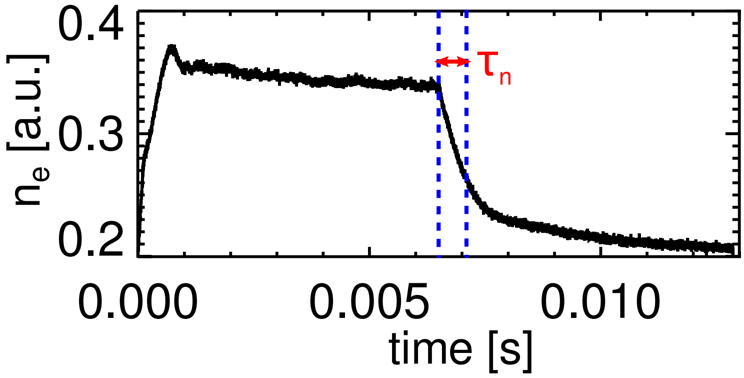

FIGURE 5.17: *Estimation of the particle confinement time. Shown is the averaged pulse from the interferometer from the modulation measurement for shot* #9786*.*

in the interferometer signal were averaged to one averaged pulse, and the particle confinement time was found from this averaged pulse. One of those averaged pulses is shown in figure 5.17.

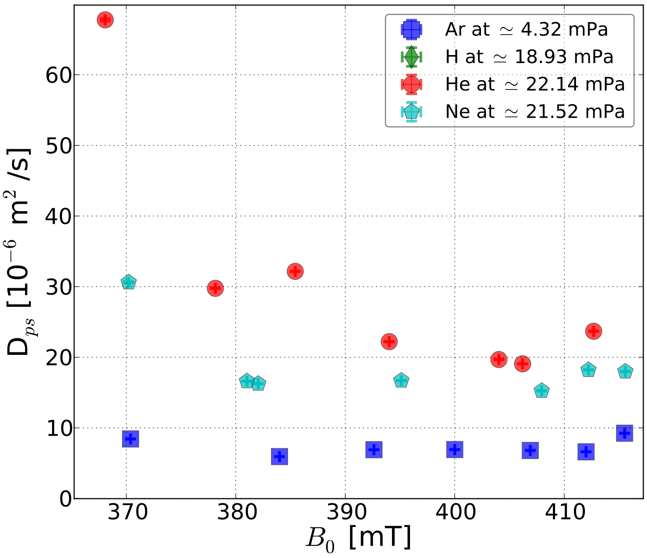

FIGURE 5.18: *Diffusion coefficients as a function of* B_0*.*

The diffusion coefficient obtained from the interferometer signal was found to be larger by approximately six orders of magnitude. This is expected to be closer to the real diffusivity, as this calculation is not neglecting the effects of turbulent transport.

---

to reach the saturation point, but did not reach it completely. In further studies one should therefore use a lower modulation frequency.

We can therefore conclude that turbulent transport is probably the dominant transport mechanism in this regime.

It can also be mentioned that attempts to measure the *energy* transport by measuring the signal decay from the optical diode[4] were done. However the noise in the signal was too high to say anything conclusive. A filtering of the high frequency Fourier components of the signals could reduce the noise, so that one could draw conclusions of the filtered signal.

5.1.8 Radiation

The radiation losses are shown in figure 5.19, and are obtained through the calculation given in section 2.3. We notice how the radiated power seem to saturate at high magnetic fields for helium and neon, whereas it continues to increase for argon. The radiation profiles are shown in A.2.

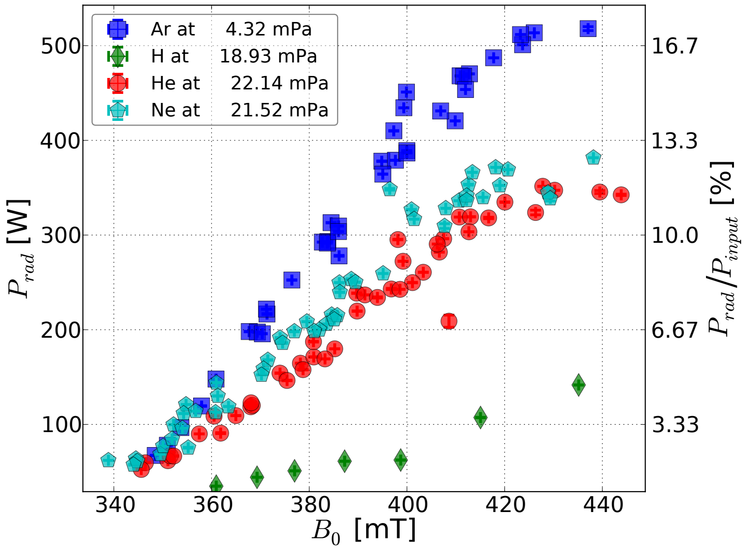

FIGURE 5.19: *Radiation losses as a function of the magnetic field.*

5.1.9 Degree of ionization

The degree if ionization, α_{ion}, is further characterization of the plasma. It is defined by

$$\alpha_{ion} \overset{def}{=} \frac{n_i}{n_i + n_g}, \tag{5.5}$$

and can be estimated if we do the following assumptions:

---

[4] One could have used the bolometer for this purpose, but it has a too low time resolution due to the thermal conduction as described in section 4.3.

- Quasi neutrality and singly ionized particles, which leads to $n_i \simeq n_e$.
- The gas before ionization is behaving like an ideal gas, so $n = \frac{p}{T}$.
- The neutral gas is assumed to be in the room temperature, so $T \approx 293\,\mathrm{K}$.

By acquiring pressure *before* the plasma is turned on, we find the particle density by $n_{\mathrm{off}} = p_{\mathrm{off}}/T_{\mathrm{room}}$. This means that the neutral gas pressure at any instance is $n_g = n_{\mathrm{off}} - n_i$, so

$$\alpha_{ion} = \frac{n_e}{n_{\mathrm{off}}}. \tag{5.6}$$

The result from these calculations are plotted in figure 5.20. One can observe that the ionization degree in argon is much higher than for the other gases. This is a direct consequence of the low ionization degree seen in table 5.2, together with its low base pressure.

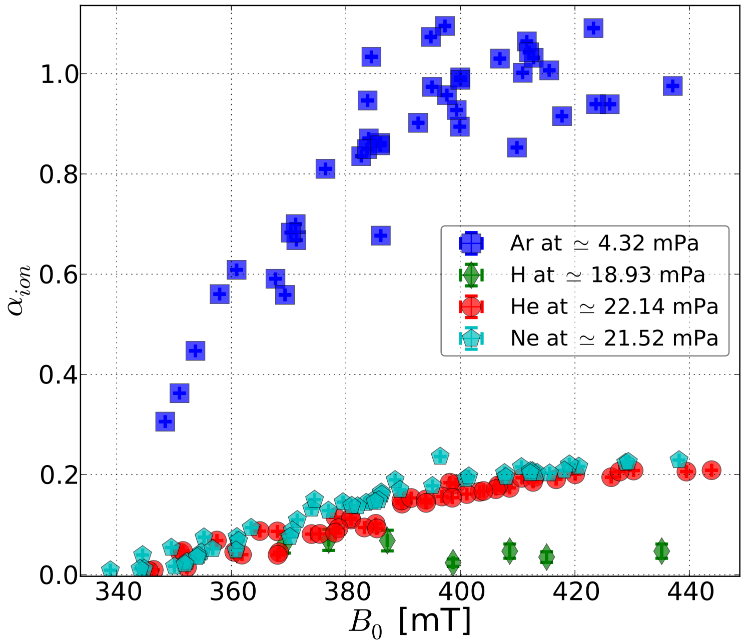

FIGURE 5.20: *The ionization α_{ion} as a function of the magnetic field.*

For very high magnetic fields we see that we have an ionization degree above one. This is of course physically impossible, thus are the assumptions too crude. Firstly, one could have used the density of the neutral particles n_0 during the shot instead of n_{off}, since the neutral gas temperature is increasing during a shot [31]. However, the neutral gas pressure during a shot is expected to increase by the equal amount of temperature due to the ideal gas law. Hence, it is expected that $n_{\mathrm{off}} \simeq n_0$. Further on, by looking at table 5.2, we see that it is plausible that there can be second degree ionizations in the argon plasmas. This can easily yield ionization degrees above one with our assumptions.

Consequences of secondly ionized particles

If there are higher ionized states present in argon, it will slightly alter the measured densities. This is because the equation to obtain the electron density from the ion saturation current makes the assumption of singly ionized particles. Therefore, the estimated density in the case of argon might be an over/estimation.

Secondly, it was thought that it could be possible to increase the temperature at higher magnetic fields in argon since there is a certain difference in the energy needed for the first and the second ionization. The idea is that the energy lost by an electron is higher in an ionization process in other inelastic collision processes. Therefore, if almost all the atoms are firstly ionized, the electrons can accumulate more energy before an ionizing collision occurs as compared with the oppsite situation.

One can observe on figure 5.4 that the saturation for argon starts at lower magnetic field than for the other gases. Although it is not clear, it might look like the saturation is starting around 390 mT. At the same magnetic field the degree of ionization is around 1. This means that it is still possible to inject more energy in the plasma by moving the ECR layer towards the center. From this one could expect that the electron temperature could have been increased considerably by increasing the magnetic field.

In figure 5.12 we can observe that the line averaged temperature is increasing after 390 mT. In addition, the radiation losses for argon (seen in figure 5.19) seems to increase after 400 mT, whereas it is saturating for neon and helium. This indicates that the energy absorbed in the plasma at these fields were directed to a temperature increase rather than to ionize the particles as expected. However, one would also assume that the confined energy would rise, and that this would be apparent in figure 5.2. Instead, one can observe that the confined energy seems to flatten at around 400 mT.

In the end, the temperature increase is not so high as expected. If one compare the temperature profiles of argon with the ones for helium, one can see that the line averaged temperature gradient with respect to the magnetic field is comparable at high B_0. In addition T_e for argon is lower than $E_{\text{first ionization}}$, so we have no guarantee that all the particles are firstly ionized. In fact, there might be a mixture if firstly and secondly ionized ions in the plasma at the same time.

5.2 Variation of the base pressure

Just as the results from the magnetic field scan were presented in the previous section, the results from the pressure scan are presented here. In the pressure scan the *base* pressure (the pressure in the vessel before the plasma is turned on) is varied on a shot to shot basis.

In terms of lowering the collisionality, lowering the pressure is the best candidate as the temperatures tends to rise, and the electron density tends to decrease. This can be

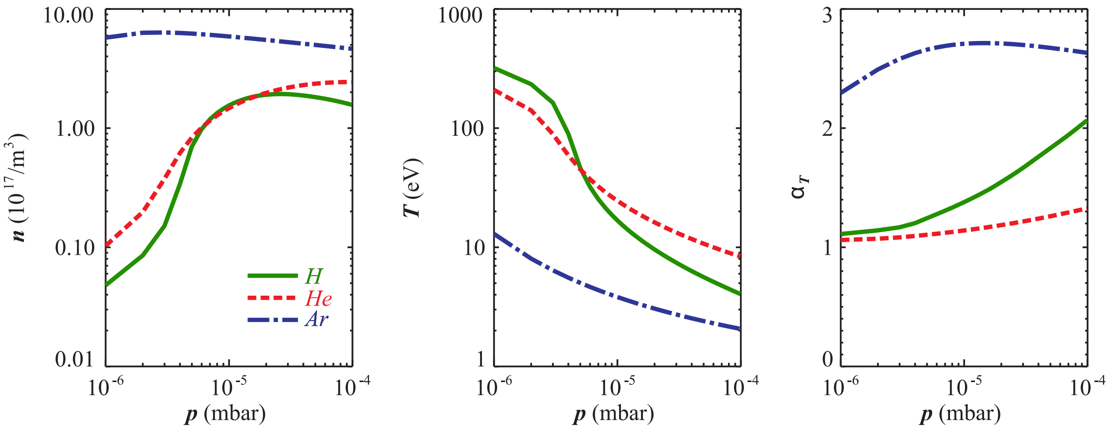

(a) Plots from pressure variation.

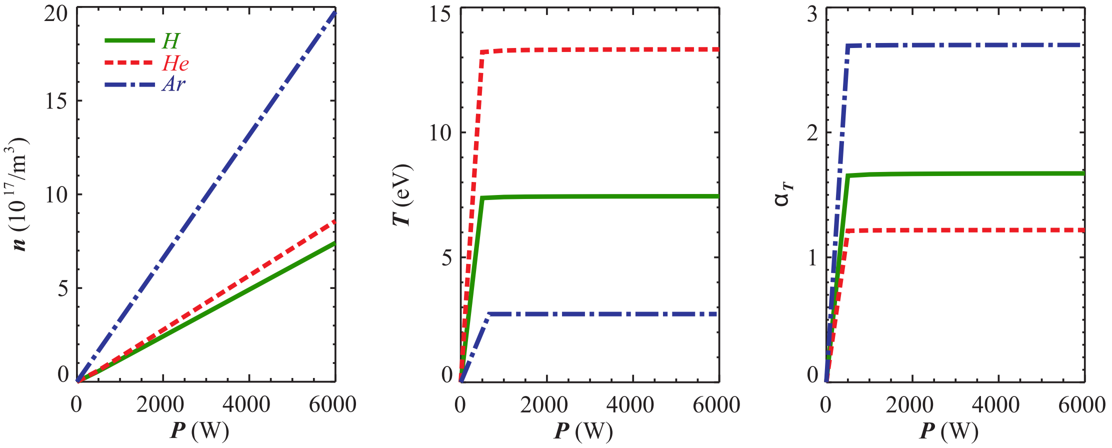

(b) Plots form injected power variation.

FIGURE 5.21: *Variation of central density, central temperature and temperature profile factor as a function of pressure and injected power [37].*

seen in figure 5.21a, where the temperature profile factor α_T is defined as

$$\alpha_T = \frac{T(r = r(\text{heating peak}))}{T(r = 0\,\text{cm})}. \tag{5.7}$$

That means that we will have peaked profiles whenever $\alpha_T < 1$, flat profiles for $\alpha_T = 1$ and hollow profiles for $\alpha_T > 1$. Also, it should be pointed out that increasing the injected power is not a good candidate for decreasing the collisionality as it turns out that after a certain point, the power is directed to ionization processes rather than heating processes, which can be seen in figure 5.21b.

It should be pointed out, though, that the results presented in figure 5.22 are obtained from a numerical simulations where B_0 was lower than in the 14 GHz system. This will change the position of the ECR-layer as presented in 5.1.1. Nevertheless, the trends found in figure 5.22 are not expected to change much.

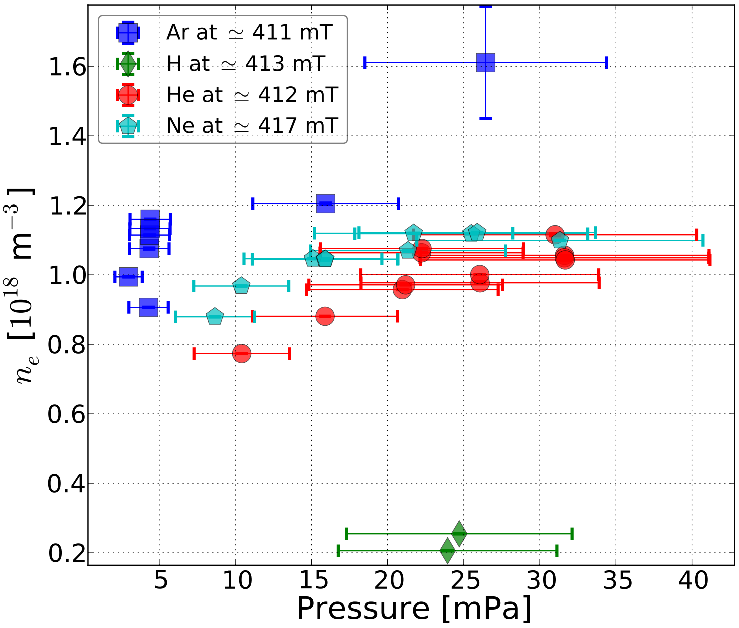

FIGURE 5.22: *Densities in the pressure scan. The large error-bars are due to the* ±30% *in the pressure measuring device.*

By stating this, it is clear from figure 5.21a that we would like to operate at pressures below 10 mPa. The problem is however, that the plasma becomes more and more unstable for decreasing electron densities, and that injection of probes at these low electron densities makes the plasma globally unstable (in other words, the signal from the interferometer is no longer flat as it is in figure 5.1). Because of this, we are more bound to operate at the flatter regions (where the non-logarithmic gradients are low) in figure 5.21a. As expected the measured density is increasing for increasing pressure as seen from figure 5.22. It should also be stated that small amount of ionizing radiation was found at very low pressures, but that the amount was still far below the safety limits.

5.2.1 The density profiles

The acquisition method and an explanation on how to read the plots is found in section 5.1.3. Figure 5.23, 5.24 and 5.25 shows the density profiles for the pressure scan. We observe that at high pressures for argon, the highest density in this thesis was obtained. Helium and neon shows little dependence on the base pressure variation in the range it was varied here. It might be the case that argon is almost constant for most of the base pressures in figure 5.25, and that the density increases towards the very end of the pressure scan. This, however, is hard to tell due to the lack of resolution in the base pressure.

Also in the pressure scan one hydrogen shot was successfully measured. The other

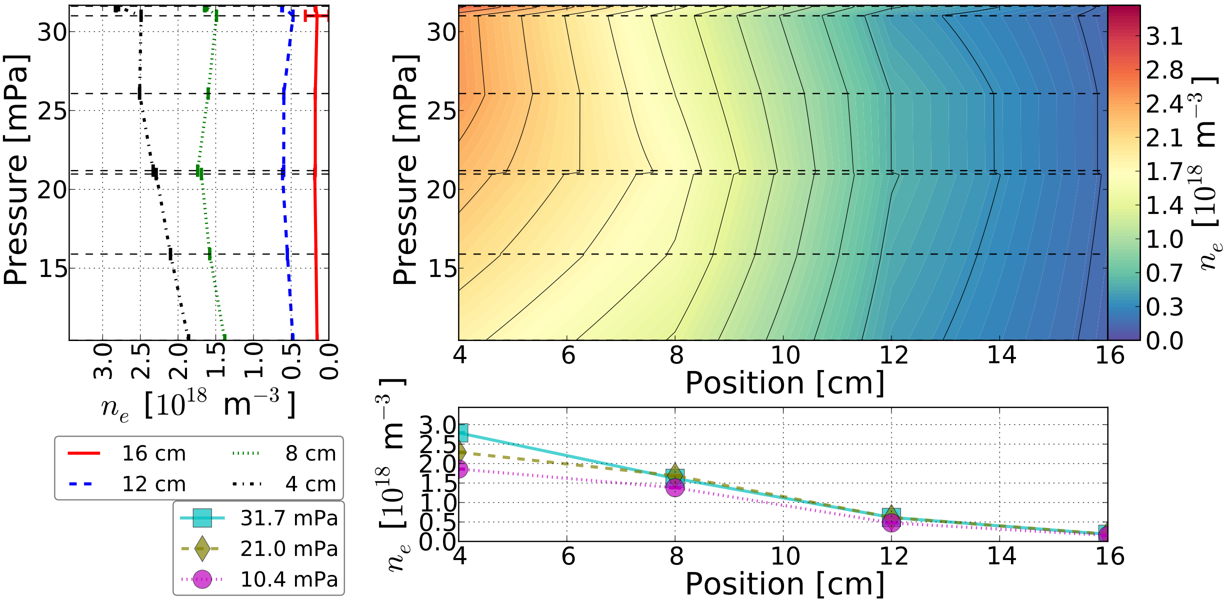

FIGURE 5.23: *Density profiles for helium at and various pressures.*

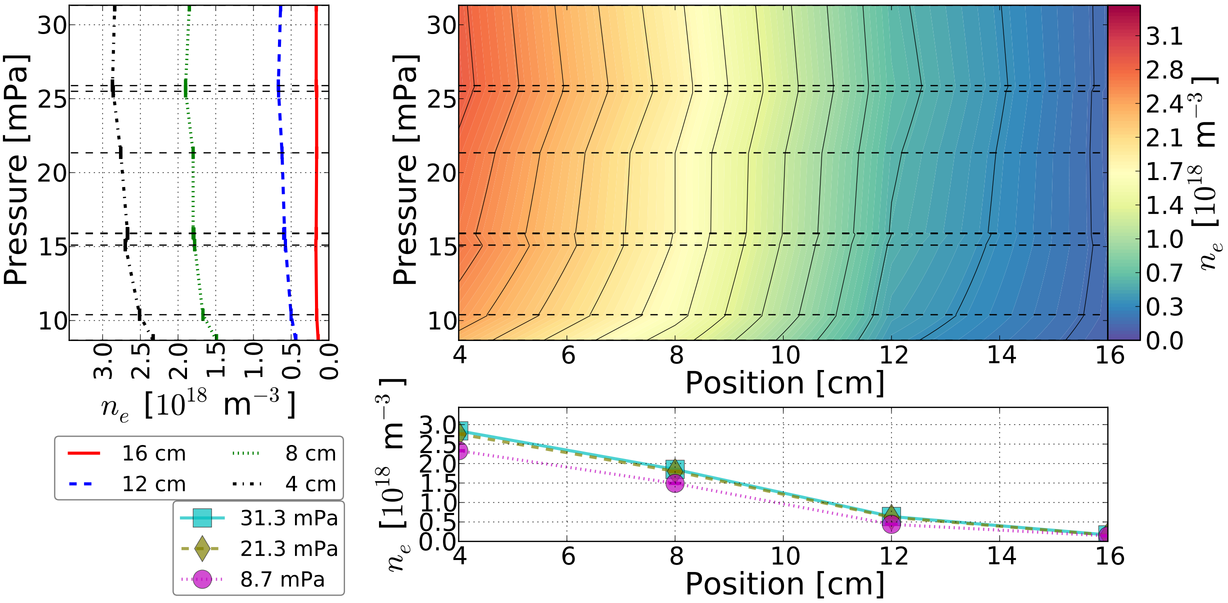

FIGURE 5.24: *Density profiles for neon at and various pressures.*

shots were either out of the sorting range, or showed a non-stable interferometer signal. The shot was performed at approximately 24 mPa, and yielded a line averaged density on approximately $0.3 \cdot 10^{18}\,\mathrm{m}^{-3}$.

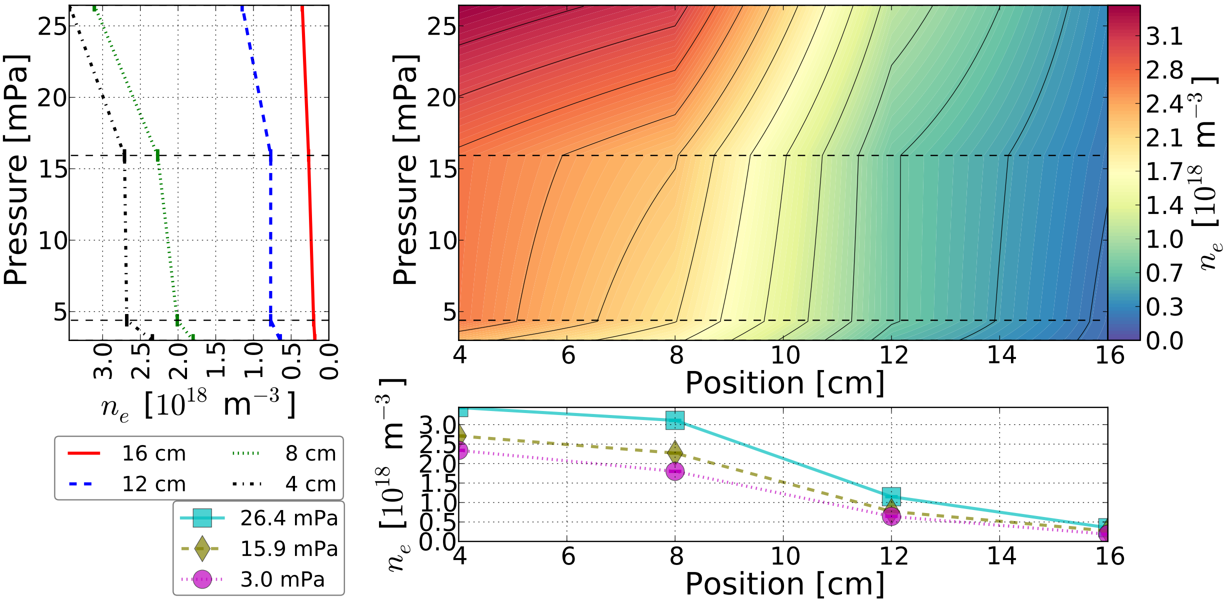

FIGURE 5.25: *Density profiles for argon at various pressures.*

5.2.2 The temperature profiles

Figure 5.26, 5.27 and 5.28 shows the temperature profiles of the pressure scan.

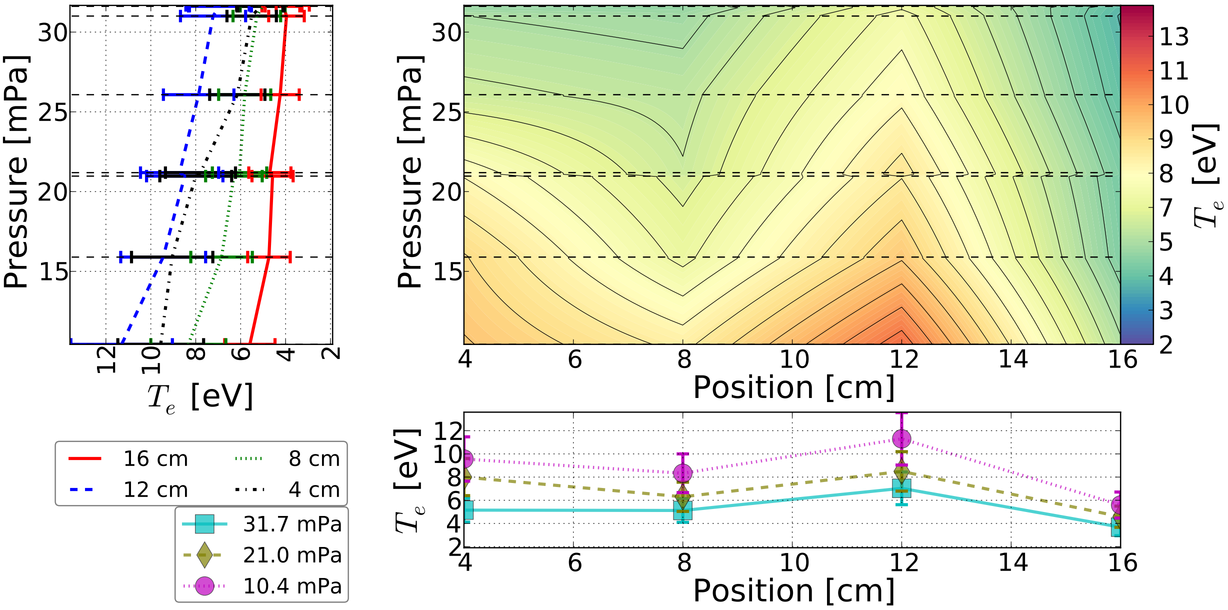

FIGURE 5.26: *Temperature profiles for helium at and various pressures.*

We observe that the profiles are hollow at high pressures, and flat at low pressures. There is also a general increase in temperature at lower pressures. This is what is

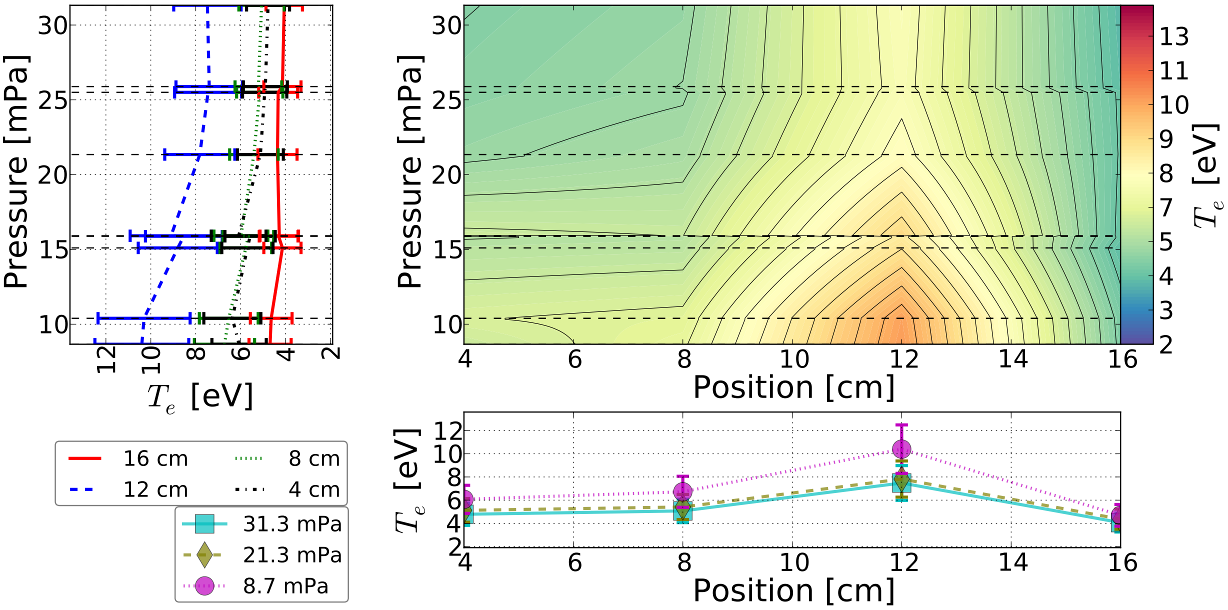

FIGURE 5.27: *Temperature profiles for neon at and various pressures.*

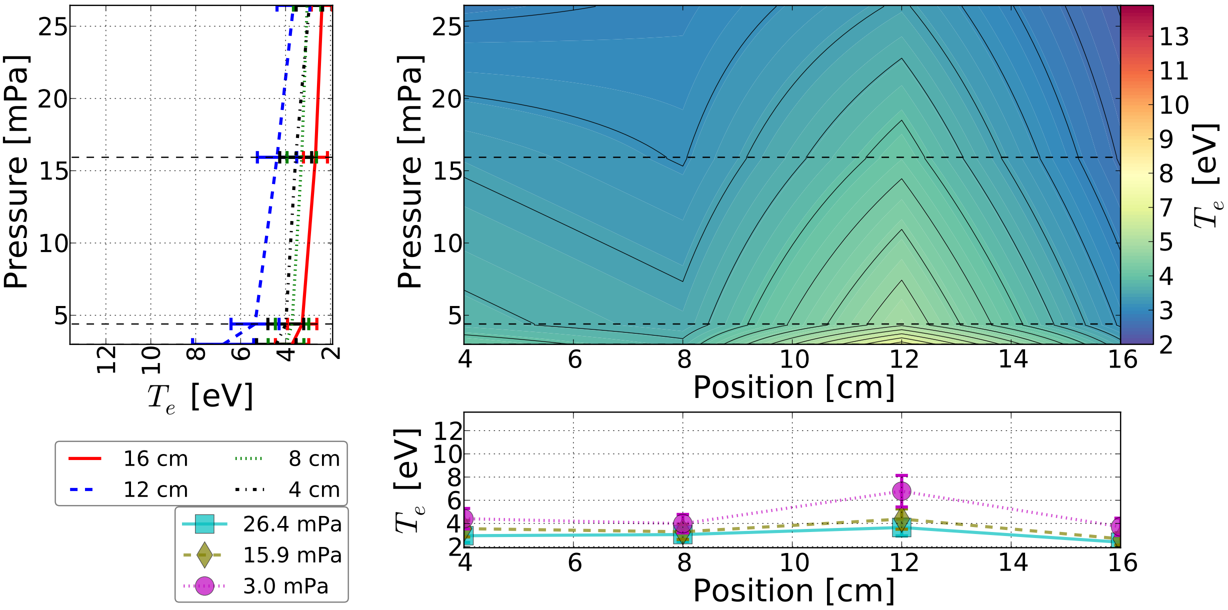

FIGURE 5.28: *Temperature profiles for argon at various pressures.*

expected from what was discussed in section 5.2. The explanation for this is that at lower pressures, there is less particles to ionize, and the mean free path becomes longer. Hence, the energy is directed to an increase in temperature. As expected, hydrogen had the highest line averaged temperature of $\approx 18\,\text{eV}$.

It should be noted that the ECR layer stays at the same position when varying the pressure since the magnetic field is kept constant. As the density is not varying too much, the flattening of the temperature profiles is not likely to be due to movements of the resonance layers.

5.2.3 Normalized collisionality

As seen in the two previous section, lower densities and higher temperatures have been observed at lower pressures as compared with the magnetic field scan. Figure 5.29, 5.30 and 5.31 shows the collisionality as a function of the pressure. We can observe that although we in general have lower collisionalities as compared with the collisionalities found in section 5.1.6, the line averaged collisionality normalized with the poloidal transit time is still orders of magnitude larger than one. Interestingly, hydrogen showed lower collisionalities. At position $R - R_0 = 4, 8, 12$ and 16 cm the collisionalities were $16, 0.4, 0.3$ and 0.1. That means that the line averaged collisionality was still above one. Nevertheless, neoclassical effects should be apparent within these parameters. It is therefore suggested that hydrogen at low pressures is a prominent candidate for studying neoclassical effects. Although difficult, probe measurements are possible at these lower pressures.

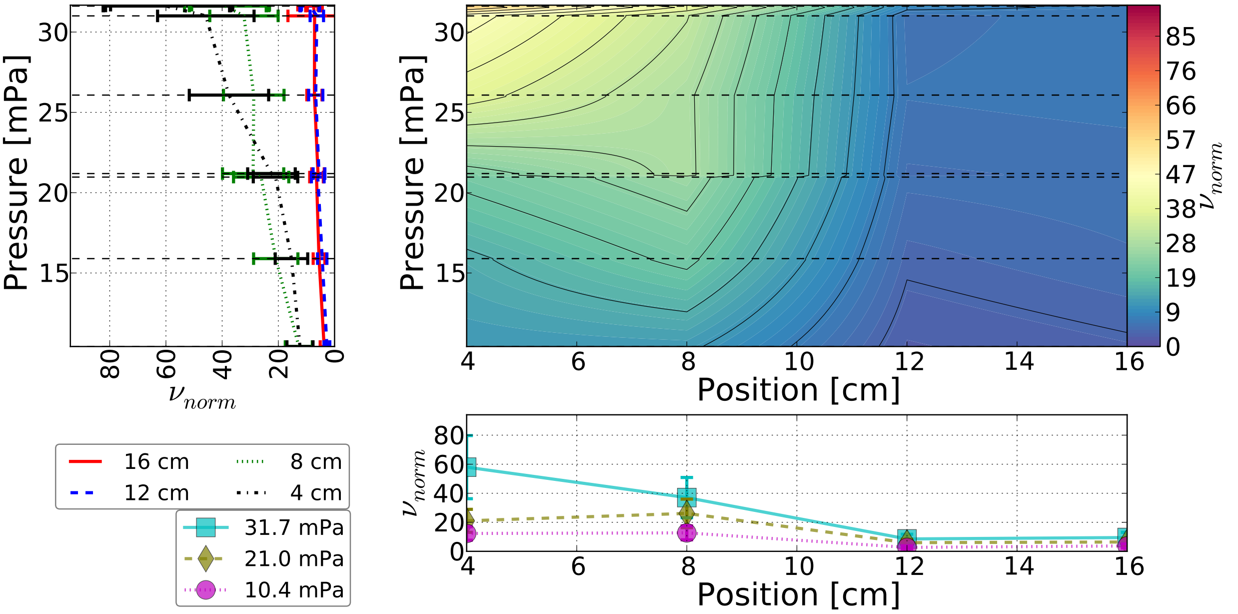

FIGURE 5.29: *Normalized collisionality for helium at various pressures.*

5.2.4 The diffusion coefficient

As discussed in 5.2.3, the line averaged τ_{ei} is $\ll \tau_{tr}$, except for hydrogen. That means that we are still in the *high collisional Pfirsch-Schlüter* regime. The dependency of D

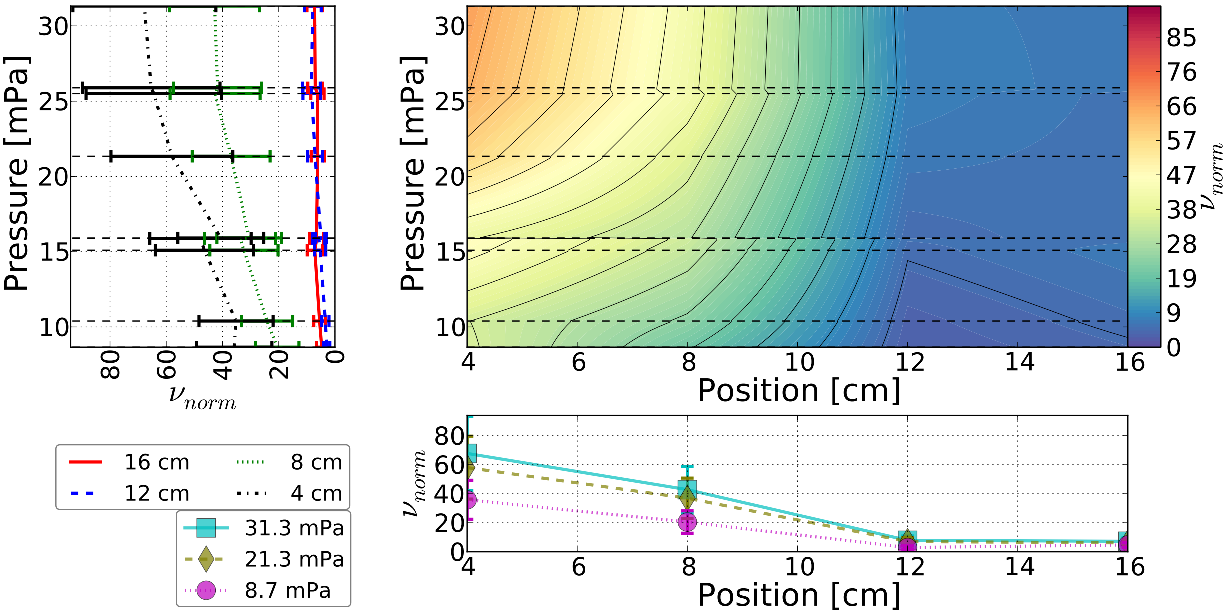

FIGURE 5.30: *Normalized collisionality for neon at various pressures.*

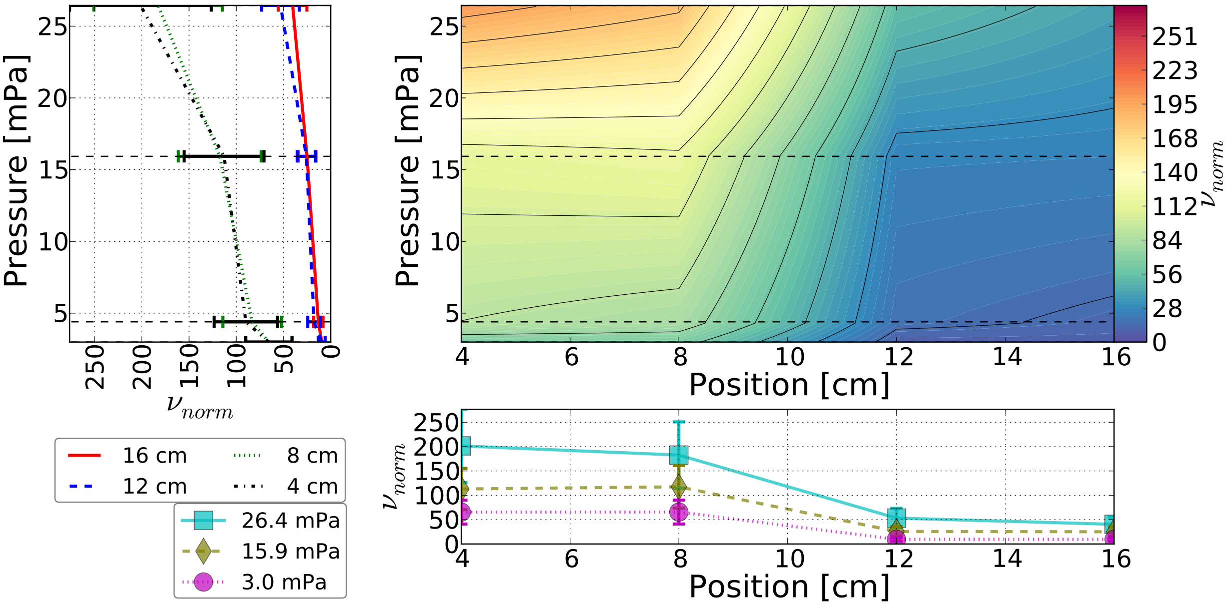

FIGURE 5.31: *Normalized collisionality for neon at various pressures. Be aware of the range of the z-axis.*

as a function of the pressure is given in figure 5.32 We can clearly see a non-linear monotonic decrease in D as we increase the pressure. Since D is estimated from the probe measurements of the density and the temperature, the decrease in D is directly related to how these quantities are varying with pressure. The dependence can be seen

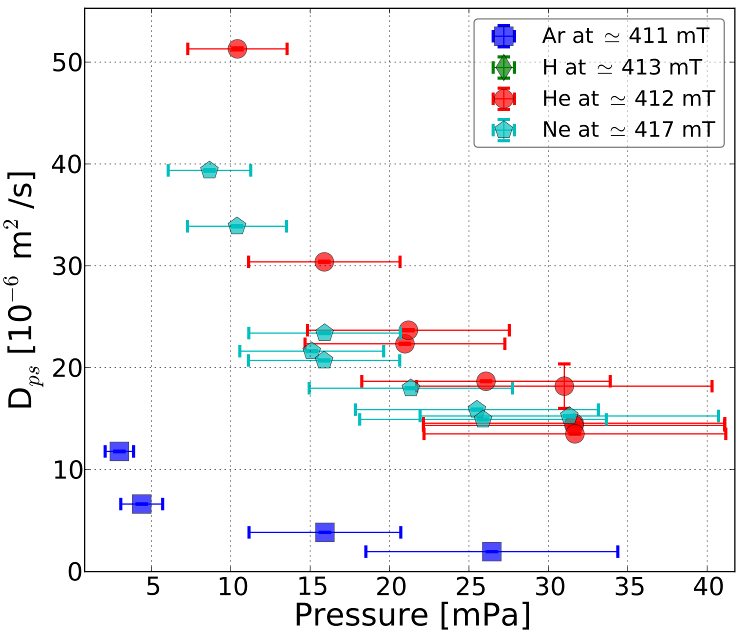

FIGURE 5.32: *The diffusion coefficient as a function of pressure.*

in equation (5.4) and (2.27).

Note that the large error-bars in the $y-$direction is due to comes from the accuracy of ±30% in the pressure measuring device [38].

5.2.5 Radiation

It is also of interest to investigate how the radiation losses are related to the pressure. As it is seen in figure 5.33, it is hard to give a general trend for all three gases. In helium, we observe an increase for higher pressures. The pressure dependence for neon appears constant. For argon, we see that we have high radiation at very low pressures. This may be because of the high electron temperatures at this pressure as compared with measurements at other pressures. One should however perform more shots at various fields in order to be able to deduce a trend for argon. In the end, the trends observed is a consequence of how the temperature and density changes with pressure (as seen in figure 5.21a) together with what transitional states that are present in the plasma.

5.2.6 Confined energy

From figure 5.21, we can see that if we decrease the pressure for helium within the range considered, we will obtain higher temperatures and lower densities. As the change in temperature is higher than the change in density, this will yield a higher confined energy for lower pressures. This is indeed what is being observed in figure 5.34. For argon we see that both the temperature and the density is increasing slightly for lower pressures.

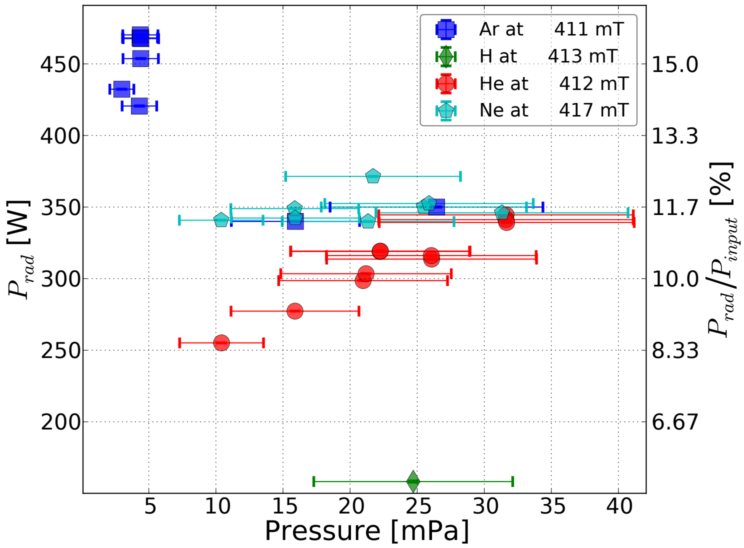

FIGURE 5.33: *Radiation losses when varying the pressure.*

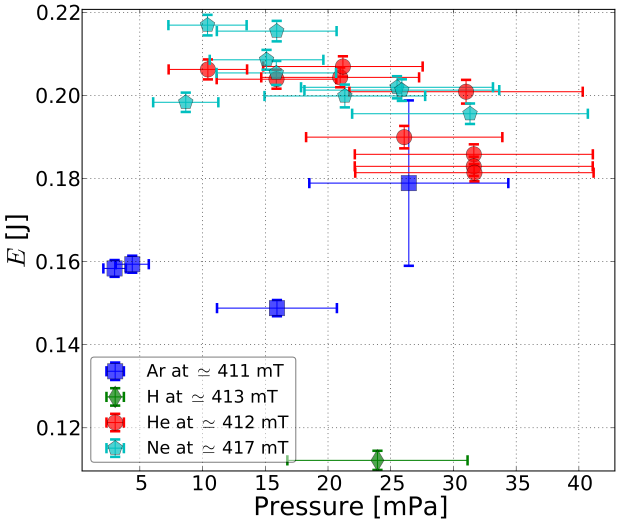

FIGURE 5.34: *The confined energy at various base pressures.*

The change is lower than those found in helium. Hence will a higher confined energy be expected at lower pressures, but with a more shallow slope than what is found for helium. This is not apparent in figure 5.34. At approximately 22 mPa the confined energy is unexpectedly high. Nevertheless, looking apart from the unexpected result, it is plausible that a trend described above could be observed if one had more argon measurements.

Although we remember that we made a rather crude assumption on the ion temperature (see 5.1), we see that the highest confined energy is ≈ 0.21 J. This is approximately the same found for the 8 GHz regime as found in TJ-K [39].

5.2.7 Ionization

The ionization as a function of the base pressure is presented in figure 5.35. We see that there is a non-linear monotonic decrease of the ionization as the pressure is increased, and that the rate of change of α_{ion} is decreasing for increasing pressure. This can be explained with the fact that the temperatures are lower at these higher pressures, meaning that less particles have the energy required for ionization. We also see that the degree of ionization is as large as 1.4 for argon. This is of course unphysical as α_{ion} is bound to be between 0 and 1. As discussed in section 5.1.9, this is most probably due to secondly ionized particles. This means that argon at low pressures is interesting to study highly ionized plasmas.

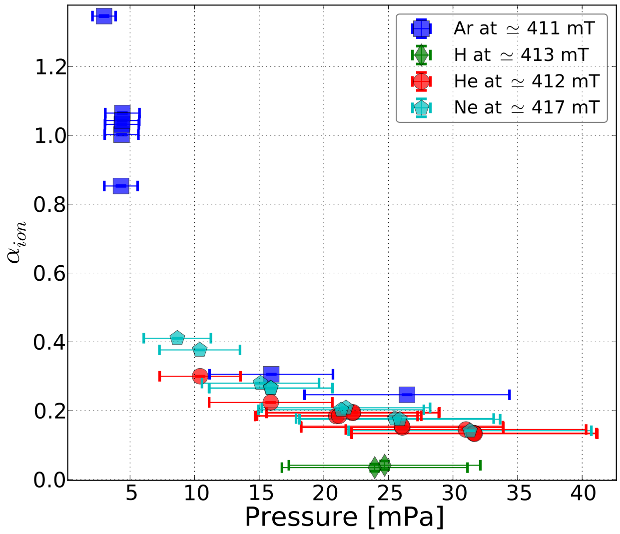

FIGURE 5.35: *The ionization as a function of the pressure.*

Chapter 6

Summary and outlook

6.1 Summary

To conclude the work of this thesis, characterization of the equilibrium state in the plasmas generated with the new 14 GHz has been done. Two scan types were performed: One magnetic field scan (where B_0 was increased on a shot to shot basis) and one base pressure scan (where the base pressure was increased on a shot to shot basis).

It has been shown how the density, temperature, collisionality, diffusion coefficient and the radiation varies as the magnetic field and base pressure is varied. We have seen how the positioning of the ECR layer has affected the measured quantities as the magnetic field has been varied, and that we have closed in on lower collisional regimes as the pressure has been reduced.

For the magnetic field scan we have seen that when we increased B_0, the density increased and saturated, and the profiles got increasingly peaked. In addition, the temperature increased and the profiles were changing from hollow to flat. As a consequence the confined energy increased. It was found that the collisionality had a "bump" at the inner position at low fields when increasing B_0, and that it was relatively flat apart from that. From this we found that helium, neon and argon belongs to the the high collisional Pfirsch-Schlüter regime, whereas hydrogen was situated at the boarder between the low collisional Pfirsch-Schlüter regime and the plateau regime. For helium, neon and argon the diffusion coefficient decreased at first, and remained relatively constant after that. We have also seen that the degree of ionization and the radiation losses increased for higher fields. In addition, the diffusion coefficients obtained from measuring the energy confinement time was found to be six times larger than the diffusion coefficient obtained from the probe measurements. Therefore, turbulent transport is believed to be dominant.

From the base pressure scan we have seen that when we increased the base pressure, the density kept quite constant for helium and neon, and is increased a bit for argon. Peaked profiles was observed. We saw that the temperature decreased, and the profiles changed from flat to hollow. We saw that the collisionality was decreasing for low pressures. Helium, neon and argon was found to belong in the high collisional Pfirsch-Schlüter regime, and hydrogen was found to belong to the boarder between the low collisional Pfirsch-Schlüter regime and the plateau regime. We found that the diffusion coefficient was decreasing for increasing pressure for helium, neon and argon. The confined energy decreased for helium and neon for higher pressure. The confined energy for argon might have decreased as well, but more shots have to be made in order to say anything conclusive. The radiation losses was increasing for helium, and might have been unchanged for neon. High radiations were found at low pressures for argon. In general, it was found that the ionization decreased for increasing pressure, and that very high radiations were found for argon at low base pressures.

6.2 Outlook

For further works, one should try to characterize the hydrogen plasmas created by the 14 GHz system fully. One should try to find out why the density in the hydrogen shots does not follow the trend as the other gases do when the magnetic field is increased.

The ion temperatures should also be measured. Once measured, one can more precisely estimate the confined energy. In addition, it would be possible to find what collisional regime the ions are in, as this might be different than the electron regime. The ion temperature can be measured by measuring the the diamagnetic drift and by using LIF measurements in the case of argon.

A spectrometer should be installed to be able to distinguish what kind of atomic states are present in the plasma. With this it will also be possible to see how much of the argon atoms which are secondly ionized (if any). Also, it might be possible to see if molecular phenomenon in hydrogen is causing the scatter in plot of line averaged density. Finally it would be interesting to see how the atomic transitions are changing as the mean free path is changing when moving the ECR-layer.

Further studies on the particle confinement time should also be done for the different gases at different magnetic fields and at different pressures. The energy confinement time would also be possible to measure once an appropriate filtering routine for filtering the noise from the time signal of the optical diode has been made.

Since the measurements at the various plasma parameters are reproducible (except for the case of hydrogen), scans with the 2-D probe diagnostic can be performed on a shot to shot basis to yield 2-D poloidal profiles with high spatial resolution.

As the plasmas in this new regime now have been characterized to a high degree, one can continue with dynamic measurements. Measurements of the 2-D poloidal profiles with high time resolution can be done with SPIDER (Stuttgart's Poloidal array for Investigations of Dynamics in Electron-cyclotron-Resonance-heated plasmas). Also, coils can be used to estimate the plasma currents. A diamagnetic loop can be used to estimate the diamagnetic currents, a saddle coil can be used to measure the Pfirsch-Schlüter currents and the toroidal currents can be measured with a Rogowski coil.

Appendix A

A.1 Transport in the equilibrium

Since the profiles for density and temperature are known together with the diffusion coefficients now are known, the equilibrium transport can be estimated from

$$\Gamma_e = -D\nabla n_e. \tag{A.1}$$

The results presented here is based on the diffusion coefficients obtained from the probe measurements and equation 5.4.

A.1.1 Magnetic field scan

The results from the magnetic field scan are plotted in the figures A.1, A.2 and A.3.

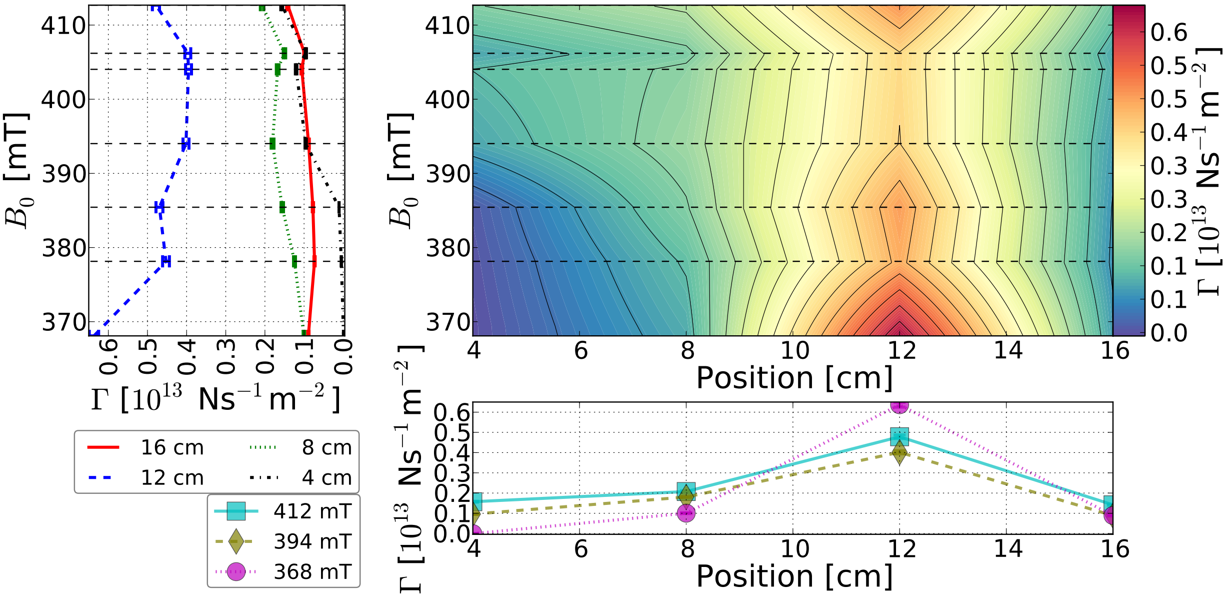

FIGURE A.1: *Equilibrium transport for helium as the magnetic field is varied.*

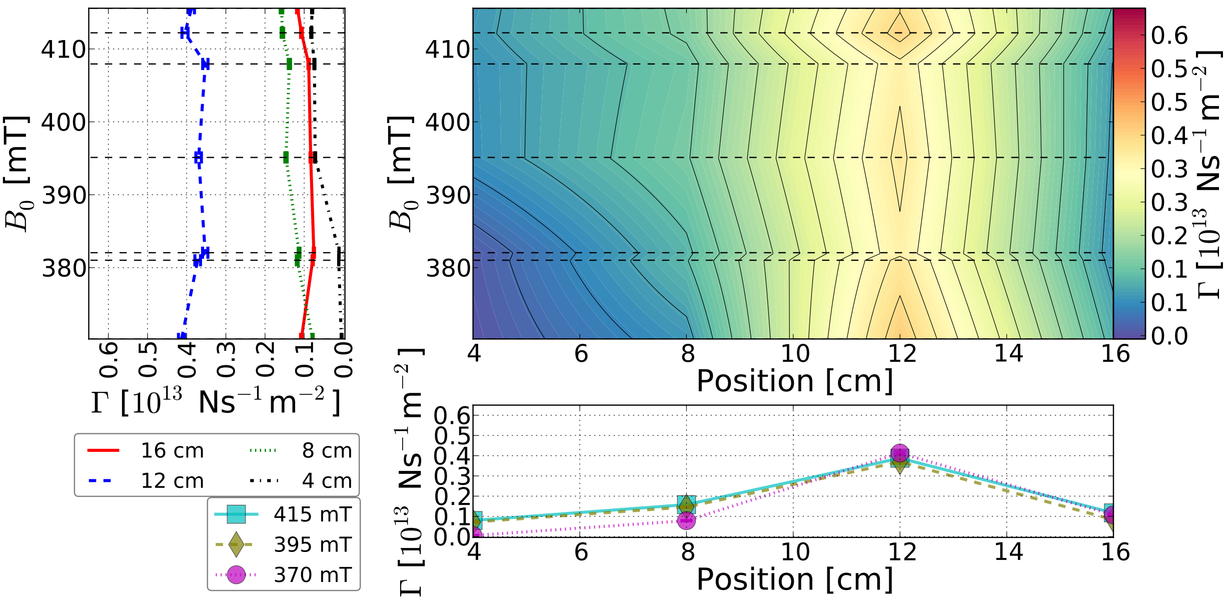

FIGURE A.2: *Equilibrium transport for neon as the magnetic field is varied.*

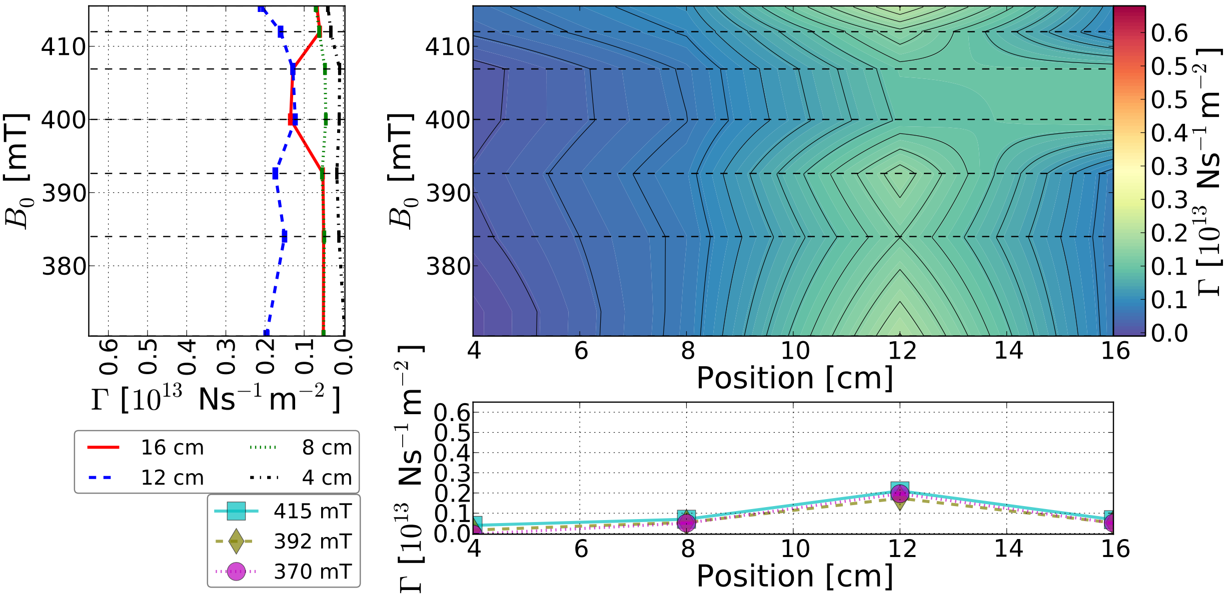

FIGURE A.3: *Equilibrium transport for argon as the magnetic field is varied.*

The transport is largest where the gradients are largest, which is expected from theory. It should be noted that due to the profiles, and due to the high D in hydrogen, the transport is approximately five times higher in hydrogen than in the rest of the gases. We also note that the transport is concentrating around the plasma edge for lower magnetic fields, while it is spreading more out at the higher fields. As D varies with T, this can be explained with the increasing flatness of the temperature profiles as the magnetic field is increasing.

A.1.2 Pressure scan

The results from the magnetic field scan are plotted in the figures A.1, A.2 and A.3. An interesting feature which can be seen from the plots, is that the transport is concentrating more towards the edge as the pressure is increased. This can be related to the hollowness of the temperature profiles increases with increasing pressure, whereas the density stays relatively constant as the pressure is varied.

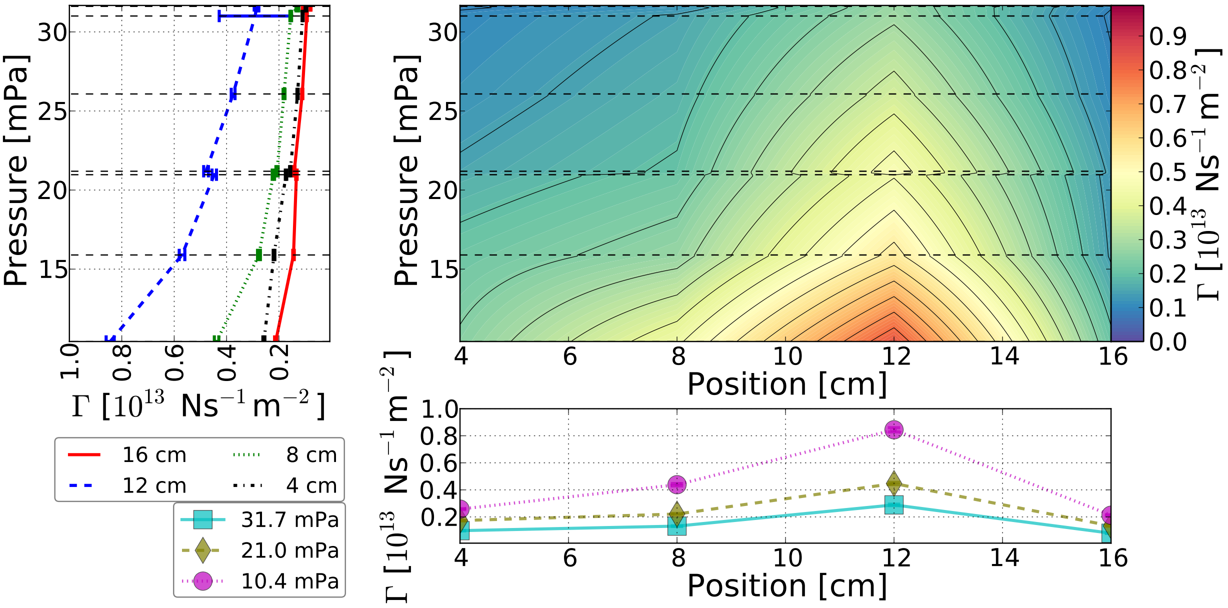

FIGURE A.4: *Equilibrium transport for helium as the pressure is varied.*

A.2 Radiation profiles

In the following section, the poloidal radiation profiles will be presented. Only shots with $R_{vh} = 0.5715 - 0.5755$ have been plotted, as these show the trends the best

A.2.1 Magnetic field scan

Figure A.7, A.8, A.9 shows how the poloidal radiation profiles are evolving with increasing magnetic field. We notice that there might be a systematic error in channel 5, as the radiation profiles are expected to be symmetric. It is noticeable that as the radiation gets higher, the poloidal gradients steepens (that is the change between two adjacent channels). The radiation losses in the three gases are comparable, although

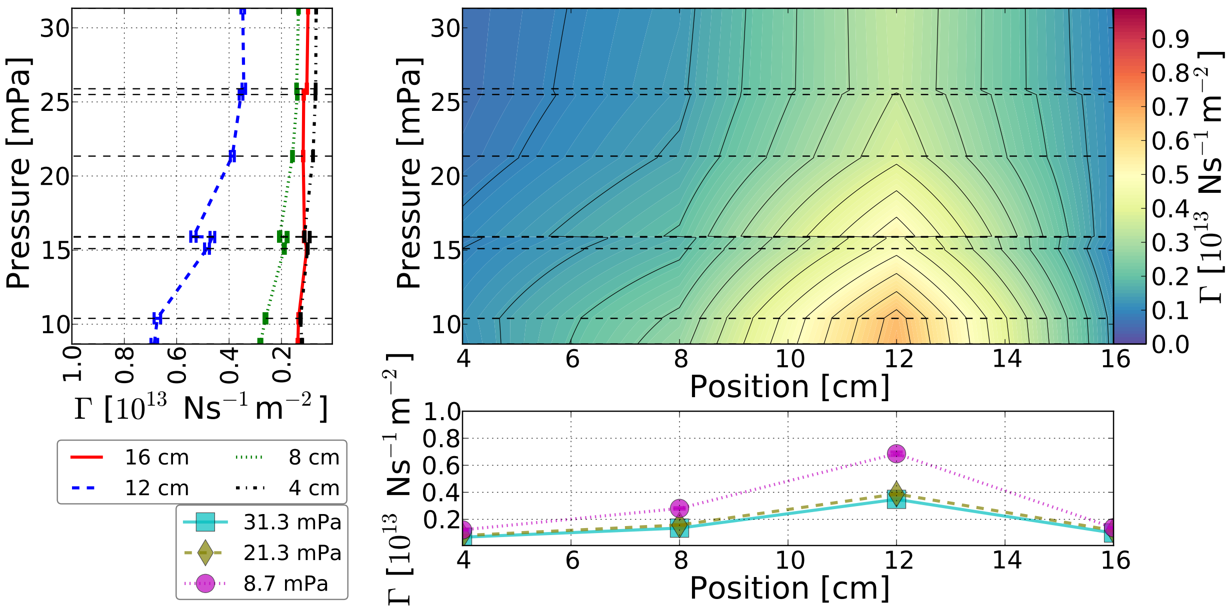

FIGURE A.5: *Equilibrium transport for neon as the pressure is varied.*

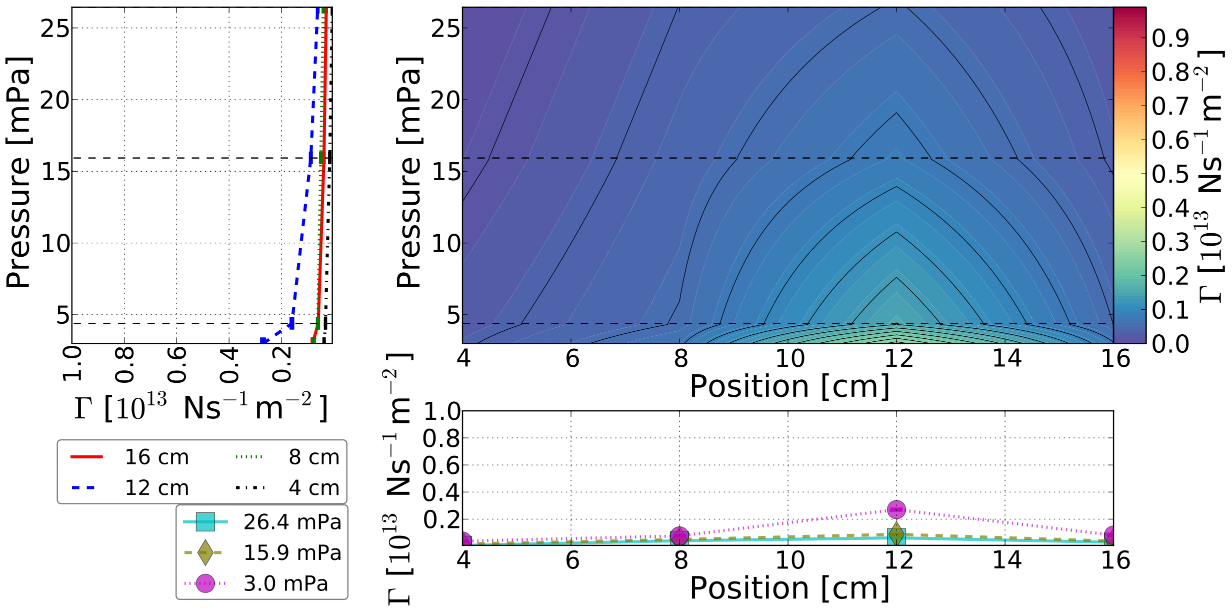

FIGURE A.6: *Equilibrium transport for argon as the pressure is varied.*

largest in argon and least in helium. This might be a consequence of more allowed transition states (that can be induced by collisions) as one increase the atomic number. The high radiation in argon might also be a consequence of the highest α_{ion}.

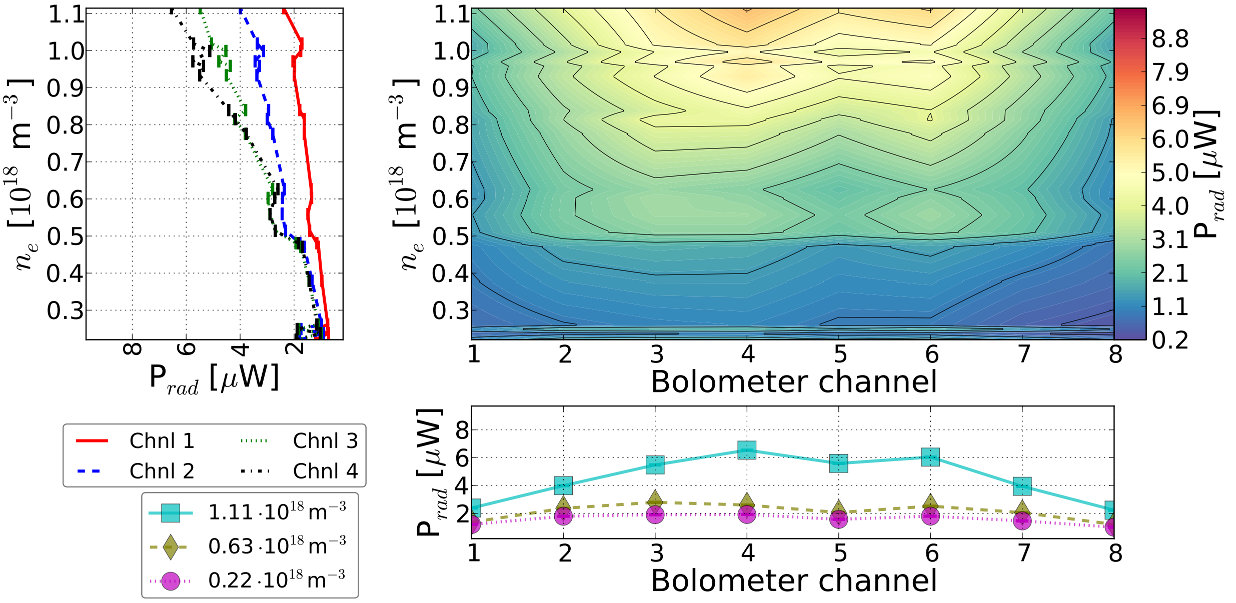

FIGURE A.7: *Poloidal radiation profiles for helium as a function of the magnetic field.*

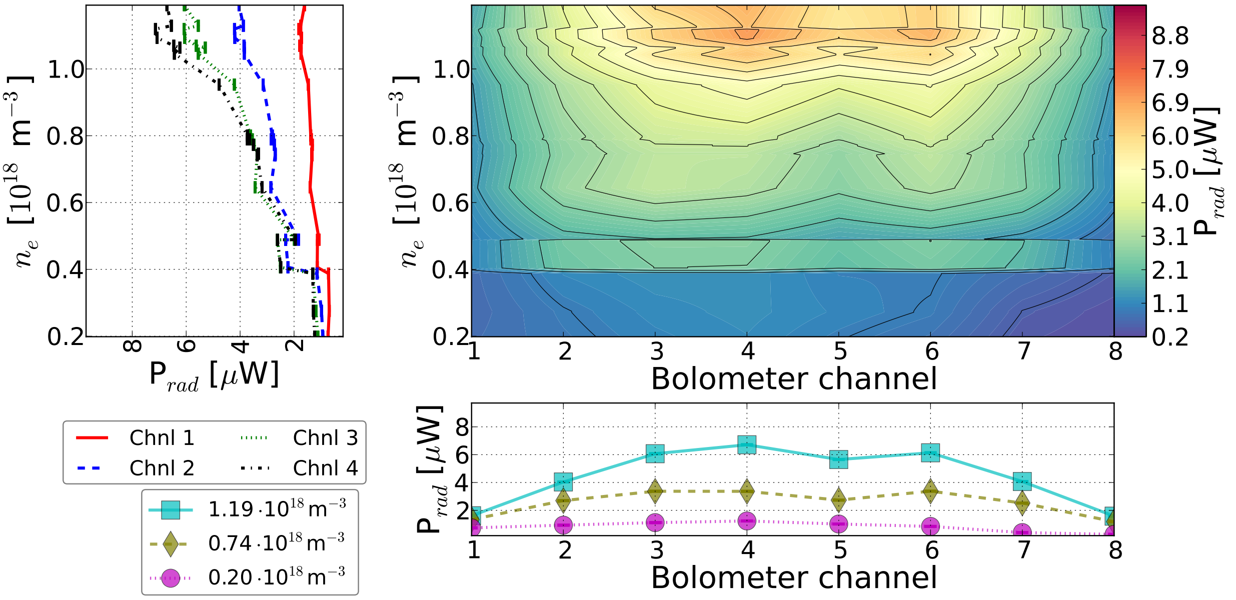

FIGURE A.8: *Poloidal radiation profiles for neon as a function of the magnetic field.*

A.2.2 Pressure scan

In the figures A.10, A.11, A.12, the poloidal radiation profiles as a function of the pressure is presented. Interestingly, we can observe as there is no common trend for the three gases as we vary the pressure. Neon shows a more or less constant profile, in helium the radiation is increasing and broadening as the pressure is increasing, whereas

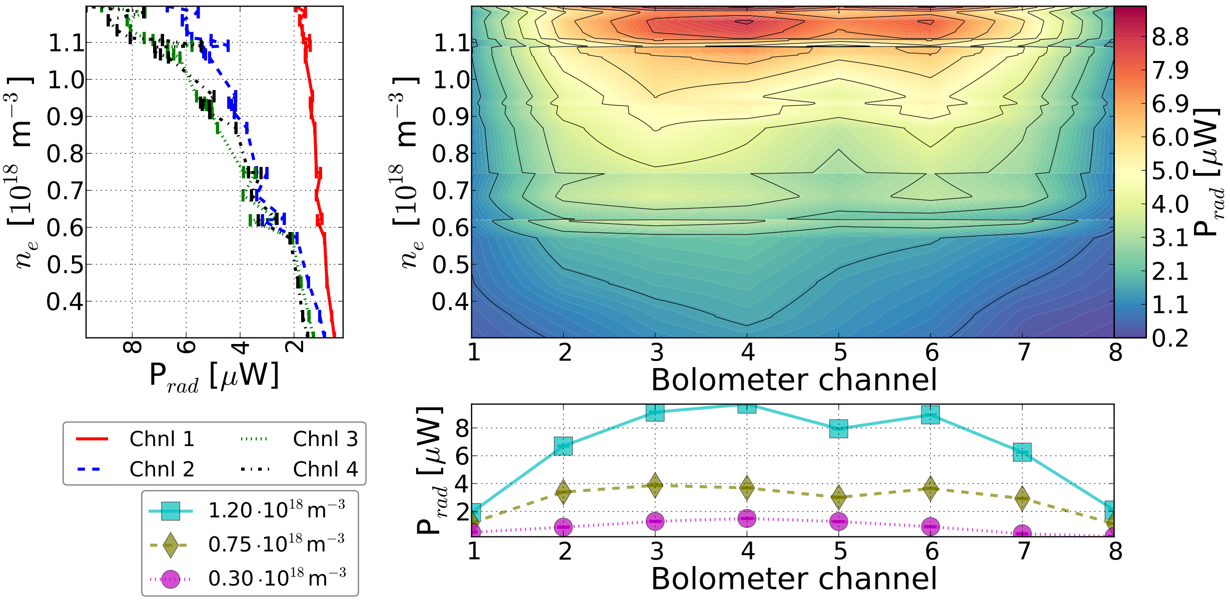

FIGURE A.9: *Poloidal radiation profiles for argon as a function of the magnetic field.*

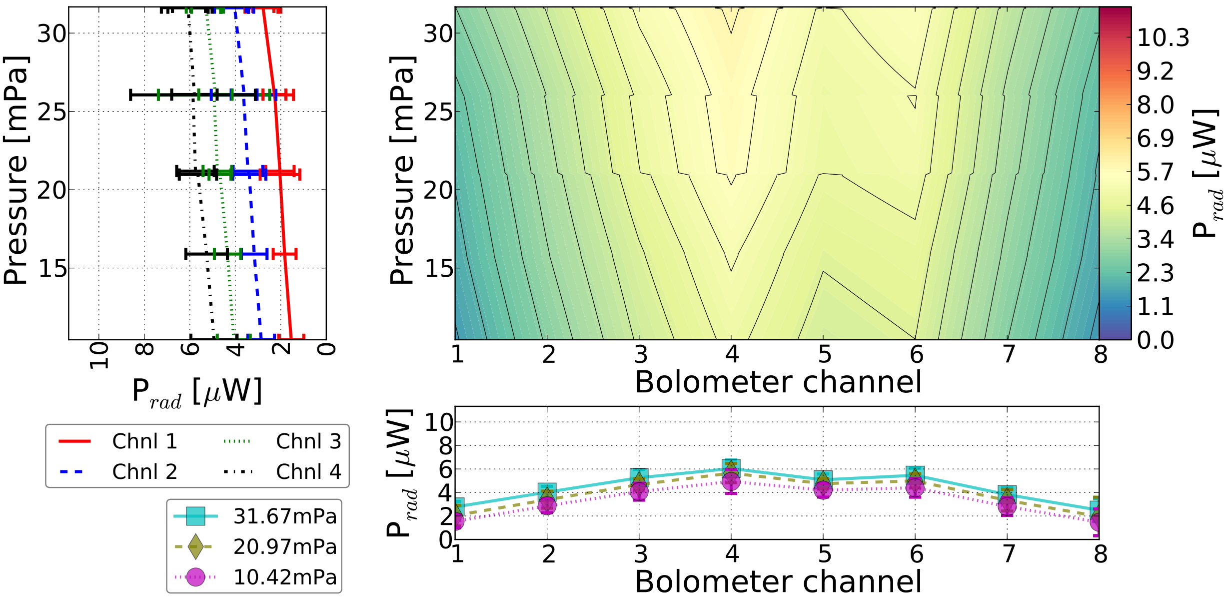

FIGURE A.10: *Poloidal radiation profiles for helium as a function of the pressure.*

the exact opposite can be observed for argon.

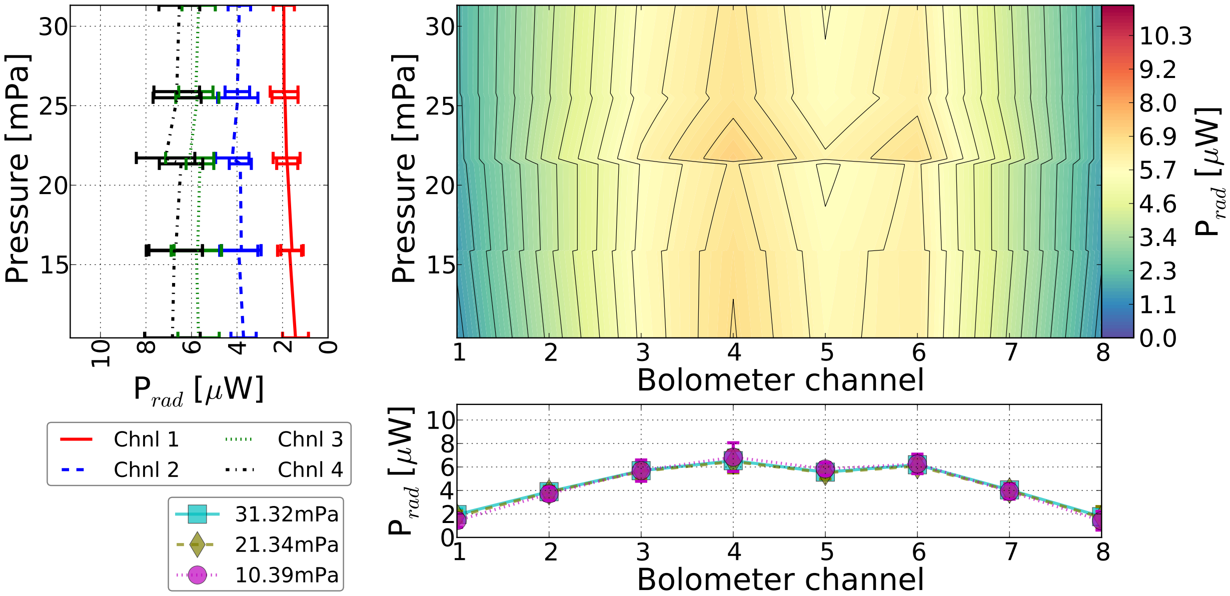

FIGURE A.11: *Poloidal radiation profiles for helium as a function of the pressure.*

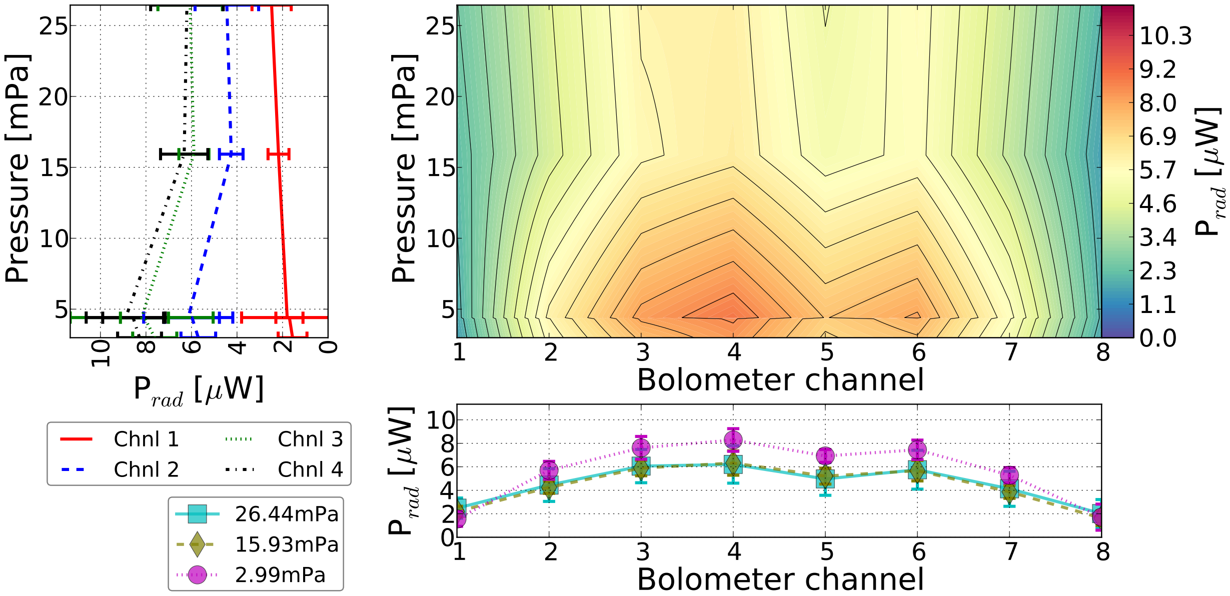

FIGURE A.12: *Poloidal radiation profiles for helium as a function of the pressure.*

A.3 Radiation obtained from the optical diode

Data has also been acquired from the optical diode. Care has to be taken when analyzing the data, since the absorption in the optical diode is a non-linear function of the frequency. Also, when the signal from the bolometer is compared with the optical diode, one has to remember that the bolometer and the optical diode have slightly overlapping absorption region in terms of frequency.

A.3.1 Magnetic field scan

Figure A.13 shows the results from the optical diode when the magnetic field is varied. We see that, although there is a large scatter, the radiation is in general increasing with increasing magnetic field. This is expected as both the density and the temperature are increasing with increasing field.

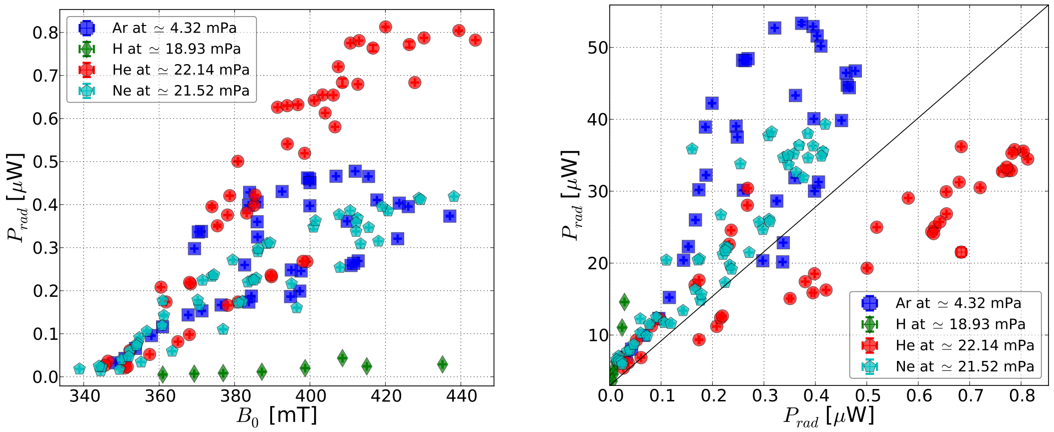

(a) The radiation recorded by the optical diode as a function of the magnetic field.

(b) Comparison of the two devices measuring the radiation.

FIGURE A.13: *Results obtained from the optical diode as the magnetic field is varied.*

We can see from figure A.13b that the radiation is shifting towards higher frequencies as we increase the magnetic field for all gases except helium. For the highest fields in helium, we see the opposite behavior. To explain this further, one should have a look at the atomic states present in the plasma.

A.3.2 Pressure scan

In figure A.14 we can see how the variation in the optical diode as the pressure is varied. The radiation recorded in the optical diode clearly states that the radiation is increased as the base pressure is increased. Similar trend might be the case for the bolometers as well. It was suggested that more neutral particles in the plasmas could be the reason for increased radiation. Figure A.14b tells us that the energy is shifted towards higher frequencies for neon, and to lower frequencies for helium as the base pressure is increased.

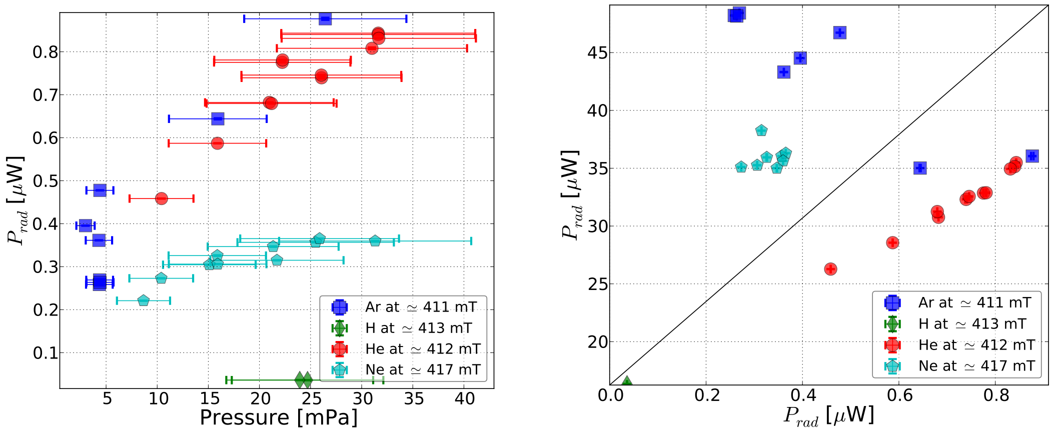

(a) The radiation recorded by the optical diode as a function of the pressure.

(b) Comparison of the two devices measuring the radiation.

FIGURE A.14: *Results obtained from the optical diode as the pressure is varied.*

Bibliography

[1] I. H. Hutchinson, *Principles of Plasma Diagnostics 2nd ed.* (Cambridge University Press, Cambridge, 2002).

[2] R. A. Helliwell, *Whistlers and Related Ionospheric Phenomena* (Dover Publications, New York, 2006).

[3] T. H. Stix, *Waves in plasmas* (American Institute of Physics, New York, 1992).

[4] A. Köhn, Ph.D. thesis, Institut für Plasmaforschung der Universität Stuttgart, Stuttgart, 2010, 🗎.

[5] J. Friedberg, in *Plasma Physics and Fusion Energy* (Cambridge University Press, Cambridge, 2007), Chap. 9, pp. 183 – 196.

[6] U. Stroth, in *Transport in Toroidal Plasmas - Plasma Physics - Confinement, Transport and Collective Effects*, edited by A. Dinklage, T. Klinger, G. Marx, and L. Schweikhard (Springer, Berlin Heidelberg, 2005).

[7] K. Rahbarnia, Diploma thesis, Christian-Albrechts-Universität, Kiel, 2001.

[8] U. Stroth, *Einführung in die Plasmaphysik, Vorlesungsskript* (Institut für Plasmaforschung, Universität Stuttgart, Stuttgart, 2007).

[9] U. Stroth *et al.*, Physics of Plasmas **11**, 2558 (2004), 🗎.

[10] T. C. Luce, C. C. Petty, and C. J. G., Plasma Physics and Controlled Fusion **50**, (2008), 🗎.

[11] C. C. Petty, Physics of Plasmas **15**, (2008), 🗎.

[12] S. Wolf, Diploma thesis, Institut für Plasmaforschung der Universität Stuttgart, Stuttgart, 2012.

[13] J. Seifert, Diploma thesis, Institut für Plasmaforschung der Universität Stuttgart, Stuttgart, 2011.

[14] J. Stöber, Diploma thesis, Christian-Albrechts-Universität, Kiel, 2001.

[15] H. Mott-Smith and I. Langmuir, Phys. Rev. **28**, 727 (1926), 🗋.

[16] B. Nold, Ph.D. thesis, Institut für Plasmaforschung der Universität Stuttgart, Stuttgart, 2012, 🗋.

[17] U. Stroth, *Plasmaphysik, Phänomene, Grundlagen, Anwendungen* (Vieweg+Teubner, Wiesbaden, 2011).

[18] M. Lieberman and A. Lichtenberg, in *Principles of Plasma Discharges and Materials Processing, Second Edition* (John Wiley and Sons, New York, 2005), Chap. 6, p. 154.

[19] F. Chen, in *Plasma Diagnostic Techniques*, edited by R. H. Huddlestone and S. L. Leonard (Academic Press, New York, 1965), Chap. 4, pp. 113–200.

[20] M. Ramisch, Ph.D. thesis, Christian-Albrechts-Universität, Kiel, 2005, 🗋.

[21] W. H. Press, B. P. Flannery, S. A. Teukolsky, and W. T. Vetterling, in *Numerical Recipes in C, 2nd ed.* (Cambridge University Press, Cambridge, 1992), Chap. 15.5, pp. 683–688.

[22] A. Zilch, Diploma thesis, Institut für Plasmaforschung der Universität Stuttgart, Stuttgart, 2011.

[23] C. S. Merli, Diploma thesis, Institut für Plasmaforschung der Universität Stuttgart, Stuttgart, 2010.

[24] M. Bernert, Diploma thesis, Max-Planck-Institut für Plasmaphysik, Garching, 2010.

[25] K. F. Mast *et al.*, Rev. Sci. Instrum. **62**, 744 (1991), 🗋.

[26] M. Schubert, Diploma thesis, Physik Departement der Technischen Universität München, München, 1999.

[27] E. B. Arroyo, Diploma thesis, Max-Planck-Institut für Plasmaphysik, Garching, 1997.

[28] L. Giannone, K. F. Mast, and M. Schubert, Rev. Sci. Instrum. **73**, 3205 (2002), 🗋.

[29] Siemens, *Silicon PIN Photodiode BPX 61*, 🗋.

[30] M. Spiegel, J. Schiller, and R. A. Srinivasan, *Schaum's Outline of Probability and Statistics, 4th Edition* (McGraw Hill Companies, New York, 2013).

[31] S. Enge, Ph.D. thesis, Institut für Plasmaforschung der Universität Stuttgart, Stuttgart, 2010, 🗋.

[32] C. Lechte, J. Stöber, and U. Stroth, Phys. Plasmas **9**, 2839 (2002), 🗋.

[33] NIST, Atomic Spectra Database, Version 3.0, 🗋.

[34] B. d. Darwent, *Bond dissociation energies in simple molecules* (University of California Libraries, Washington, 1970), 🗎.

[35] R. Prater *et al.*, AIP Conference Proceedings **159**, 9 (1987), 🗎.

[36] A. Köhn *et al.*, AIP Conference Proceedings **1406**, 493 (2011), 🗎.

[37] G. Birkenmeier, Diploma thesis, Institut für Plasmaforschung der Universität Stuttgart, Stuttgart, 2008.

[38] P. Vacuum, *Operating Instructions - Compact Full Range Gauge FPM sealed PKR 251*, 🗎.

[39] A. Köhn *et al.*, Plasma Physics and Controlled Fusion **55**, (2013), 🗎.

Acknowledgements

I would here like to thank those who have helped. This thesis would not have been what it is, if it was not thanks to a lot of people.

I express my gratitude towards the steering committee of the Erasmus Mundus FUSION-EP programme for accepting me as a student in this program, giving me the opportunity to participate in this great international experience.

I would like to thank the hosting institutions for the first year at Université de Lorraine, and especially Dr. Daniele Del Sarto for supervising my M1 stage.

Further thanks goes to all the people working at the hosting institution for the second year at Universität Stuttgart, firstly for providing a great working atmosphere, and secondly for hosting the educational "Mittwoch"-seminars. I am also thankful for all the help provided by Dr. Mirko Ramisch, Golo Fuchert, Stefan Wolf, Stefan Merli and Bernhard Schmidt.

My thanks also goes to Frank Janssens, Dr. Carsten Lecthe and Prof. Gérard Bonhomme for providing valuable help in urgent situations.

Especially I would like to thank my supervisor Dr. Alf Köhn for being extremely helpful and service minded, and for all the time he has offered to help me with this work.

I would like to thank my family for always being supportive, and I would like to give a special thank to Lenka Zaťková for always being there for me, always believing in me, and for making may days bright and enjoyable.

Declaration in lieu of oath

Herewith I declare in lieu of oath that I have prepared this thesis exclusively with the help of my scientific teachers and the means quoted by them.

Stuttgart, the 7th of July

Michael Løiten

Copyright Agreement

I hereby grant the FUSION-EP consortium the non-exclusive right to publish this work. I declare that this work is free of copyright claims of third parties.

Stuttgart, the 7th of July

Michael Løiten